



Second-harmonic generation from silicon monoxide and zinc oxide

From bulk effects to interactions with ambient air

Andersen, Søren Vejling

Publication date:
2014

Document Version
Early version, also known as pre-print

[Link to publication from Aalborg University](#)

Citation for published version (APA):

Andersen, S. V. (2014). *Second-harmonic generation from silicon monoxide and zinc oxide: From bulk effects to interactions with ambient air*. Department of Physics and Nanotechnology, Aalborg University.

General rights

Copyright and moral rights for the publications made accessible in the public portal are retained by the authors and/or other copyright owners and it is a condition of accessing publications that users recognise and abide by the legal requirements associated with these rights.

- Users may download and print one copy of any publication from the public portal for the purpose of private study or research.
- You may not further distribute the material or use it for any profit-making activity or commercial gain
- You may freely distribute the URL identifying the publication in the public portal -

Take down policy

If you believe that this document breaches copyright please contact us at vbn@aub.aau.dk providing details, and we will remove access to the work immediately and investigate your claim.

Second-harmonic generation from silicon monoxide and zinc oxide

From bulk effects to interactions with ambient air

SØREN VEJLING ANDERSEN

SUPERVISOR: PROFESSOR KJELD PEDERSEN

PhD Thesis in Physics
Department of Physics and Nanotechnology
Aalborg University

Second-harmonic generation from silicon monoxide and zinc oxide

Anden-harmonisk generation fra siliciummonoxid og zinkoxid

Front cover illustration

Measured second-harmonic generated signal from a 2D silicon monoxide structures defined by lithography.

Copyright ©2014 by Søren Vejling Andersen and the Department of Physics and Nanotechnology, Aalborg University

Published and distributed by

Department of Physics and Nanotechnology, Aalborg University

Skjernvej 4A, DK-9220 Aalborg Øst.

Phone +45 99 40 92 15. Fax +45 99 40 92 35

Printed in Denmark by Uniprint, Aalborg

All right reserved. No part of the publication may be reproduced, transmitted or translated in any form or by any means, electronic or mechanical, including photocopy, recording, or any information storage and retrieval system, without prior permission in writing from the author.

ISBN 87-89195-32-9

Second-harmonic generation from silicon monoxide and zinc oxide

From bulk effects to interactions with ambient air

by

Søren Vejling Andersen

Supervisor: Professor Kjeld Pedersen

List of published papers

1. S.V. Andersen, K. Pedersen, "Second-harmonic generation from electron beam deposited SiO", Optics Express, Vol. 20, Issue 13, pp. 13857-13869 (2012)
2. S.V. Andersen, M.L. Trolle, K. Pedersen, "Growth direction of oblique angle electron beam deposited silicon monoxide thin films identified by optical second-harmonic generation", Applied Physics Letters, Vol. 103, Iss. 23, pg. 231906 (2013).
3. S. V. Andersen, V. Vandalon, R. H. E. C. Bosch, B. W. H. van de Loo, K. Pedersen, and W. M. M. Kessels, "Interaction between O₂ and ZnO probed by time-dependent second-harmonic generation", Applied Physics Letters, Vol. 104, Iss. 5, pg. 051602 (2014).

This thesis has been submitted for assessment in partial fulfilment of the PhD degree. The thesis is based on the submitted or published scientific papers which are listed above. Parts of the papers are used directly or indirectly in the extended summary of the thesis. As part of the assessment, co-author statements have been made available to the assessment committee and are also available at the Faculty. The thesis is not in its present form acceptable for open publication but only in limited and closed circulation as copyright may not be ensured.

Preface

This thesis summarizes the main results gained during my time as a PhD student at the Department of Physics and Nanotechnology, Aalborg University, Denmark, from December 2010 to November 2013 under the supervision of Professor Kjeld Pedersen. From February to end April I had the pleasure to stay abroad in the group Plasma and Materials Processing of Professor Erwin Kessels at the Department of Applied Physics, Eindhoven University of Technology (TU/e), The Netherlands. My main work during my PhD study in Aalborg has been focused on second-harmonic generation to study the surprising bulk nonlinear optical properties of silicon monoxide prepared by electron beam deposition. In Eindhoven the interaction between ZnO and oxygen molecules was studied with second-harmonic generation. The thesis is based on three journal papers and the work surrounding them. A list of published articles and conference talks presenting the main results can be found in Chap. 8.

Outline of the thesis

Chap. 2 is meant as an introduction to the fundamentals of optical second-harmonic generation and thereby the main physics used in this thesis to analysis the characteristics of the nonlinear optical response from SiO and ZnO. Followed by Chap. 3, where the different deposition techniques used to synthesize SiO and ZnO thin films are briefly presented. The optical second-harmonic setups used to investigate the second-harmonic response from these thin films are presented. Chap. 4 presents the second-harmonic response from SiO and is linked to the papers found in App. A and B. It is demonstrated that the second-harmonic generated signal is dependent on film thickness and that orientated dipoles created during the deposition may be the cause for the second-order nonlinear response. Furthermore, it is demonstrated that oblique angle deposition of SiO leads to a tilting porous structure where the second-order nonlinear optical response can be controlled through the deposition angle. By analysing the angular dependency of the second-harmonic response of

this OAD SiO the growth direction can be identified. Then some unpublished results regarding the oxidation of porous SiO structures when in contact with ambient air is presented. Finally, Chap. 4 demonstrates that also the growth direction of oblique angle deposited ZnO can be identified. Chap. 5 is linked to App. C, which presents the nonlinear optical properties of atomic layer deposited ZnO thin films. It is demonstrated that the interaction between oxygen and ZnO probed by time-dependent second-harmonic generation is possible. Finally, a short summary in English can be found in Chap. 6 and in Danish see chapter 7.

Acknowledgements

First I would like to address a special thanks to my supervisor **Kjeld** for his guidance, very useful help, especially in the laboratory, and not at least our scientific talks even at busy times. Thanks for your "open door" policy for that I'm grateful. I would like to acknowledge **Erwin** for welcoming me to the PMP group at Eindhoven University of Technology. I would like to send a special thanks to **Peter** and **Jens** for the assistance in the cleanroom and for introducing me to the equipment and to **Kjeld**, **Rasmus** and **Jens** for introducing me to nanosecond lab. I would like to acknowledge my old Masters group at Aarhus university for still having the laboratory equipment (and coffee maker) at my disposal. Thank you **John** for the RBS and SIMS measurements and **Britta** for the fantastic SEM images which have shown to be invaluable. I would like to thank **Hans** for quickly creating all the imported sample holders. A thanks to **Esben** and **Paw** for giving me femtosecond laser time. I would like to acknowledge all my colleagues at the department for many (necessary) informal discussions over a cup of coffee. I would like thank **Rasmus** og **Troels** for the nice welcome to "the newcomer" at the office and for showing me the ropes around the department. To **Kristian** and **Mads** for filling the office with fruitful discussions on "wired" result and thanks to **Mads** for his enthusiastic approach to physics with the words "This is easy to model, I can quickly do it..!?". The invaluable "non-expert" discussions on topics not related to the department have been fantastic, thanks **Kristian** and **Mads**. I would like to extend a big "thank you" to the groups members at PMP for the very open welcome and for making the time in Eindhoven an enjoyable time. Especially **Roger**, **Vincent** and **Bas** I have enjoyed every minute in the darkness in the lab discussing decaying SHG signals. I will definitely come back for a visit, preferably on a Thursday... A warm thanks to **Dennis** and **Jakob** for the proof reading, you definitely made it at more smooth read. Last, but not least, I would like thank my girlfriend **Vera** for understanding why sometimes my thoughts are somewhere in the "Ether" and for supporting me throughout the last three years, and **Luna**, sorry for not having so much time to play the last six months, I will make up for it.

February 24, 2014 **Søren Vejling Andersen**

Contents

1	General Introduction	1
2	Theory	5
2.1	The basics of bulk second-harmonic generation	5
2.2	Angular dependence of SHG	8
2.3	Rotation of the second-order nonlinear susceptibility tensor	10
2.4	Electric field induced second-harmonic generation	11
3	Experimental techniques	13
3.1	Electron beam deposition technique	13
3.2	Atomic layer deposition	15
3.3	Structural properties	15
3.4	Linear optical characterization technique	16
3.5	The nonlinear optical techniques	17
4	Second-harmonic generation from SiO	21
4.1	Introduction	21
4.2	Second-harmonic generation from SiO	22
4.3	Oblique angle deposited SiO	27
4.4	Oxidation of oblique angle deposited SiO	29
4.5	Oblique angle deposited ZnO	36
4.6	Summary and Outlook	39

5	Interaction between ZnO and O₂ probed by TD-SHG	41
5.1	Introduction	41
5.2	Structural properties	42
5.3	Second-harmonic generation from ALD ZnO	43
5.4	Time-dependent second harmonic generation	45
5.5	Ageing of ZnO	48
5.6	Summary and Outlook	53
6	Summary	55
7	Resumé	57
8	List of publications	59
	Bibliography	61
	Appendices	69
A	Optics Express, Vol. 20, Issue 13, pp. 13857-13869 (2012)	71
B	Appl. Phys. Lett. 103, 231906 (2013)	87
C	Appl. Phys. Lett. 104, 051602 (2014)	93

General Introduction

The interaction between light and matter has been studied for many centuries and in 1865 Maxwell formulated a complete set of equations governing classical electrodynamics.¹ Two years later the Danish physicist Ludvig V. Lorenz, independently of Maxwell², developed the same set of equations describing the nature of light and its interaction with matter.³ Almost 100 years was needed before Franken *et al.*⁴ demonstrated the possibility to generate optical second-harmonics in non-centrosymmetric crystals. This was one of many positive consequences of the invention of the laser in 1960⁵, since intense radiation is needed in order to generate a second-harmonic (SH) electromagnetic field. Hence, the requirement of a laser makes the optical second-harmonic generation (SHG) technique a fairly young one, which is also evident from Fig. 1.1 showing a number of documents including the words "second-harmonic generation".

Strict symmetry conditions are needed in order for SHG to occur. If a material is centrosymmetric, which means that the crystal structure upholds inversion symmetry, no bulk SHG signal is generated. If the material is non-centrosymmetric (no inversion symmetry) it allows for a bulk SHG signal.⁶ Despite this, Terhune *et al.*⁷ showed that centrosymmetric calcite has a SHG response and Bloembergen *et al.*⁸ also demonstrated that centrosymmetric crystalline silicon has a SHG response. These surprising, at that time, SHG signals were realized to be related to surface conditions breaking the inversion symmetry.^{9,10} This realization allows for study of buried interfaces between two centrosymmetric materials, for instance, the very important SiO₂/Si interface.¹¹ Moreover, a number of investigations have

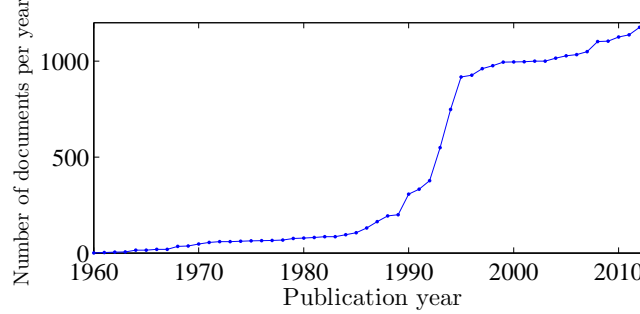


Figure 1.1: Number of documents found in the literature include the words "second-harmonic generation" as a function of publication year yielding a total of 24026 documents starting from 1960 to 2013.

demonstrated a strong sensitivity of SHG to charges at semiconductor surfaces and interfaces through an electric field induced third-order effect.^{12,13} Important information about the space-charge regions at interfaces between silicon and thin films has also been revealed.^{9,10,14,15} Due to the strict symmetry conditions second-harmonic generation is considered to be a very important tool to investigate surfaces and interfaces of centrosymmetric materials and as illustrated in Fig. 1.1 this research field exploded in the mid-1990's.

The explosion in articles was a result of the development of new nonlinear optical materials compatible with Si process technology, which has been an active research field over the past two decades due to an increased fibre communication market. Nonlinear materials provide the basis for several important photonic properties⁶, for instance, on-chip devices for high-speed optical switching, electro-optic modulation, wavelength conversion.^{16,17,18} Poling of glasses is considered a promising process that can lead to large second-order nonlinearities over a broad spectral range for a wide range of glass compositions.^{19,20,21} In combination with bulk allowed third-order nonlinearities, this results in an effective second-order effect allowing SHG as well as electro optic effects. An enhancement of more than two orders of magnitude of SHG compared to bulk poled silica glass has been obtained from a poled stack of alternating doped and un-doped layers of silica.²² Moreover, poled polymers are also considered to be promising for photonic applications.²³ However, poling is a post deposition process that requires electrode contacts, hence, making it difficult to induce nonlinear effects in nanostructures²⁴, which is desirable for optical devices.

The overall objective of this project is to investigate the nonlinear second-order optical properties from two very different monoxides, namely silicon monoxide (SiO) and zinc monoxide (ZnO), where the latter is normally called zinc oxide. Apart from this, time-dependent second-harmonic generation from porous SiO and ZnO

films are used to study the interaction between the ambient atmosphere and these fascinating oxides.

Silicon monoxide is a useful material with many industrial applications, for instance as protective coatings or as part of dielectric stacks for mirrors and antireflective coatings.^{25,26,27} SiO is amorphous with a complex atomic structure which is not yet fully understood^{28,29}. Since SiO is amorphous, and therefore upholds inversion symmetry on at macroscopic scale, no previous work has been reported on SHG from SiO. This work demonstrates that with the correct deposition conditions SiO thin films are second-order nonlinear active. The origin is discussed and different uses of this nonlinear optical properties of SiO are demonstrated.

Single crystalline ZnO was one of the very first non-centrosymmetric crystal to be studied with SHG.³⁰ The second-harmonic response is very large and later on it was demonstrated that the response strongly depends on the nanostructure and film thickness.^{31,32,33,34} Apart from being nonlinear optical active the surface of ZnO has been demonstrated to interact with oxygen.^{35,36} This work demonstrates that TD-SHG can be used to study this interaction between oxygen and ZnO.

This vital non-contact SHG characterization technique becomes powerful when combined with other techniques, such as Rutherford backscattering spectroscopy (RBS), scanning emission microscopy (SEM), secondary ion mass spectrometry (SIMS) and spectrometric ellipsometry (SE). These techniques will provide insight into the structural properties and the important linear optical properties, which will help to clarify the origin of the SHG signal.

Chapter 2 will give some general remarks on the theoretical foundation of SHG from thin nonlinear films having a bulk response. Chapter 3 presents the main characterization tools and deposition techniques used in this work. We move on to chapter 4, which demonstrates that through a standard electron beam deposition technique of SiO, a second-order nonlinear thin film can be produced. Furthermore, it is demonstrated that through oblique angle deposition (OAD) of SiO one can tune the SHG response. Investigating the angular dependence of the SH response from these OAD thin films the growth direction can be identified. Chapter 4 ends by discussing this oxidation dynamics of porous OAD SiO. Chapter 5 demonstrates that time-dependent second-harmonic generation (TD-SHG) can be used to study the interaction between ZnO and O₂. This thesis ends with summaries in English (Chapter 6) and in Danish (Chapter 7).

Theory

This chapter introduces the basic principles and phenomenology of a generated second-harmonic electromagnetic field, when a nonlinear medium is exposed to an intense (fundamental) electromagnetic radiation. Next, the dependence of the observed optical second-harmonic intensity as a function of angle of incidence of the fundamental field is discussed. The response can reveal important information about nonlinear properties and thereby the structural properties of a material. Finally, this chapter ends with a brief presentation of electric-field induced second-harmonic generation.

2.1 The basics of bulk second-harmonic generation

Exposing a nonlinear medium to an electromagnetic field (light) leads to linear phenomena such as refraction and reflection of the medium which is easily detected by the naked eye. In general the electromagnetic field $\vec{E}(\vec{r}, \omega)$ will induce an optical polarization $\vec{P}(\vec{r}, \omega)$ in the medium at position \vec{r} with a frequency ω described by⁶

$$\vec{P}(\vec{r}, \omega) = \epsilon_0 \overset{\leftrightarrow}{\chi}^{(1)}(\omega) \vec{E}(\vec{r}, \omega). \quad (2.1)$$

Here ϵ_0 is the vacuum permittivity and $\overset{\leftrightarrow}{\chi}^{(1)}(\omega)$ is the electric susceptibility which is the second-rank tensor describing the interaction between the medium and the E-field, e.g., refraction and reflection at the surface. Probing the same nonlinear medium with an intense E-field results in higher order (n) optical effects and, assuming spatially homogeneous fields and that the medium is lossless and dispersionless,

the polarization can then be described as^{6,37}

$$\vec{P}(\vec{r}, t) = \epsilon_0 \overset{\leftrightarrow}{\chi}^{(1)} \vec{E}(\vec{r}, t) + \epsilon_0 \overset{\leftrightarrow}{\chi}^{(2)} \vec{E}(\vec{r}, t)^2 + \epsilon_0 \overset{\leftrightarrow}{\chi}^{(3)} \vec{E}(\vec{r}, t)^3 + \dots \quad (2.2)$$

$$\equiv \vec{P}^{(1)}(\vec{r}, t) + \vec{P}^{(2)}(\vec{r}, t) + \vec{P}^{(3)}(\vec{r}, t) + \dots \quad (2.3)$$

where $\overset{\leftrightarrow}{\chi}^{(n)}$ is the n^{th} order susceptibility tensor of the rank $n + 1$. For $n > 1$ the polarization $\vec{P}^{(n)}(\vec{r}, t)$ is the n -order, which depends on the nonlinear behaviour on the form $\vec{E}^n(\vec{r}, t)$. Therefore, the word "nonlinear" is used to describe this optical phenomenon for $n > 1$. Here the second-harmonic generated polarization is given by

$$P_i^{(2)}(2\omega) = \epsilon_0 \sum_{jk} \chi_{ijk}^{(2)}(2\omega, \omega, \omega) E_j(\omega) E_k(\omega) \quad (2.4)$$

This equation demonstrates that when an intense $\vec{E}(\omega)$ is oscillating at ω it will generate a polarization $\vec{P}^{(2)}(2\omega)$ oscillating at the double frequency 2ω .

The nonlinear susceptibility tensor $\overset{\leftrightarrow}{\chi}^{(2)}$ arises due to the intense E-field interacting with electrons surrounding the atoms in the nonlinear medium. The time-dependent E-field will induce an time-dependent atomic dipole. Performing at full quantum mechanical analysis, with perturbation theory and an interaction Hamiltonian $\hat{V}(t) = -\hat{\mu} \cdot \vec{E}(\vec{r}, t)$ describing the interaction between the electrons with the probing electromagnetic field, where $\hat{\mu} = e\hat{\mathbf{r}}$ is the electric dipole operator, results in a nonlinear second-order susceptibility tensor given by³⁸

$$\chi_{ijk}^{(2)}(2\omega, \omega, \omega) = -\frac{Ne^3}{\hbar^2} \sum_{g,n,n'} \left[\frac{\langle g|r_i|n\rangle \langle n|r_j|n'\rangle \langle n'|r_k|g\rangle}{(2\omega - \omega_{n'g} + i\Gamma_{n'g})(\omega - \omega_{ng} + i\Gamma_{ng})} + \dots \right] \rho_g^{(0)}. \quad (2.5)$$

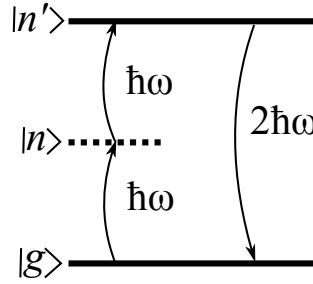


Figure 2.1: Locations of the resonances of the term in Eq. (2.5).

This expression includes 8 terms that describe a sequences of electron transitions. The term in Eq. (2.5) represents the electron transitions illustrated in Fig. 2.1.

Two photons excite the system from the initial ground state $|g\rangle$ with the energy $\hbar\omega$ to the intermediate states $|n'\rangle$ and $|n\rangle$, see Fig. 2.1. When the system relaxes back to the initial state $|g\rangle$ a photon with the energy $2\hbar\omega$ is emitted. Γ is the characteristic relaxation time for the transitions between the states which defines the line broadening. N denotes the density of dipoles and $\rho_g^{(0)}$ denotes the population of the state $|g\rangle$. When the incident fundamental probing photons have an energy $\hbar\omega$ comparable to the resonance $\hbar\omega_{n'g}$ the SHG photons are resonantly enhanced.

If the nonlinear medium is probed far from resonance frequency (far from the energy band gap) $\chi_{ijk}^{(2)}$ can be considered a constant in ω and the medium is lossless (transparent). As a consequence this allows for permutation of the indices without permuting frequencies

$$\chi_{ijk}^{(2)}(2\omega, \omega, \omega) = \chi_{jki}^{(2)}(2\omega, \omega, \omega) = \chi_{kij}^{(2)}(2\omega, \omega, \omega) = \chi_{ikj}^{(2)}(2\omega, \omega, \omega) \quad (2.6)$$

$$= \chi_{jik}^{(2)}(2\omega, \omega, \omega) = \chi_{kji}^{(2)}(2\omega, \omega, \omega). \quad (2.7)$$

This is the so-called Kleinman symmetry condition which has mainly been considered throughout this work. When this condition is valid a nonlinear tensor is defined $d_{ijk} = \frac{1}{2}\chi_{ijk}^{(2)}$ which is used to simplify the notation of the 3. rank tensor $\chi^{(2)}$. As demonstrated above the indices j and k are symmetric, consequently, j and k can be replaced with a single index l constructed as $xx = 1$, $yy = 2$, $zz = 3$, $yz = 4$, $xz = 5$, and $xy = 6$. This leads to a 3×6 matrix d_{il}

$$d_{il} = \begin{bmatrix} d_{11} & d_{12} & d_{13} & d_{14} & d_{15} & d_{16} \\ d_{16} & d_{22} & d_{23} & d_{24} & d_{14} & d_{12} \\ d_{15} & d_{24} & d_{33} & d_{23} & d_{13} & d_{14} \end{bmatrix} \quad (2.8)$$

due to permutation of the indices, $d_{35} = \frac{1}{2}\chi_{zzx}^{(2)} = \frac{1}{2}\chi_{xzz}^{(2)} = d_{13}$ is allowed as demonstrated in the matrix (2.8). Then 10 independent tensor elements remain contra the original 27 tensor elements in $\overset{\leftrightarrow}{\chi}^{(2)}$.

In this work the $C_{\infty v}$ space symmetry is mainly considered which results in a nonlinear susceptibility tensor consisting of the nonvanishing components d_{15} , $d_{24} = d_{15}$, d_{31} , $d_{32} = d_{31}$, and d_{33} . Under Kleinman symmetry $d_{31} = d_{15}$, leaving only two independent tensor elements to be considered

$$d_{il} = \begin{bmatrix} 0 & 0 & 0 & 0 & d_{31} & 0 \\ 0 & 0 & 0 & d_{31} & 0 & 0 \\ d_{31} & d_{31} & d_{33} & 0 & 0 & 0 \end{bmatrix} \quad (2.9)$$

Rewriting Eq. (2.4) with the matrix Eq. (2.9) we obtain the second-harmonic po-

larization to be given by

$$\begin{pmatrix} P_x(2\omega) \\ P_y(2\omega) \\ P_z(2\omega) \end{pmatrix} = 2\epsilon_0 \begin{pmatrix} 2d_{31}E_xE_y \\ 2d_{13}E_yE_z \\ d_{31}(E_x^2 + E_y^2) + d_{33}E_z^2 \end{pmatrix} = \epsilon_0 \begin{pmatrix} 2\chi_{zxx}E_xE_y \\ 2\chi_{xzz}E_yE_z \\ \chi_{zxx}(E_x^2 + E_y^2) + \chi_{zzz}E_z^2 \end{pmatrix}. \quad (2.10)$$

2.2 Angular dependence of SHG

In this work we generally probe thin nonlinear films deposited on linear transparent substrates to study the second-order nonlinear response as a function of angle of incidence of the fundamental electromagnetic field. In this four layered system (air, film, substrate, and air) the Maxwell equations require that the second-harmonic field must satisfy

$$\nabla \times \nabla \times \vec{E}^{(2)}(\vec{r}, t) - \left(\frac{2\omega}{c^2}\right)^2 \overset{\leftrightarrow}{\epsilon}_2 \cdot \vec{E}^{(2)}(\vec{r}, t) = 4\pi \left(\frac{2\omega}{c}\right)^2 \vec{P}^{(2)}(\vec{r}, t). \quad (2.11)$$

Here $\overset{\leftrightarrow}{\epsilon}_2$ is the permittivity tensor at 2ω . Solving the boundary value problem of the fundamental and of the second-harmonic frequencies (Eq. (2.11)) for this system, Herman and Hayden³⁹ showed that in the no-depletion limit for an isotropic absorbing medium on a linear transparent substrate the transmitted second-harmonic polarization is given by Eq. (B11) in Ref.³⁹. When assuming that the reflective second-harmonic generated signal from the nonlinear film is close to zero then Eq. (B11) reduces to

$$P_{2\omega}^{\gamma \rightarrow p} = \frac{128\pi^3}{cA} \frac{[t_{af}^{1\gamma}]^4 [t_{fs}^{2p}]^2 [t_{sa}^{2p}]^2}{n_2^2 c_2^2} P_\omega^2 \left(\frac{2\pi L}{\lambda_p}\right)^2 d_{\text{eff}}^2 \exp[-2(\delta_1 + \delta_2)] \frac{\sin^2 \Psi + \sinh^2 \Omega}{\Psi^2 + \Omega^2}. \quad (2.12)$$

Here the effective nonlinear coefficient d_{eff}^2 for $C_{\infty v}$ space symmetry, see matrix (2.9), as a function of angle of incidence is given as

$$d_{\text{eff}}^{\gamma \rightarrow p} = \begin{cases} 2d_{15}c_1s_1c_2 + d_{31}c_1^2s_2 + d_{33}s_1^2s_2 & \gamma \rightarrow p \\ d_{31}s_2 & \gamma \rightarrow s \end{cases} \quad (2.13)$$

where $d_{15} = d_{31}$, when Kleinman symmetry is valid. The γ denotes if the fundamental field is s - or p -polarized. The Fresnel transmission coefficients at the fundamental and second-harmonic generated field are denoted as $t^{1\gamma}$ and t^{2p} , respectively, and subscripts af, fs and sa refer to air-film, film-substrate and substrate-air interfaces,

respectively. Furthermore,

$$\begin{aligned} s_m &= 1/n_m \sin(\theta), \\ c_m &= \sqrt{1 - s_m^2}, m = 1, 2, \\ \Psi &= (2\pi L/\lambda)(n_1 c_1 - n_2 c_2), \\ \Omega &= \delta_1 - \delta_2 = 2(\pi L/\lambda)(n_1 \kappa_1/c_1 - n_2 \kappa_2/c_2). \end{aligned}$$

Here θ is the angle of incidence of the fundamental wavelength. The subscripts $m = 1$ and $m = 2$ denote the fundamental and second-harmonic fields, respectively. Therefore, by measuring the nonlinear response from a sample, with the above mentioned symmetries, allows for estimation of the nonlinear coefficients d_{31} and d_{33} if the linear optical properties are known. However, precise estimation of P_ω and the Gaussian beam area A probing the sample is necessary.

A more precise method to estimate the effective nonlinear coefficient d_{eff} is by comparing the second-harmonic generated signal from a quartz disk to the nonlinear signal from a SiO film. Jerphagnon and Kurtz⁴⁰ showed that the second-order polarization from a probed quartz crystal has the form

$$\begin{aligned} P_{2\omega}^{p \rightarrow p}(\text{quartz}) &= \frac{512\pi^3}{cA} \frac{[t_{af}^{1p}]^4}{(n_1^2 - n_2^2)^2} \frac{2n_2 \cos \theta_2 (n_1 \cos \theta + \cos \theta_1)}{(\cos \theta_2 + n_2 \cos \theta)^3} \\ &\times (n_2 \cos \theta_1 + n_1 \cos \theta_2) d_{11}^2 P_\omega^2 \exp[-(L^2/w^2) \cos^2 \theta (\tan \theta_1 - \tan \theta_2)^2] \\ &\times \sin^2(2\pi L/\lambda)(n_1 \cos \theta_1 - n_2 \cos \theta_2), \quad (2.14) \end{aligned}$$

where θ_1 and θ_2 are the refractive angles of the fundamental and second-harmonic fields. The last term in Eq. (2.14) is the oscillating term resulting in Maker fringes. Setting this term to 1 and $\theta = 0^\circ$ (normal incidence) yields the maximum expected signal from the quartz crystal

$$P_{2\omega}^{p \rightarrow p}(\text{quartz}) = \frac{512\pi^3}{cA} \frac{16}{(n_1 + 1)^3(1 + n_2)^3} \frac{2n_2(n_2 + n_1)}{(n_1^2 - n_2^2)^2} d_{11}^2 P_\omega^2. \quad (2.15)$$

Dividing Eq. (2.15) into Eq. 2.12 the constants A and P_ω disappears leaving only d_{eff} as an unknown parameter, if the ratio $P_{2\omega}/P_{2\omega}(\text{quartz})$ is measured experimentally. Using the value $d_{11} = 0.31$ pm/V reported by Hagimoto and Mito⁴¹ for quartz at an excitation wavelength of 633 nm, and considering Miller's Δ ³⁰

$$\Delta_{ijk} = \frac{d_{ijk}}{[n_i^2(2\omega) - 1][n_j^2(\omega) - 1][n_k^2(\omega) - 1]}. \quad (2.16)$$

which is nearly constant for all noncentrosymmetric crystals. Using Δ to compensate for dispersion in d_{11} for quartz the above considerations enable one to estimate d_{eff} at a given excitation wavelength when compared to crystalline quartz. This technique was utilized in App. A and the result is discussed in chap. 4.

2.3 Rotation of the second-order nonlinear susceptibility tensor

The SHG response and its variation with rotation of the sample around the surface normal depends on the orientation of the symmetry directions in the material. This will be used in Chapter 5 in the analysis of films deposited at oblique angles. Figure 2.2 illustrates the nonlinear susceptibility tensor in a particular direction

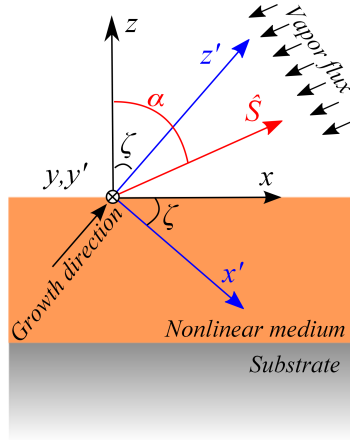


Figure 2.2: OAD growth of a thin film with the incident flux anti-parallel to \hat{S} at an angle α relative to the surface normal and the growth direction of columns along the \hat{z}' axis making an angle β with the surface normal. The direction of broken symmetry, defined by ζ , coincides with β in (a). Note, however, that this cannot be assumed a priori. For this reason we distinguish between these angles.

defined by the Cartesian coordinate system (x', y', z') , where the angle between the z - and z' -axis is ζ . It is therefore more convenient to rotate the direction of the induced nonlinearity into the laboratory coordinate system (x, y, z) , through a simple rotation matrix

$$\mathbf{R} = \begin{pmatrix} \cos \zeta & 0 & -\sin \zeta \\ 0 & 1 & 0 \\ \sin \zeta & 0 & \cos \zeta \end{pmatrix}. \quad (2.17)$$

Hence, the second-order nonlinear susceptibility tensor $\chi_{x'y'z'}^{(2)}$ is rotated with the angle ζ around to y -axis (or y' -axis) by

$$\begin{aligned}\chi_{abc}^{(2)} &= \sum_{i'j'k'} R_{i'a} R_{j'b} R_{k'c} \chi_{i'j'k'}^{(2)} \\ &= R_{x'a} R_{x'b} R_{x'c} \chi_{x'x'x'}^{(2)} + R_{x'a} R_{x'b} R_{y'c} \chi_{x'x'y'}^{(2)} + R_{x'a} R_{x'b} R_{z'c} \chi_{x'x'z'}^{(2)} \\ &\quad + R_{x'a} R_{y'b} R_{x'c} \chi_{x'y'x'}^{(2)} + R_{x'a} R_{y'b} R_{y'c} \chi_{x'y'y'}^{(2)} + R_{x'a} R_{y'b} R_{z'c} \chi_{x'y'z'}^{(2)} \\ &\quad + R_{x'a} R_{z'b} R_{x'c} \chi_{x'z'x'}^{(2)} + R_{x'a} R_{z'b} R_{y'c} \chi_{x'z'y'}^{(2)} + R_{x'a} R_{z'b} R_{z'c} \chi_{x'z'z'}^{(2)} + \dots\end{aligned}\quad (2.18)$$

This yields a total of 27 elements, however, when considering $C_{\infty v}$ space symmetry the above reduces to

$$\begin{aligned}\chi_{abc}^{(2)} &= (R_{x'a} R_{x'b} R_{z'c} + R_{y'a} R_{y'b} R_{z'c} + R_{x'a} R_{z'a} R_{x'x} + R_{y'a} R_{z'b} R_{y'c}) \chi_{x'x'z'}^{(2)} \\ &\quad + (R_{z'a} R_{x'b} R_{x'c} + R_{z'a} R_{y'b} R_{y'c}) \chi_{z'x'x}^{(2)} \\ &\quad + R_{z'a} R_{z'b} R_{z'c} \chi_{z'z'z'}^{(2)}.\end{aligned}\quad (2.19)$$

yielding a total of 14 non-vanishing element contra the 3 in $C_{\infty v}$ space symmetry with a direction perpendicular to the surface plane, thus, illustrating the complexity pointed out around Eq. 1 in App. B. A more convenient way of presenting Eq. (2.19) is

$$\chi_{abc}^{(2)} = \begin{pmatrix} R_{x'a} R_{x'b} R_{z'c} + R_{y'a} R_{y'b} R_{z'c} + R_{x'a} R_{z'a} R_{x'x} + R_{y'a} R_{z'b} R_{y'c} \\ R_{z'a} R_{x'b} R_{x'c} + R_{z'a} R_{y'b} R_{y'c} \\ R_{z'a} R_{z'b} R_{z'c} \end{pmatrix} \begin{pmatrix} \chi_{x'x'z'}^{(2)} \\ \chi_{z'x'x}^{(2)} \\ \chi_{z'z'z'}^{(2)} \end{pmatrix}\quad (2.20)$$

$$= 2\mathbf{Q} \begin{pmatrix} d_{x'x'z'}^{(2)} \\ d_{z'x'x}^{(2)} \\ d_{z'z'z'}^{(2)} \end{pmatrix}\quad (2.21)$$

Adopting this new rotated tensor $\overset{\leftrightarrow}{\chi}_{abc}^{(2)}$ to the work of Herman and Hayden³⁹, it becomes possible to model the second-harmonic response from a medium with an induced nonlinearity in a particular direction as illustrated in Fig. 2.2. This will be discussed further in Chap. 4 and App. B.

2.4 Electric field induced second-harmonic generation

Inversion symmetry of a centrosymmetric material can be broken by inducing an dc-field within the media, which results in SHG. An induced dc-field can for instance be obtained through a polling process. This otherwise centrosymmetric material

will now have a SH response, since a space charge region is created allowing for second-harmonic polarization given by⁷

$$P_i^{(2)}(2\omega) = \epsilon_0 \sum_{jkl} \chi_{ijkl}^{(3)} E_j(\omega) E_k(\omega) E_l^{dc} \quad (2.22)$$

where E_l^{dc} is the component of the dc field \vec{E}_{dc} . Moreover, notice that the electric-field induced second-harmonic (EFISH) polarization is dependent on $\chi^{(3)}$, which is a consequence of the material being centrosymmetric. This will be discussed in further details in Chap. 5 and App. C.

Experimental techniques

This chapter gives a short presentation of the electron beam deposition system used to deposit silicon monoxide thin films along with the atomic layer deposition process used to produce ZnO thin films. The different thin film characterization techniques used to characterise the synthesised thin films are presented. More importantly, a detailed description of the experimental nonlinear optical setups is outlined at the end of the chapter.

3.1 Electron beam deposition technique

Prior to any thin film deposition onto a substrate, proper surface cleaning of the substrate is necessary. Mainly fused silica and silicon (001) have been used as substrates in this work. Prior to deposition they were treated with acetone for 2 minutes in an ultrasonic to remove organic material. Thereafter, the samples were showered with milli Q water followed by a 2 minutes ultrasonic bath in ethanol to remove acetone and/or organic leftovers. Between every step the substrates were blow dried with dry N₂.

Figure 3.1(a) illustrates (not to scale) the main components of the electron beam deposition system Cryofox. The substrates can be loaded into the deposition chamber through a load lock. A -7.5 kV electron beam, deflected by controlled magnetic fields, can be swiped across a graphite crucible filled with target material. Bombarding the target SiO material with electrons will heat SiO grains so it will evaporate towards the substrates kept at room temperature. Normally the

background deposition pressure is $\sim 1 \cdot 10^{-6}$ mbar, which yields a very high mean-free-path resulting in the SiO vapour arriving on a "line-of-sight" from the crucible to the substrate. Charging effects are inevitably going to occur when bombarding isolating SiO grains. Therefore, during the deposition start one must gently increase the current of the -7.5 kV electrons from 0 mA to ~ 20 mA, which normally leads to a deposition rate of $\sim 1 \text{ \AA/s}$. If the current is increased too fast, the 3-5 mm large SiO grains in the crucible will repel each other, and the crucible will empty fairly quickly due to jumping SiO grains. During the deposition the SiO grains tend to move slightly around in the crucible, therefore, one must carefully monitor the deposition rate and then compensate by changing the position of the sweeping electron beam manually. This is a somewhat tricky business, nonetheless, once it is mastered the optical properties of the SiO are reproducible. Even with large variations in deposition rate the important second harmonic response from the SiO thin films is still intact. All substrate cleaning routines and SiO depositions were performed in a cleanroom environment.

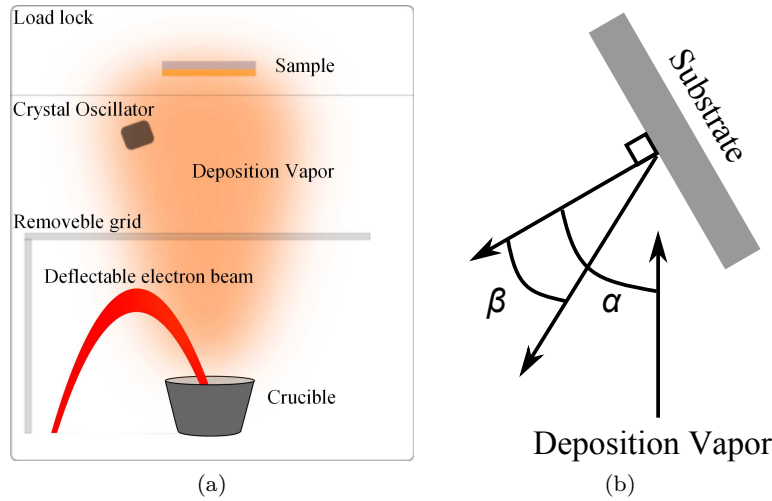


Figure 3.1: (a) A rough sketch of the electron beam deposition system Cryofox. (b) demonstrating the principle behind oblique angle deposition. Here, α is the deposition angle and β is the growth direction both measured from the surface normal.

During atypical electron beam deposition, large amounts of stray charged particles are expected to be present. A retarding grid ($\sim 50\%$ transmittance) was inserted in-between the source and target with the same -7.5 kV applied on it. This should capture all the negatively charged particles created by the electrons, which also evaporate towards the substrate. This could actually be confirmed by the naked eye; with the inserted retarding grid a cone like blueish plasma ascending

from the crucible was visible, consistent with the colours of an oxygen plasma. This is discussed in further detail in App. A.

Oblique angle deposition (OAD) was used to produce a series of SiO and ZnO thin films. The basics behind OAD is illustrated in Fig. 3.1(b), where the substrate simply is tilted at an angle α measured from the substrates normal. The resulting thin film is a porous columnar structure that is tilted with an angle β , which normally is smaller than α . Unfortunately, the Cryofox deposition system was not designed for oblique angle deposition. However, an aluminum substrate holder enabled eight pairs of fused silica and silicon substrates to be placed simultaneously at different α during deposition. Thus, SiO was deposited simultaneously onto substrates placed at the angles $\alpha = 0^\circ, 10^\circ, 20^\circ, 30^\circ, 45^\circ, 60^\circ, 70^\circ$ and 80° with a estimated accuracy of $\pm 1^\circ$.

The Cryofox deposition is actually used for many different types of material deposition, from noble metals and semiconducting materials to different types of glass. Furthermore, rf/dc-magnetron sputtering is also possible with the same deposition system. This could naturally be an issue, since impurities may get incorporated into the SiO thin films. However, after a total system cleaning, prior to a SiO deposition, the strong second harmonic response from the sample was still present. Thus, it can be ruled out that unwanted deposition materials inside the SiO film is source of the nonlinearity.

3.2 Atomic layer deposition

Atomic layer deposition (ALD) is based on a gas phase chemical process, similar to chemical vapour deposition (CVD), where different reactants are introduced to at substrate surface. However, in an ALD process the substrate surface is exposed for short periods of time to the reactants. For instance, the thin polycrystalline ZnO films for this study were synthesized by subsequently exposing the surface to $(\text{C}_2\text{H}_5)_2\text{Zn}$ as the metal precursor for 30 ms, followed by H_2O (oxidant) for 20 ms. In-between and after these reactants, the deposition system was purged with dry nitrogen. This sequence is called a cycle, where an atomic layer of Zinc is deposited followed by an oxygen atomic layer. Hence an ALD process builds the thin film, atomic layer by atomic layer. By increasing the number of cycles one can in a very controlled manner choose a desired film thickness. The *n*-type Si(100) substrate temperature was 200°C and an Oxford Instruments OpAL reactor was used to perform the depositions. For more details on the ALD process see⁴².

3.3 Structural properties

The nanostructural properties of a thin film can have a pronounced effect on the optical properties. It is therefore important to characterise the structural properties

of the SiO and ZnO films to better understand the optical response.

Scanning electron microscopy (SEM) and transmission electron microscopy (TEM) are imaging techniques based on electrons interacting with a sample, and thereby the atoms within the sample. TEM has a higher resolution compared to SEM and can be used to identify the crystalline nature of a film and even crystal planes can be identified. X-ray diffraction (XRD) can reveal, if different types of crystal growth planes are present within a film, since the diffraction angle of the incident x-rays reveals the growth direction of the crystals planes. Atomic force microscopy (AFM) can be used to identify the surface morphology of a given sample by tapping a very sharp and very well defined needle, where the change in trapping behaviour is a direct measurement of the surfaces hills and valleys.

Besides the structural characterization techniques a few destructive compositional characterization techniques have been used. In a Rutherford backscattering spectroscopy (RBS) measurements, He^+ ions are accelerated toward a sample (target) with an energy of $E_0 = 2$ MeV. By analysing the backscattered energy E_1 of the He^+ ions from the sample, one can gain insight into the composition of the sample by

$$E_1 = \left(\frac{m_1 \cos(\theta_1) \pm \sqrt{m_2^2 - m_1^2 \sin^2(\theta_1)}}{m_1 + m_2} \right)^2 E_0. \quad (3.1)$$

Here, θ_1 is the backscattering angle of the He^+ ions with the mass m_1 , and m_2 being the mass of target nucleus. Hence, the only unknown parameter is m_2 as θ_1 is defined by the placement of the detector. Analysing a SiO thin film deposited on silicon has several advantages. A doped silicon substrate is conducting, thus, changing effects from the ions will be minimized compared to the fused silica substrate. All the RBS spectra presented in this thesis have been analysed using the software RUMP⁴³.

RBS has its limitations, if the nucleus of interest has a very low mass. Here, secondary ion mass spectroscopy (SIMS) fills the gap and has a sensitivity down to 10^8 atoms/cm².⁴⁴ By bombarding a selected area of a sample, with a focused caesium ion beam, will sputter off the surface material, and by using a mass spectrometer, these off sputtered secondary ions can be identified as a function of depth in the sample.

3.4 Linear optical characterization technique

The linear optical properties and thickness of the SiO and ZnO thin films were determined with spectroscopy ellipsometry (SE) measurements. The Jellison and Modine model⁴⁵ was used to represent the thin films on silicon substrates.

A Perkin-Elmer lambda 1050 spectrometer with an integrating sphere setup was used for transmission/reflection spectroscopy. This can also give an estimation of

the absorption as a function of wavelength for a given sample on a transparent substrate. With the dual beam setup any fluctuation during a measurement can be normalised out, thus, making the spectrometer a powerful tool to perform time-dependent measurements, as will be demonstrated in Chap. 4.

3.5 The nonlinear optical techniques

A general outline of the transmittance SHG optical setups is presented in Fig. 3.2. Two different laser systems have been used; a Nd:YAG-laser pumped optical parametric oscillator (OPO) system delivering 5-ns (spectral bandwidth <1 nm FWHM) pulses at 10-Hz repetition rate and a mode-locked Ti:Sapphire laser (Spectra-Physics Tsunami) delivering 100-fs (spectral bandwidth ~ 12.5 nm FWHM) at 80-Hz repetition. The mean power output for the latter system is very constant over time and has therefore mainly been used for the time-dependent SHG measurements and 2D scans. The Nd:YAG system setup was mainly used for spectral investigations due to the very narrow spectral pulse width.

In all the cases a Fresnel rhomb was used to control the polarisation of probing laser field that is focused onto the sample. A polariser was placed directly after the Fresnel rhomb to ensure a s- or p-polarisation of the incident laser field. This combination enabled one to control the power of the laser field by rotating the Fresnel rhomb behind the polariser, which was locked at a particular polarisation direction.

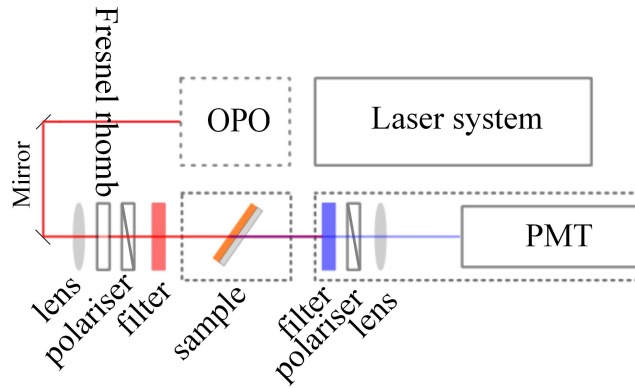


Figure 3.2

Extraction of the SHG field from the transmitted fields was done with a few combinations of coloured glass filters to cover the investigated spectral region, see table 3.1 for the used combinations. A longpass filter right before the sample was used to remove any SHG light generated by the optics in the beam path and

Fundamental wavelength	Filters after sample	Filters before sample
550 nm–700 nm	2 mm UG11x + 3 mm UG11	Hot mirror filter + 3 mm OG515
720 nm–1000 nm	4×3 mm BG40	1×3 mm RG715
1000 nm–1400 nm	3 mm KG3	3 mm RG850

Table 3.1

shortpass filters after the sample enabled only the SHG light from the sample to pass through to the photo multiplier tube (PMT). In front of the PMT a polariser was used to analyse the polarisation of the SHG light. Therefore, it was possible to perform p-p, p-s, s-p and s-s measurements as a function of wavelength and angle of incidence with this setup. In a transmittance setup a successful extraction of the SHG signal is simply verified by removing the sample from the beam path and then hopefully observing no measurable signal. Furthermore, by placing a monochromator in front of the PMT to investigate the spectral composition of the measured signal, one can confirm if or if not it is a SHG signal.

A trigger signal from the Nd:YAG-laser was used to gate the 10-Hz 5-ns generated SH signal measured by the PMT. The timing was monitored by an oscilloscope and was controlled by a SRS boxcar. Every data point measured with the Nd:YAG-laser system is an average of 100 pulses per position or wavelength, hence, 10 seconds is needed for every data point, in order to give sufficient statistics. Placing a wedge-

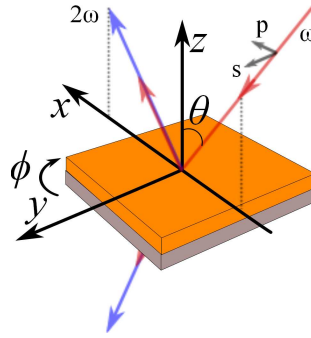


Figure 3.3: Demonstrating the geometry of a sample in the optical setups.

shaped crystal in the same location as the samples gives a normalizing reference signal without Maker fringes. This removes all laser, filters, lens, polariser and detector spectral variations by normalizing the SHG spectral response from a SiO

sample to the relatively flat spectral SHG response from a quartz crystal.

As has been demonstrated in Chap. 2 and what will be shown in Chap. 4 the SHG signal is strongly dependent on the angle of incidence of the pump field. Therefore, changing the angle of incidence (AOI) of the probing laser beam can give great insight into the origin to the SHG signal from a sample. For practical reasons, this is performed by rotating the sample with an angle θ about the y -axis, see Fig. 3.3. For the azimuthal measurements the sample is rotated an angle ϕ around the z -axis. For the oblique angle deposited SiO thin films great attention is needed to the direction of α when placing the samples in the SHG optical setup. For all the AOI measurements performed in App. C the growth direction α is tilted towards the x -axis, hence, the columns are parallel to the xz -plane; more details are given in App. B.

For the measurements on ZnO the time-dependent SHG experiments were performed in reflection mode using the a mode-locked Ti:Sapphire laser delivering p-polarized pulses with a photon energy of 1.675 eV ($\lambda = 740\text{nm}$) focused onto the sample with a doublet lens (focal length 200 mm) resulting in an average laser intensity varying from 10 to 50 MW/cm². Colored glass filters (Schott BG40) were used to separate the excitation radiation from the second-harmonic (SH) radiation. The SHG signal was detected with a photomultiplier tube coupled to single photon counting electronics. The angle of incidence of the laser beam was 30° except for the measurements in which the surrounding ambient of the sample was changed by using a closed chamber. In these experiments the sample was placed at 45° angle of incidence. The chamber could be purged with dry nitrogen, and air could be reintroduced through a valve.

Second-harmonic generation from SiO

4.1 Introduction

This chapter presents the study of the second-harmonic generation from SiO prepared by electron beam deposition. We will start with the realization that the SiO thin films has an effective second order nonlinearity giving rise to an efficient bulk SHG response. It was realized that the nonlinearity arises due to the deposition conditions. It is thus not necessary to apply electrical contacts and a thermal post deposition process as in conventional poling to arrive at a bulk SHG. Furthermore, the electron beam deposition allows straight forward use of conventional lithography for in-plane definition of nonlinear optical elements. The inversion symmetry of SiO is broken perpendicular to the surface which is similar to that of poled materials. One can thus consider the same type of active optical components consisting of SiO films as from poled glass films.

We move on to demonstrate that this unique nonlinear optical response of electron beam deposited SiO can be tuned through a simple oblique angle deposition (OAD) technique. OAD deposition typically leads to a porous tilted structure. By observing the angular dependency of the nonlinear response as a function of angle of incidence of the probing laser, the growth direction of these OAD SiO films can be revealed. Beside this unique nonlinear tunability, it was found that these porous OAD SiO thin films tend to oxidise when in contact with ambient air and that this

oxidation process can be studied with time-dependent second-harmonic generation as well as time-dependent linear optics.

Finally, this chapter ends by demonstrating that OAD of ZnO can also lead to a tunable second-harmonic response and by analysing the angular optical SHG response, one can also reveal the growth direction of the condensed ZnO film.

4.2 Second-harmonic generation from SiO

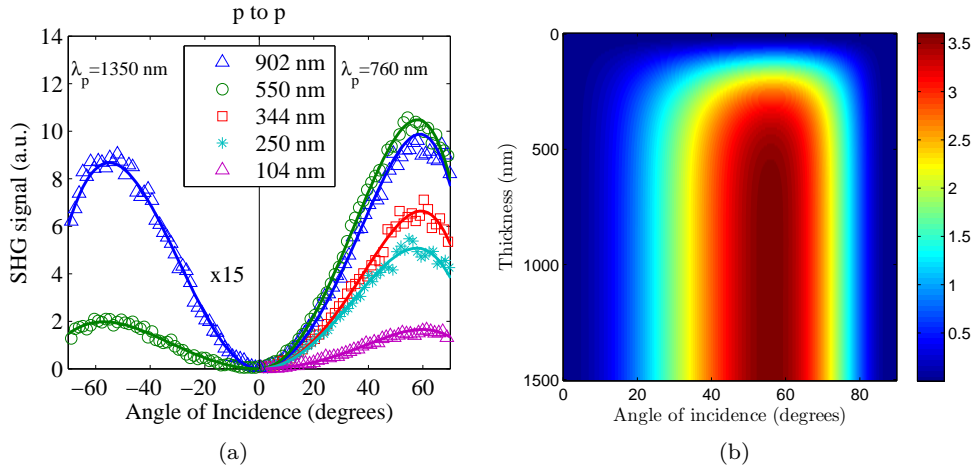


Figure 4.1: Angular dependency of the SHG signal from the SiO thin films (a) with the thickness between 104 nm to 902 nm. On the left hand side and the right hand side, respectively, 1350 nm and 760 nm excitation wavelength were used. Symbols are experimental results and the solid lines are the best fits using Eq. 2.12. Notice that a factor of 15 has been multiplied to the signal strength on the left hand side. (b) simulation (using Eq. (2.12)) of the SHG response as a function of angle of incidence and film thickness illustrating the saturation effect.

Through a standard electron beam deposition of silicon oxide ($\text{SiO}_{1 < x < 2}$) powder and/or grains onto a substrate, the condensed thin film has a strong bulk nonlinear response compatible to that of crystalline quartz. This is quite surprising, since SiO_x films are amorphous and therefore centrosymmetric on a macroscopic scale. The nonlinear properties of SiO thin films and the reason, why SiO films prepared with electron beam deposition are non-centrosymmetric, are outlined and discussed in App. A. However, the main results are highlighted here together with some unpublished results.

Figure 4.1(a) demonstrates the angular dependency of the SHG signal from SiO thin films with the thickness between 104 nm and 904 nm. From these results three important things are seen; first, the symmetry is broken perpendicular to the surface since the SHG signal dies when the probing laser angle of incidence is normal to the surface ($\theta = 0^\circ$). Second, the SHG signal is dependent on film thickness. Finally, SiO has a band gap, see Fig. 2 in App. A, which results in a saturation of the SHG signal due to linear absorption, see right hand side of Fig. 4.1(a). This effect is highlighted in Fig. 4.1(b) where a simulation of the SHG signal as a function of angle of incidence and film thickness shows the saturation effect when pumped with the wavelength of 760 nm. Choosing a pump wavelength so the second-harmonic generated photon energy is below the band gap, the quadratic behaviour is intact, as demonstrated in the left hand side of Fig. 4.1(a). Nonetheless, the effective nonlinear coefficient was determined to $d_{\text{eff}} = 0.2 \text{ pm/V}$ at a pump wavelength of 760 nm, which is comparable to non-centrosymmetric crystals, see App. A for further details.

It is suggested that the non-centrosymmetry is related to orientated Si-H and O-H bonds. During the deposition a flux of negative oxygen ion is created by the -7.5 kV electron beam sweeping the SiO grains in the crucible. This was verified by placing a retarding grid between the crucible and substrate, see Fig. 6 in App. A. With the retarding grid a blueish plasma became visible from the crucible, which is consistent with a oxygen plasma. Besides charging the surface of the substrate these oxygen ions will penetrate the SiO film as it evolves on the substrate. By assuming that a potential U between the substrate and the crucible is comparable to the e-beam acceleration voltage and neglecting thermal effects, the oxygen ion will be accelerated towards the substrate with the kinetic energy of

$$K = \frac{1}{2}mv^2 = eU = 7.5 \text{ keV}. \quad (4.1)$$

Figure 4.2(a) demonstrates the simulated penetration depth and profile of the oxygen ions, and Fig. 4.2(b) shows the corresponding vacancies created within the SiO film, when assuming the oxygen ion have a kinetic energy of 7.5 keV. The simulation was performed with the freeware program SRIM⁴⁶. Clearly, defect formation created by the penetrating oxygen ions is present, thus, from the simulations it is expected that an almost uniform distribution of vacancies throughout the SiO film is present. These vacancies may become passivated by hydrogen atoms⁴⁷, hence, formation of Si-H and O-H bonds may occur.

In Fig. 4.3(a) a secondary ion mass spectroscopy (SIMS) measurement shows the composition of a 220 nm thick SiO sample deposited on fused silica (SiO_2). The fast oscillations seen in the data are due to charge effects since the sample is bombarded with negative caesium ions to sputter material off from the SiO sample. Therefore, a thin gold (Au) layer was deposited on top of the SiO film to minimize this effect.

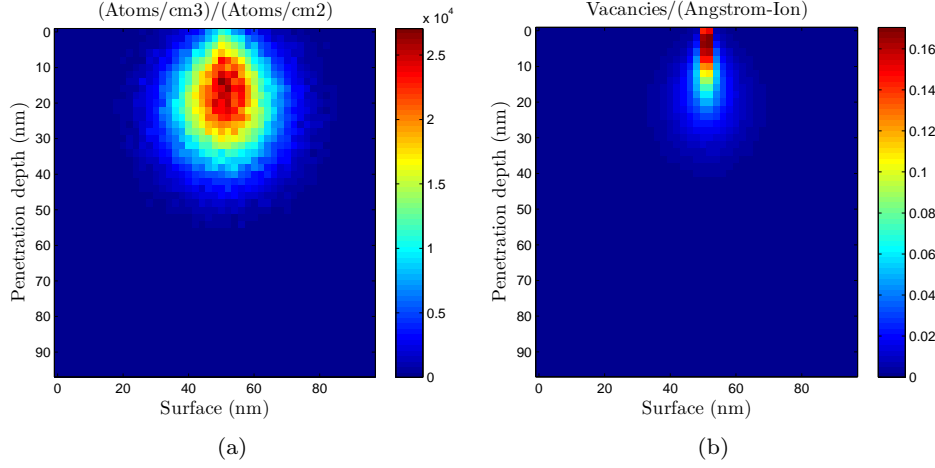


Figure 4.2: (a) Penetration profile of 7.5 keV oxygen ions in a SiO film (b) vacancy distribution generated due to collisions between oxygen ions and the Si and O atoms in the SiO film.

Apparently, an uniform distribution of hydrogen content throughout the sample is present. This confirms the presence of hydrogen bonds and the model proposed in App. A. A continuous flux of negative oxygen ions during the depositing leads to defect formation that is passivated with hydrogen bonds, and the associated charging of the film may orient these Si-H bonds resulting in non-centrosymmetric film.

As expected carbon (C) is located on the SiO₂ substrate surface as seen in Fig. 4.3(a), however, variations in C content in the SiO film is related to changes in the deposition rate. With a slower deposition rate more C will be present in the film.⁴⁸ Hence, this sample is synthesized with variations in the deposition rate. Moreover, variations in Si and O are seen and a slight increase in O content is accompanied by an increase in C content, hence, formation of C-O bonds occurs. Moreover, at the same time a decrease in Si content is seen. With a slower deposition rate, more C is located at the surface, and if it is energetically favourable to form C-O bonds instead of Si-O bonds, Si atoms will accumulate on the growing surface. Therefore, with a drop in C contents an increase in Si contents occurs.

By comparing the ratio between the counts of Si and O in the SiO₂ substrate and in the SiO thin film one can get a rough estimate of the stoichiometry of the SiO film. It was found that $(\text{Si}/\text{O})_{\text{SiO}_2} / (\text{Si}/\text{O})_{\text{SiO}} = 1.8 \pm 0.4$, thereby indicating that the SiO thin film is in fact a silicon monoxide. It was confirmed with Rutherford backscattering spectroscopy (RBS) that electron beam deposition of SiO grains leads to a silicon monoxide film. Figure 4.3(b) shows a spectrum from a 280 nm

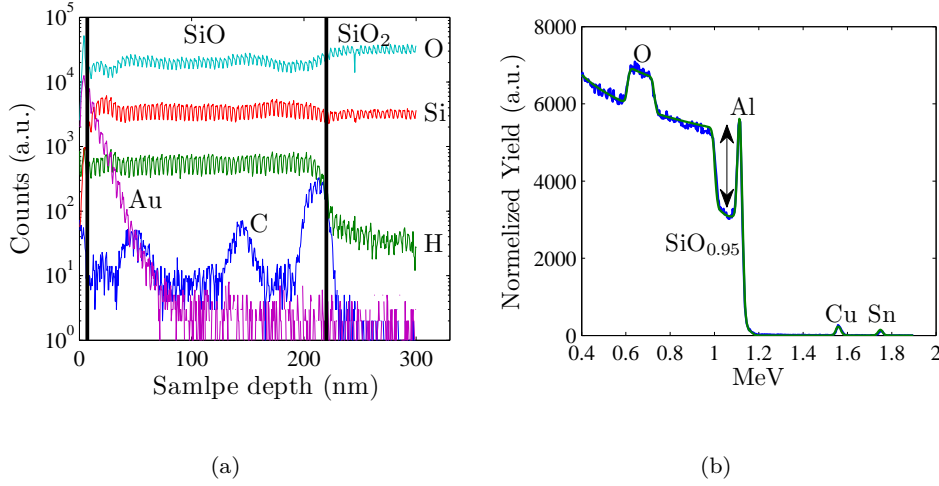


Figure 4.3: (a) Secondary ion mass spectroscopy of a 220 nm thick SiO sample displaying a uniform hydrogen content. Variations in carbon contents is due to variation in deposition rate. Using the relationship between the Si og O counts measured in the SiO₂ film, the stoichiometry x in the SiO _{x} film is estimated to $x = 1.1$. (b) Rutherford backscatter spectroscopy of a 280 nm film with an aluminium film on top. The green curve is a simulation to the blue data. The x in SiO _{x} was estimate to 0.95 which is in a good agreement with SIMS.

thick film deposited on silicon. To reduce charging effects during the measurement, a 30 nm thick aluminium film (with the impurities Cu and Sn) was sputtered on top of the film. The blue and green curves are the measured data and a simulation to represent the experimental data, respectively. As briefly discussed in Chap. 3 the backscattering energy of the He⁺ atoms depends on the mass of the atoms present the film. Therefore, the depth of the dip in Fig. 4.3(b), indicated by the double arrow, depends on the number of oxygen atoms present in the SiO _{x} . It was found that the data could best be represented with a SiO_{0.95} film, which is consistent with the SIMS measurement.

By preparing a mixture consisting of SiO powder and SiO₂ powder as deposition target material one can synthesis a SiO _{x} film. Figure 1(a) in App. A shows the spectral SHG response from a SiO _{x} thin film pumped with $\lambda = 760\text{nm}$, however, a SiO₂ film prepared from SiO₂ grains lacked a measurable second-harmonic response. It is therefore speculated that the SHG signal strength is inversely proportional to the stoichiometry x , since the extra oxygen atoms will reduce the amount of Si–H bonds. As a side note it can be mentioned, that annealing a SiO _{x} in argon or nitrogen atmospheres at elevated temperatures ($\sim 1000^\circ\text{C}$) will transform the SiO _{x} film to a SiO₂ film where the excess Si atoms will cluster and form nanocrystals embed-

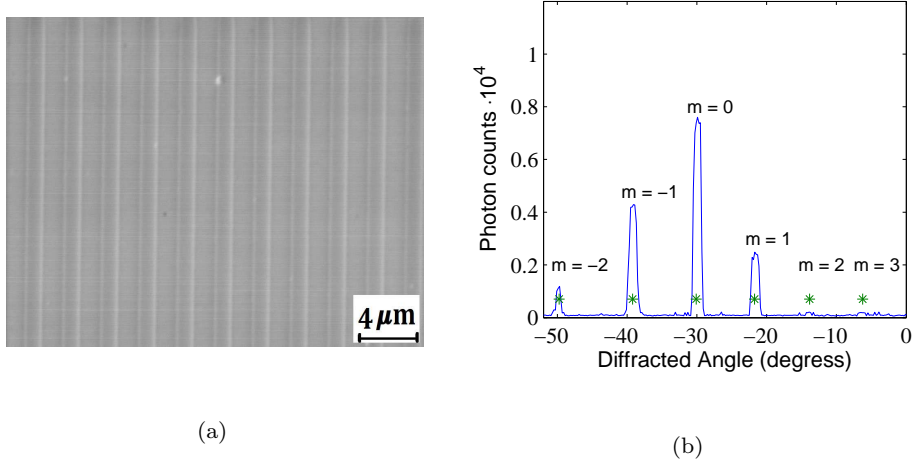


Figure 4.4: (a) SHG from SiO well defined 2D structure by e-beam lithography. (b) The SHG diffracted signal measured from a 90 nm thick SiO grating consisting of $1.4\ \mu\text{m}$ wide lines that are spaced $3\ \mu\text{m}$ apart.

ded in the SiO_2 matrix.^{49,50} Due to quantum confinement effects photoluminescence from this structure occurs when excited with a light source with a photon energy above the band gap. This was indeed the case for the annealed $\text{SiO}_{1.5}$ sample. When it was subjected to an excitation source of 488 nm (Argon ion CW laser) a clearly measurable PL was present thereby indicating formation of Si nanocrystals. However, when subjecting the SiO_x films to this annealing routine, it was found that the nonlinearity was reduced significantly, see Fig. 5 in App. A. Nonetheless, even after two years of storage at room temperature the SiO thin films still exhibit a strong measurable SHG response.

One of the advantages of direct deposition of a nonlinear film could be the possibility of defining structures on substrates by lithography. Using e-beam lithography well defined nonlinear 2D structures can be synthesized. Figure 4.4(a) shows a SEM image of a 90 nm thick SiO grating consisting of $1.4\ \mu\text{m}$ wide lines that are spaced $d = 3\ \mu\text{m}$ apart. The grating has a linear as well as a nonlinear response, and Fig. 4.4(b) shows the measured SHG diffracted signal from the SiO grating, here the green stars are the position of the predicted diffracted maxima. For further details see App. A.

4.3 Oblique angle deposited SiO

Electron beam oblique angle deposition (OAD) of SiO leads to a porous tilted structure with a non-centrosymmetry that is related to the structural properties of the SiO film. We demonstrated in App. B that by OAD the SH response can be easily be tuned through the deposition angle. Moreover, the measured angular SH response was fitted with the model presented in section 2.3 and the non-centrosymmetry direction showed to be related to the growth direction of the SiO. Therefore, by using SHG one can identify the growth direction of OAD SiO. The main results are highlighted in this section along with some few unpublished results.

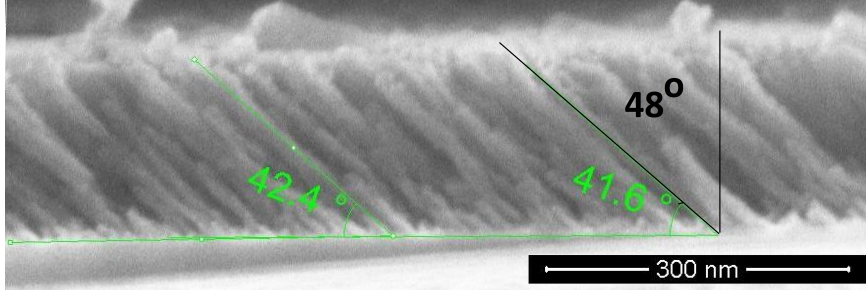


Figure 4.5: A cross sectional SEM image of a SiO thin film deposited on silicon with an oblique angle(α) of 80° . A columnar growth is seen tilted relative to the surface normal, β , $\sim 48^\circ$.

Figure 4.5 shows the tilting structure of a SiO film prepared with $\alpha = 80^\circ$. At this extremely oblique angle a columnar growth is seen and the structural tilting angle measured from surface normal is $\beta = 48^\circ$. By varying α one can control the structural properties of a film, see Fig. 1(b) in App. B.

In Fig. 4.6(a) the SHG signal from SiO thin films measured with 760 nm pump light as a function of angle of incidence from $\alpha = 0^\circ$ to $\alpha = 80^\circ$ is presented. With increasing α , the maximum at $\theta = +60^\circ$ decreases compared to the normalized maximum at $\theta = -60^\circ$. Notice that for $\alpha > 30^\circ$ at $\theta = 0^\circ$ (perpendicular to the surface) a measurable SHG signal exists. This feature is important for nonlinear optical devices. Clearly, the OAD films have a build-in anisotropy that is breaking the inversion symmetry in a particular direction. A simple model presented in Chap. 2 has been fitted to the SHG data in Fig. 4.6(a), solid lines are best fits, for further details see App. B. The results presented in Fig. 4.6(b) were obtained when Kleinman symmetry was assumed, thereby, only the tensor elements χ_{zzz} and χ_{zxx} and the angle ζ of the build-in anisotropy relative to the surface normal remain as fitting parameters. Moreover, it was assumed that the ratio between χ_{zzz} and χ_{zxx} was 3:1, however, for $\alpha > 45^\circ$ the ratio was also used as a fitting parameter to improve the fit. The fitted ratios can be found in Fig. 4.6(b). The estimated

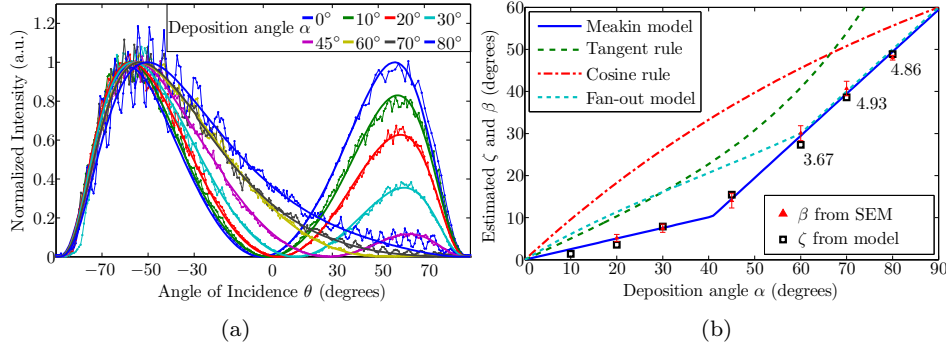


Figure 4.6: (a) The SHG signal as a function of θ . The solid lines are the best fits using the presented model in Chap. 2 yielding ζ which is plotted in (b) together with Meakin's model⁵¹, tangent rule⁵², cosine rule⁵³, the fan-out model⁵⁴ ($\phi = 60^\circ$), and the β values estimated by cross-sectional SEM imaging. The numbers are the estimated $\chi_{z'z'z'}/\chi_{z'x'x'}$ from the fit in (a).

ζ from the fitting routine are compared to the β measured from the SEM images. Clearly, there is a very close relation between β and ζ , and as discussed in App. B, the growth direction and the direction of induced nonlinearity are identical.

Figure 4.7 demonstrates p-p and s-p AOI measurements from the $\alpha = 30^\circ$ SiO sample performed 2 years later than the measurement shown in Fig. 4.6(a). Assuming Kleinman symmetry, then for the p-p case, only two independent tensor elements needs to be considered, namely χ_{zzz} and χ_{zxx} . For the s-p case only χ_{zxx} remains.³⁹ Hence, estimating χ_{zxx} from the s-p measurement and using it to perform a better fit of the p-p data should lead to a more exact estimate of the ratio χ_{zzz}/χ_{zxx} . Unfortunately when using the s-p χ_{zxx} a very poor fit (not shown) to the p-p measurement is achieved and it is uncertain why. The estimated growth direction ζ and the tensor elements χ_{zzz} and χ_{zxx} from the fits can be found in Fig. 4.7, where the estimated growth direction from p-p and s-p data are found to be identical within the uncertainties. Apparently, from the two year old sample the estimated growth direction is a bit larger than the original estimated $\zeta = 7.3^\circ$, see Fig. 4.6(b). It should be noted that the growth direction from the SEM images was estimated to $7.48 \pm 0.98^\circ$. On a side note, locking the χ_{zzz}/χ_{zxx} ratio to 3:1, as in Fig. 4.6(a), does not affect the resulting ζ . It is unclear why ζ , estimated from the 2 year old sample, differ from the originally estimate ζ directly after the deposition. However, it may be related to a change of the linear optical properties. Nonetheless, even after 2 years of storage, the non-centrosymmetry leading to a strong SHG signal is still present.

By this fairly simple oblique angle deposition technique one can tune the nonlin-

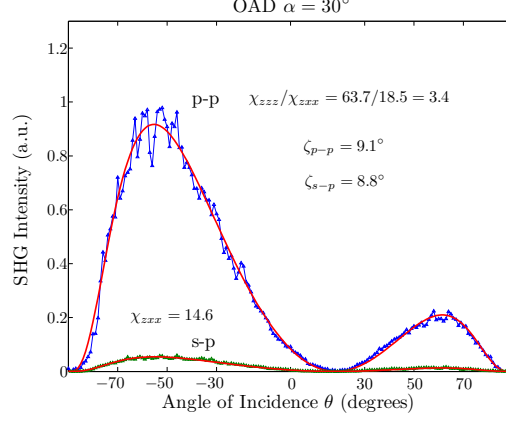


Figure 4.7: The p-p and s-p SHG signal as a function of angle of incidence. Here the data is fitted with Eq. (2.12) and combined with (2.21) and is displayed by the solid red curve. The measurements were performed 2 years later than the one shown in Fig. 4.1(a).

ear optical properties of the SiO films, thus, making SiO a very interesting material for future nonlinear optical devices. However, as discussed in App. B, the porous oblique angle deposited silicon monoxide tended to oxidise when in contact with ambient air. This will cause an uncertainty of the estimated ζ , since the linear optical properties changes during the oxidation process. Moreover, the oxidation of the samples was found to have a pronounced effect on the nonlinear optical response of the OAD SiO thin films.

4.4 Oxidation of oblique angle deposited SiO

This section presents preliminary results on oxidation of porous OAD SiO films that do not give a complete picture of the oxidation process. However, new interesting results have been obtained demonstrating that the process can be studied with linear optical spectroscopy and with second-harmonic generation.

The oblique angle deposited SiO films were found to oxidise when in contact with ambient air due to the porous structure. Only few studies on the oxidation dynamics of porous SiO_x can be found in the literature. Liao and Lee⁵⁵ demonstrated that porous silicon oxide films, prepared at low temperatures by plasma enhanced chemical vapour deposition, oxidises mainly due to water (H₂O) molecules reacting to Si-H bonds and -Si-Si- bonds. They showed that hydrogen diffuses out of the film as oxygen atoms in H₂O form bonds with the silicon atom in the Si-H bonds. However, intense work on the oxidation kinetics of a hydrogen terminated

Si surface⁵⁶, porous silicon^{57,58,59,60} and amorphous silicon^{61,62,63} can be found in the literature. If Si-H bonds are present in these silicon films, the same oxidation process as demonstrated by Liao and Lee takes place. Therefore, the oxidation dynamics in porous silicon and OAD SiO can be considered comparable. As the

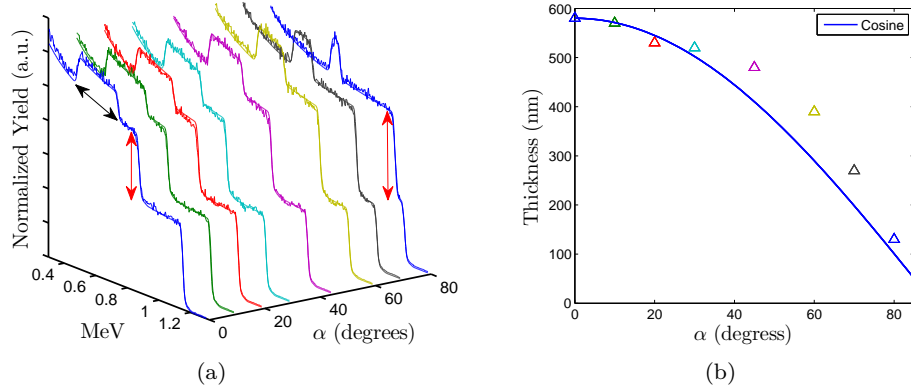


Figure 4.8: (a) RBS spectra measured 140 days after first contact with the ambient air. The smooth solid curves are simulations to the data yielding film thickness and the stoichiometry. (b) the film thickness estimated from (a) that follows a cosine behaviour.

OAD SiO samples are removed from the deposition chamber the samples changed from a brownish yellow colour to almost being transparent for large α . Figure 4.8(a) shows RBS spectra measured 140 days after first contact with ambient air. The smooth curves overlaying the data are simulations, which is used to estimate the stoichiometry and thickness of the SiO thin films. The black arrow illustrates the width of the oxygen peak which is a measure of the film thickness. The estimated thickness is plotted in Fig. 4.8(b) and it decreases with a $\cos(\alpha)$ behaviour as seen elsewhere⁶⁴. The height of the red arrow is a measure of x in SiO_x , see Fig. 4.9(b) for the plotted x . The observed difference is due to a variation in porosity, which is a function of α .

The absorbance spectra measured 144 days after the deposition confirms the RBS data, see Fig. 4.9(a). The absorbance is shifted towards the UV depending on α (or porosity). This corresponds to the SiO films oxidising towards an SiO_2 which has an absorption edge around 5 eV. The energy band gaps E_g from the SiO_x films are estimated by a Tauc plot⁶⁵ and are plotted in Fig. 4.9(c). Plots of the stoichiometry as a function of energy band gaps shows a saturation behaviour, see Fig. 4.9(d). These structural and linear optical changes due to reactions with the ambient air were found to be permanent. Furthermore, the oxidation process is

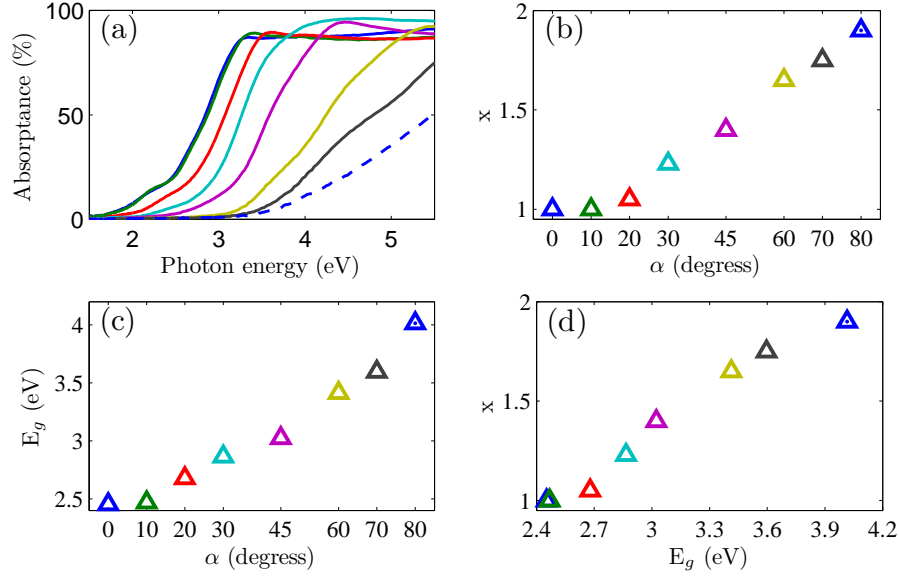


Figure 4.9: The optical and stoichiometric properties of samples $\alpha = 0^\circ$ to $\alpha = 80^\circ$ estimated 140 days and 144 days, respectively, after first contact with the ambient air. (a) The absorbance as a function of photon energy and the corresponding energy band gap E_g estimated by a Tauc plot can be found in (c). The estimated stoichiometry x in SiO_x as a function of α see (b), and as a function of E_g see (d).

strongly dependent on α , and thus the porous structure of the OAD SiO thin films.

Figure 4.10 shows a top view SEM image of sample $\alpha = 70^\circ$ with a very thin Au film coated on top in order to gain a high imaging contrast in SEM. A columnar structure with a relative large spacing between the individual columns exists, which gives a very large surface contact area to the ambient air.

The overall speculated oxidation process is illustrated in Fig. 4.11. As H_2O molecules diffuse into the porous columnar structure they attack the Si-H bonds and the SiO films is converted to SiO_x films on a prolonged time scale. However, directly after the samples are removed from the deposition chamber, the top part of the sample tends to oxidise as speculated in Fig. 4.11(b). On a minute time scale H_2O molecules will surround the columns and it is therefore assumed that the columnar surface oxidises homogeneously from top to bottom for large α . This is a fair assumption when considering the structure seen in Fig. 4.10, and since the RBS spectra reveal homogeneous oxidation of the OAD films. It is therefore

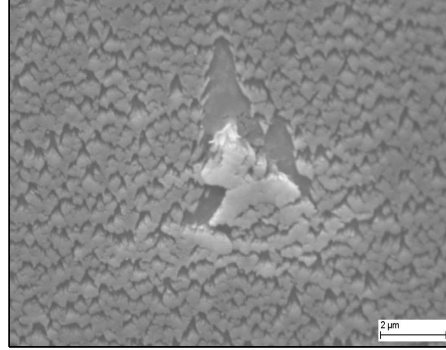


Figure 4.10: Topview SEM image of $\alpha = 70^\circ$. The large SiO particle in the centre of the image is formed due to surface impurities on the substrate. This particle allowed for a higher contrast resulting in the tilting columnar structure to become visible.

speculated that a very thin oxide layer grows very quickly on the SiO columns, maybe even before the sample has reached the experimental setup. Thus, the SHG signal presented in Fig. 4.12 may be from a sample state similar to that illustrated in Fig. 4.11(c).

Interestingly, this oxidation process occurs very quickly and was found to have a pronounced effect on the SHG signal. This feature was briefly demonstrated in App. B and is also shown in Fig. 4.12. Since the square root of the decaying SHG signal is a direct measure of the SH generating Si-H dipoles disappearing, the data in Fig. 4.12 is a direct measurement of oxygen atoms arriving in the SiO film.

When observing the time-dependent SH response of the oxidising SiO films several things need to be considered. The linear optical properties also change, which will be demonstrated further below, since the SiO changes to a SiO film with a SiO_x capping layer, as sketched in Fig. 4.11(c). The refractive index and the amount of absorbed SH signal decreases due to the oxidation, and one can therefore expect an increase in generated SH response if the Si-H is not affected, which is confirmed by Eq. (2.12). The change in linear optical properties are therefore neglected when the SH response is considered, since the change in Si-H bonds will have a more pronounced effect on the SHG signal.

As oxygen atoms react with the SiO film a SiO_x oxide grows, where thickness growth at room temperature in air follows the form^{66,67,68}

$$d(t) = r_0 t_m \ln(1 + t/t_m), \quad (4.2)$$

where r_0 is the initial oxidation rate, and t_m is a characteristic time. Figure 4.12 demonstrates that the SHG signal squared can be fitted with Eq. 4.2, and where the insert shows on a logarithmic scale that the data can very well be represented

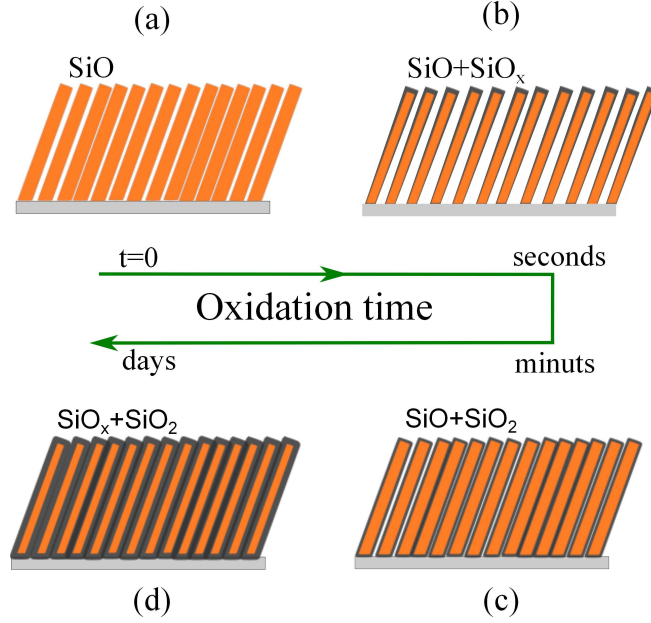


Figure 4.11: Illustrating the oxidation process of a columnar SiO thin film deposited with large α when in contact with the ambient air.

with this simple thickness model. However, this model can only be adopted to short oxidation times, since it predicts that $d \rightarrow \infty$ with $t \rightarrow \infty$, which is definitely not the case.

Another way to describe the decaying SHG signal is to use Fick's diffusion equation to describe the diffusion of H_2O molecules that are reacting with the Si-H bonds. When considering the situation in Fig. 4.11(c) the H_2O needs to penetrate a porous oxide barrier before reacting with the SiO columns. Using the work by Sah *et al.*⁶⁹ for this type of oxidation process the concentration $C(z, t)$ of the diffusing H_2O molecules as a function of time and location in the SiO film, when considering a two layered slap model, is given by

$$C(z, t) = m(1 - \xi)C_0 \sum_{n=0}^{\infty} \xi^n \text{erfc} \left[\frac{(2n+1)z_0 + rz}{2\sqrt{D_1 t}} \right] \quad (4.3)$$

where C_0 is the concentration of H_2O molecules at the columnar surface, z_0 is the thickness of the film and z is the location inside the film. With $z = 0$ is at the SiO_x/SiO interface. ξ is related to the structural properties⁶⁹ of the film, and in this case ξ is smaller than 0.5⁵⁸. $r = \sqrt{D_1 D_2}$ where D_1 and D_2 are the diffusion coefficients in the oxide layer and SiO film, respectively. Finally, m is dependent

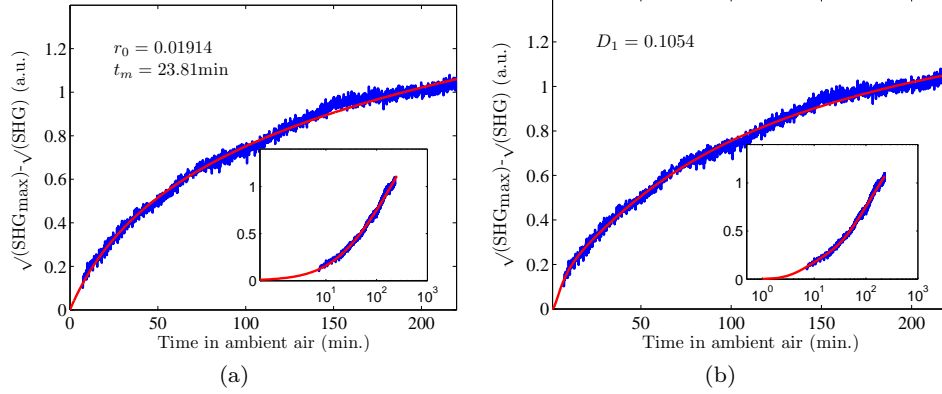


Figure 4.12: The time-dependent second-harmonic generated signal measured 5 minutes after first contact with the ambient air atmosphere at room temperature. As H_2O molecules attack the Si-H bonds the SHG decays. Therefore, the square root of the SHG signal must be directly connected to the amount of oxygen atoms reacting with the Si-H bond. The data is fitted with Eq. 4.2 in (a) and to Eq. 4.4 in (b).

on ξ and r by $\xi = (m - r)/(m + r)$.

In order to perform a fitting routine to the data, it is assumed that $z = 0$, and by using a simpler form

$$C(0, t) = A \operatorname{erfc} \left[\frac{B}{2\sqrt{D_1 t}} \right] + E \operatorname{erfc} \left[\frac{G}{2\sqrt{D_1 t}} \right], \quad (4.4)$$

the data in Fig. 4.12(b) can nicely be fitted. This equation has a more realistic form, as $t \rightarrow \infty$ the concentration of oxygen atoms arriving levels out at $C \rightarrow A + E$, since the created oxide protects the remaining Si-H bonds, as illustrated in Fig. 4.11(d). Therefore, studying the dynamics of the decaying second-harmonic signal can reveal the interaction properties between the Si-H bonds and H_2O molecules. Finally, this oxidation process also confirms that the origin of the SHG response can be assigned to ordered Si-H bonds as discussed in App. A.

Using the integrating sphere setup to study the time-dependent transmittance of $\lambda = 350\text{nm}$ from the $\alpha = 60^\circ$ and $\alpha = 45^\circ$ samples confirms the colour change identified by the naked eye. Figure 4.13 demonstrates the change in transmittance $T(t)$ subtracted $T(t = 0s)$ to gain a good reference point. The $\alpha = 60^\circ$ becomes more transparent with time compared to $\alpha = 45^\circ$, which must be related to the porosity. The inserts in Fig. 4.13 show that the oxidation levels out after > 10 days for the $\alpha = 60^\circ$, where the x -axis is on a logarithmic scale. The same must be the case for the $\alpha = 45^\circ$ sample and the remaining α thin films.

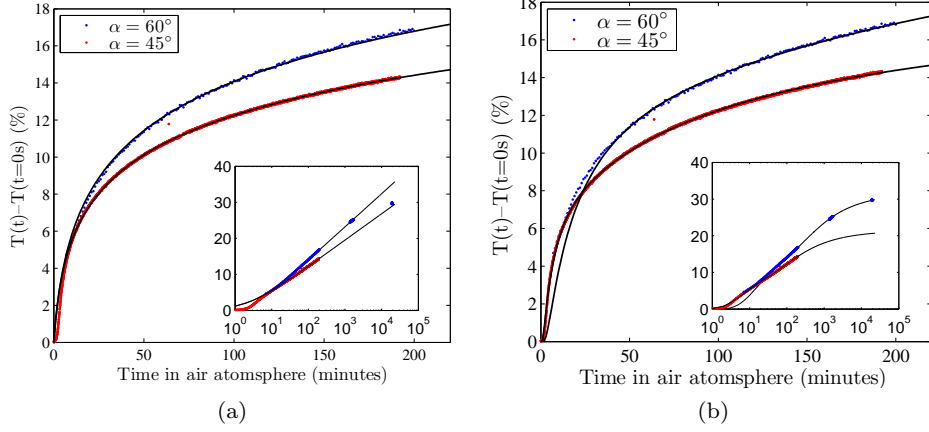


Figure 4.13: The time-dependent transmittance measured at $\lambda = 350\text{nm}$ starting few minutes after first contact with the ambient air atmosphere. The $\alpha = 60^\circ$ sample becomes more/faster transparent compared to the $\alpha = 45^\circ$ which is due to the difference in porosity. (a) the data is fitted with a logarithmic function se Eq. (4.2). The insert show that with prolonged storage time Eq. (4.2) no longer can represent the data. (b) shows that $T(t)$ data can be represented with at concentration function $C(x, t)$, see Eq. (4.3) derived from Fick's diffusion equation.

Interestingly, the time-dependent transmittance, in Fig. 4.13(a), can be fitted with the same simple logarithmic function as Eq. (4.2) on the form $T(t) = a \ln(1 + t/b)$, where a and b are constants. A reasonable fit is achieved, however, the insert shows that with prolonged oxidation time the transmittance levels off. Figure 4.13(b) demonstrates that Eq. (4.4) also can be used to represent the time-dependent transmittance. This is rather surprising since the transmittance from a thin film has the form

$$T(t) = [1 - R(t)] e^{-\sigma(t)d_{\text{SiO}}(t)}, \quad (4.5)$$

when neglecting multiple reflections. Here $R(t)$ is the reflection from the air-film interface, $\sigma(t)$ is the absorption coefficient and $d_{\text{SiO}}(t)$ is the thickness of the absorbing layer. In order to understand the behaviour seen in Fig. 4.13 all these parameters needs to be considered as they change during the oxidation. By solving the boundary value problem of the system air/film/substrate/air, the influence of these time-dependent parameters on the transmittance can be studied.

Figure 4.14(a) shows the effect on the transmittance at $\lambda = 350\text{nm}$ when changing the refractive index $n(t)$ from the $n_{\text{SiO}} \rightarrow n_{\text{SiO}_2}$ in a defined time interval. Only a slight influence, notice that the amplitude change is very small, on the transmittance is seen and can therefore be neglected. However, if the complex refractive

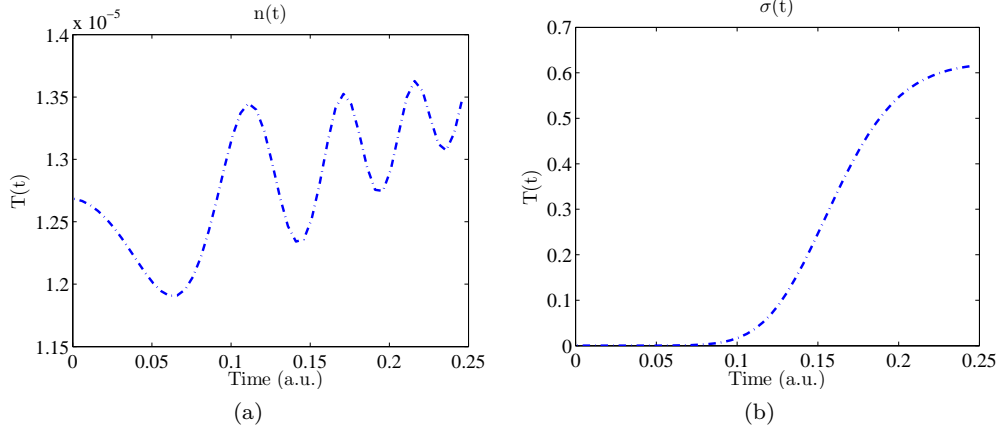


Figure 4.14: The behaviour of the transmittance as the refractive index is changed in (a) and as the complex refractive index changed in (b).

index is changed from $\kappa_{\text{SiO}} \rightarrow \kappa_{\text{SiO}_2}$ by a linear function $(\kappa_{\text{SiO}}(100 - 0.1t)/100)$ the error functional behaviour observed in Fig. 4.13 can be reproduced. However, on a short oxidation time scale it is assumed that the absorption coefficient is time-independent in the time range illustrated in Fig. 4.11(a) to Fig. 4.11(c), thus, only the thickness $d(t)$ of the absorbing SiO film is reduced, which will yield the same result as in Fig. 4.14(b). However, it should be noted that Fig. 4.13 shows that with prolonged storage, the energy band gap shifts dependent on α , hence, σ has changed.

These preliminary results demonstrates that the oxidation mechanism of porous OAD SiO films can be studied by time-dependent second-harmonic generation and time-dependent linear spectroscopy. Several clarifying experiments needs to be performed, preferably in a *in-situ* setup, in order to fully disclose the dynamics and interaction between H_2O and the SiO films. Furthermore, a full diffusion model and linear optical model is needed in order to gain a full insight into the dynamics of the time-dependent data.

4.5 Oblique angle deposited ZnO

Figure 4.15 shows SEM images of an oblique angle electron beam deposited ZnO thin film with the substrate tilted $\alpha = 30^\circ$. By comparing 4.15(a) and 4.15(b), one may think that we are dealing with two different samples, however, this is not the case. Actually, the structural properties of the ZnO thin film varied extremely over the 1 cm wide substrate. Figure 4.15(a) (side view) and Fig. 4.15(c) (top view) are images from the area of the ZnO film closest to the deposition source (position 1),

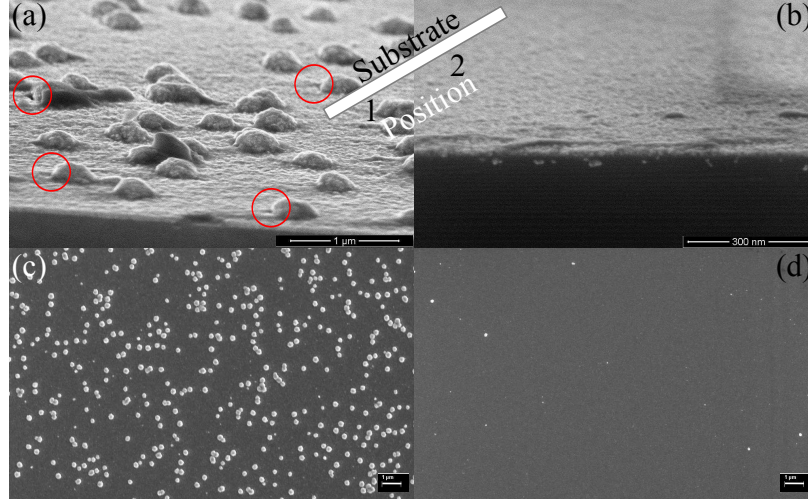


Figure 4.15: Cross sectional SEM images illustrating the structural properties of an OAD $\alpha = 30^\circ$ at position 1 see (a) and position 2 see (b). In (a) a ZnO thin film with nanoparticles is seen and in (b) these particles are lacking. The topview SEM images in (c) and (d) highlights this pronounced difference in structural properties across the sample.

whereas Fig. 4.15(b) (side view) and Fig. 4.15(d) (top view) are images about 0.5 cm further away from the source (position 2). This variation in structural properties over 0.5 cm is quite amazing when considering that the source is about 1 m from the substrate. Moreover, the sample thickness for $\alpha = 30^\circ$ at position 1 was around 200 nm and decreased down to 20 nm at position 2, which was estimated from cross sectional SEM images (not shown). It is seen in Figs. 4.15(a) and (c) that the ZnO film consists of a thin film with nanoparticles at position 1, while at position 2 only the thin film is present. Notice that the particles have "shadows" (indicated by red circles) which are due to a lack of deposited material since it is condensed on the nanoparticle. Hence, the ZnO film is indeed OAD deposited, a fact that also can be seen by a small tilt of the nanoparticles.

The deposition pressure was 10^{-4} mbar which is very high for an electron deposition process. As a result of this, a pressure gradient could have been present across the substrate during the deposition which may explain this structural variation across the sample. Nonetheless, a series from $\alpha = 0^\circ$ to $\alpha = 80^\circ$ was deposited with a stable deposition rate of $\sim 0.8 \text{ \AA/s}$, which yield the same structural variation for all samples as seen in Fig. 4.15.

In this chapter we saw that the angular dependence of SHG could be used to identify the tilt ζ of a structure deposited at oblique angles. Figure 4.16 shows

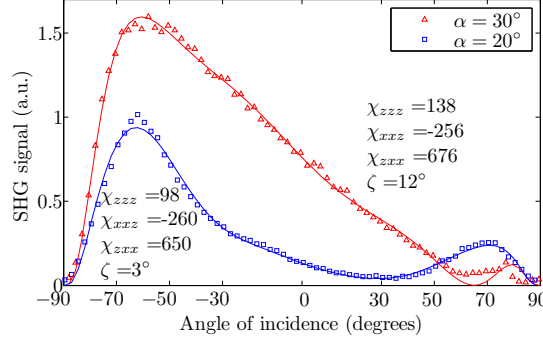


Figure 4.16: The SHG signal as a function of angle of incidence measured from OAD ZnO at $\alpha = 20^\circ$ (blue squares) and $\alpha = 30^\circ$ (red triangles). The estimated tensor elements and the growth direction ζ from the two samples can be found in the figure.

the measured SHG signal as a function of angle of incidence from two samples; one deposited at $\alpha = 30^\circ$ and one at $\alpha = 20^\circ$. The two samples were probed at position 1 (the nanoparticle area), however, due to the varying structural properties throughout the ZnO film it is very difficult to get a good idea about the structural properties that are being probed. The samples were placed and probed in the same manner as in App. B, however, in this case the probing p-polarised fundamental wavelength was 786 nm from the Ti:sapphire laser system. A significant difference in the SHG signal from the two samples is seen in Fig. 4.16 and the presented model in App. B fits both AOI data signals fairly well. In order to perform the fit, the complex refractive index is needed and was adapted from elsewhere⁷⁰. Since the thickness varied across the samples, this was also used as a fitting parameter along with the tensor elements χ_{zzz} , χ_{xxz} and χ_{zxx} and the structural tilt ζ . Unfortunately, with these five fitting parameters, the model can basically be fitted to anything. However, notice that the estimated tensor elements for the two different samples yield the same values. Here the ratio between the tensor elements are; $\chi_{zxx}/\chi_{zzz} = 4.9$ and $\chi_{zxx}/|\chi_{xxz}| = 2.6$ for the $\alpha = 30^\circ$ film and $\chi_{zxx}/\chi_{zzz} = 6.6$ and $\chi_{zxx}/|\chi_{xxz}| = 2.5$ for $\alpha = 20^\circ$ which are amazingly closely related. This convergence between the two fits indicate that the fitted values ζ found in Fig. 4.16 are true and moreover, they are in the range of what is expected. It is rather surprising that the tensor element χ_{zzz} is smaller than χ_{zxx} and χ_{xxz} contrary to the values reported elsewhere⁷¹. However, the second-order nonlinear optical susceptibility elements have shown to be strongly dependent on the structural properties of the ZnO thin film.^{71,33} As seen in Fig. 4.15 the film consist of two different structures; a ZnO thin film part and a ZnO nanoparticle part, where each part may have a different second-order susceptibility tensor. Thus, more investigations are needed to fully understand the

SHG response from these rather complex ZnO structures.

4.6 Summary and Outlook

Using electron beam deposition to produce SiO thin films leads to non-centrosymmetric films, which have a strong second-harmonic response comparable to crystalline quartz, see App. A, where the response is suggested to arise from oriented dipoles. Through oblique angle deposition it was demonstrated, see App. B, that the second-harmonic response can be tuned through the deposition angle α . Moreover, a presented model showed the possibility for extraction of the growth direction of the tilted columnar structure. Furthermore, this technique was demonstrated to work on OAD ZnO, however, further studies are needed to draw any conclusion on OAD ZnO. Unfortunately, the porous columnar structure of OAD SiO tend to oxidise when in contact with ambient air. It was demonstrated that the oxidation mechanism can be observed with linear optics as well with nonlinear optics.

Enhancing the effective nonlinear coefficient of SiO can be approached by several means. Introducing hydrogen during the deposition process may affect the SH response since this SH response is speculated to arise from oriented Si–H and O–H bonds. Investigating the SHG as a function of stoichiometry (SiO_x) may be a more straight forward study; one must simply prepare a mixture of SiO and SiO_2 powder in the deposition crucible. Additionally, Si_yO or Si_yO_x films may enable the presences of a higher density of Si–H bonds throughout the film resulting in an enhanced SH response. Moreover, introducing Ge to the deposition process may enhance the SH response.⁷²

Electron beam deposition of SiO enables fabrication of nonlinear optical devices that are compatible with Si processing technology, as demonstrated in Fig. 4.4. This enables extremely well defined nonlinear 2D structures which, for instance, can be used as waveguides for surface plasmons⁷³, and to excite second-harmonic surface plasmons.⁷⁴ Silicon monoxide can therefore be a very interesting material for studies in second-harmonic plasmon polaritons waveguides.⁷⁵ Sensors may be developed by using ring resonators⁷⁶ to enhance the second-harmonic signal and utilizing that the enhanced SH signal amplitude is very sensitive to changes in the refractive index of a ring resonator, which may occur due to adsorbed species. Actually, it has been demonstrated that adsorption of H_2O on porous SiO can be measured by a capacitance change⁷⁷, thereby, making porous SiO ring resonators a interesting approach to study interaction with H_2O .

Altogether, this chapter has shown, that electron deposited silicon monoxide has future perspectives in silicon based nonlinear optical devices.

Interaction between ZnO and O₂ probed by TD-SHG

5.1 Introduction

Three years after the first experimental discovery of second-harmonic generation in a non-centrosymmetric crystal in 1961 by Franken *et al.*,⁴ Miller reported for the first time the experimentally estimated second-order susceptibility tensor elements of crystalline zinc monoxide (ZnO).³⁰ The closed packed hexagonal structure of crystalline ZnO and point group 6 mm symmetry is the reason for three second-order non-vanishing tensor elements, namely $\chi_{xxz} = \chi_{xzx} = \chi_{yyz} = \chi_{zyz}$, $\chi_{zxx} = \chi_{zzy}$, and χ_{zzz} which leads to a bulk second-harmonic response.⁶ Miller estimated these elements to be relatively large and later on in the 1990's, it was realized that these tensor elements could be enhanced by controlling the nano-structure of ZnO thin films.³³ Through deposition conditions and techniques the synthesis of ZnO may yield different types of nanostructures; nanocrystalline thin films⁷⁸, nanowires^{79,80,81}, nanoparticles⁸² and nanoflakes⁸³.

Apart from the inherent bulk second-harmonic response from ZnO a common interest into possible application areas has increased over the past decades.⁸⁴ Poly- and nanocrystalline ZnO has a direct band gap of 3.2-3.4 eV at room temperature and its n-type conducting properties are ideal for solar cell applications,^{85,86,87,88}

and furthermore it is an efficient light emitting diode in the near UV region of the spectrum.^{89,90} The sensor properties of ZnO to ambient air have already been investigated in the early 19th century.⁹¹ When O₂ is adsorbed on surface defect sites a measurable change in resistivity occurs. Nowadays, different types of nano-structured ZnO have been used to enhance this interaction and have been shown to work well as UV detectors and O₂ detectors.^{36,92,93,94} Besides ZnO, TiO₂ surface defect sites also interact with O₂ and H₂O, and actually this interaction between TiO₂ and the ambient air has been studied with SHG.^{95,96,96} However, studies of the interaction between ambient air and ZnO with SHG have not yet been reported in the literature before the paper found in App. C.

In this chapter the interaction between ambient air and ZnO thin films is investigated with time-dependent second-harmonic generation (TD-SHG). The presented material should be regarded as supplementary to the article found in App. C. First off all the structural properties of atomic layer deposited (ALD) ZnO thin films are discussed. We briefly touch the n-type properties and the spectral second-harmonic response from several different ZnO thin films. Finally, the TD-SHG results are presented for newly fabricated samples and samples stored for a given time-period in ambient air. The latter are included to investigate the ageing effect of ZnO when in contact with the ambient air and should be considered as preliminary results.

5.2 Structural properties

Several ZnO thin films were deposited by atomic layer deposition (ALD), mainly on silicon (001) substrates and a few on Corning 7059 glass substrates. A series with varying thickness was deposited on silicon with a substrate temperature of 200°C for SHG spectral analysis. Moreover, the interaction between oxygen molecules and surface defect sites of ZnO was investigated on a 20 nm thick sample prepared on silicon at 180°C. In Fig. 5.1(a) a high resolution cross sectional transmission electron microscopy (TEM) image illustrates the nanocrystalline structure of a sample prepared at 250°C on a glass substrate.

For Figs. 5.1a and 5.1b it is clear that the nanocrystals grow perpendicular to the substrate surface. Different crystal orientations are present with was confirmed by X-ray diffraction.⁹⁷ In addition, it was also found that the crystal structure depends on film thickness, which is supported by the optical properties presented in the following section. Figure 5.1(c) and 5.1(d) show the surface morphology measured using AFM of samples prepared at 200°C and 180°C, respectively. Decreasing the substrate temperature normally results in smaller crystal grains leading to additional surface defects sites and grain boundaries. These sites interact with oxygen, thus, the number of defect sites play an important role. This is important in nanowires, where a high surface to volume ratio is achieved.

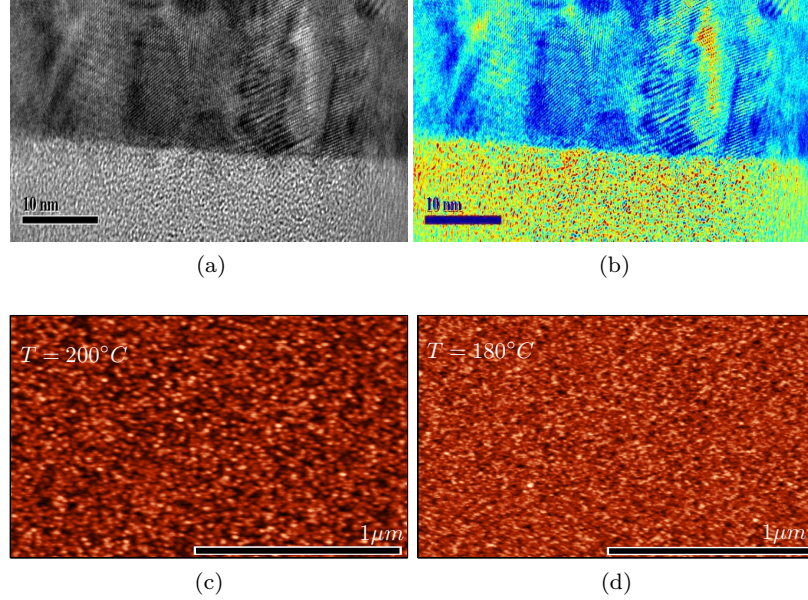


Figure 5.1: A cross sectional TEM image of an ALD ZnO thin film on SiO₂ prepared at 250°C, in grayscale (a) and in colour scale (b). Notice the different lattice planes indicating a nanocrystalline structure. AFM images of thin films prepared at 200°C and 180°C found in (c) and (d), respectively. Larger grains are synthesised when increasing the substrate temperature.

5.3 Second-harmonic generation from ALD ZnO

As discussed in Chap. 2 three independent non-vanishing second-order susceptibility tensor elements χ_{xxz} , χ_{zxx} and χ_{zzz} leads to a bulk second-harmonic response from ZnO. It was briefly demonstrated in Sec. 4.5 that the angular second-harmonic response from oblique angle electron beam deposited ZnO could only be fitted if these three tensor elements were considered. In Fig. 5.2(a) the measured reflected second-harmonic spectral response from 11 nm to 86 nm thick ZnO thin films deposited onto silicon is presented. Moreover, in Fig. 5.2(a), the spectral response from a 38 nm thick film deposited onto silicon without the native oxide is presented. The oxide was removed with a HF dip shortly before the deposition. Apart from the silicon substrate samples with varying thickness in Fig. 5.2(a), a single sample of 86 nm deposited on corning 7054 glass is included. The direct band gap of 3.4 eV of bulk ZnO is marked with a vertical blue line.⁶ Looking at the 11 nm to 86 nm series it is evident that the SHG peak position shifts around depending on film thickness. In Fig. 5.2(b), the absorption coefficient κ shows that the energy

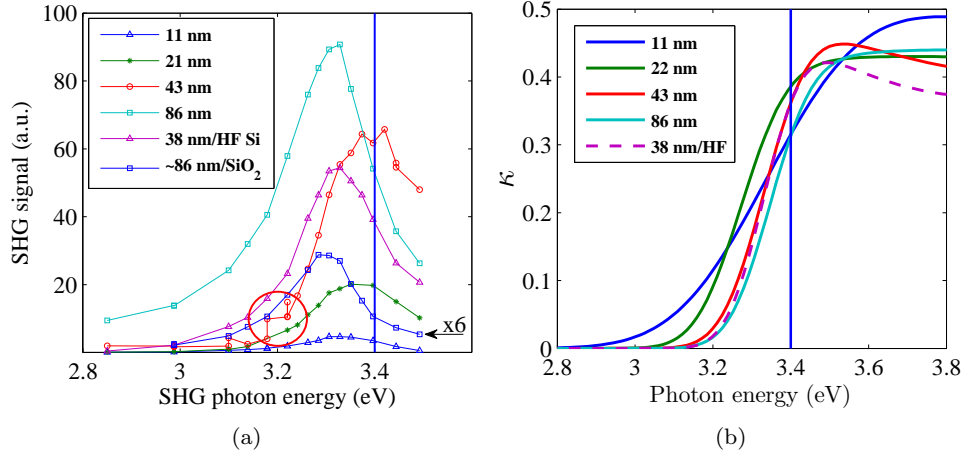


Figure 5.2: (a) SHG spectral response from: 11 nm to 86 nm thick ZnO thin films deposited on silicon, 38 nm sample deposited on silicon without the native silicon oxide, and finally a 86 nm sample deposited on Corning 7059 glass. The peak position shifts around and is speculated to be related to a difference in crystal structure. (b) The estimated (by SE) imaginary part of the complex refractive index as a function of photon energy.

band shifts towards 3.4 eV with increased film thickness. Hence, the peak positions of the SHG response corresponds very well to the data in Fig. 5.2(b). However, it should be noted that the correct SHG peak position of the 86 nm sample in Fig. 5.2(a) is not seen due to strong absorption of the SHG signal in the sample, hence, the "true" peak position may be closer to the bulk resonance at 3.4 eV as seen for the 43 nm thick sample.

Notice that the SHG spectral peak position of the 38 nm HF sample and 43 nm sample differ, which is rather surprising since they accompanied each other during the deposited, and the resulting absorption coefficient are almost identical. The thickness difference is related to the ALD of ZnO on bare silicon is normally delayed by few deposition cycles. It is expected that there is a difference in crystallinity between these two samples, since the bare crystalline silicon substrate triggers crystalline growth compared to the native oxide, which may explain this difference.

Notice the amplitude variations, indicated by the red circle, measured at the same pump photon energy. It was realised that this drop in SHG amplitude is related to oxygen molecules adsorbed on the surface.

5.4 Time-dependent second harmonic generation

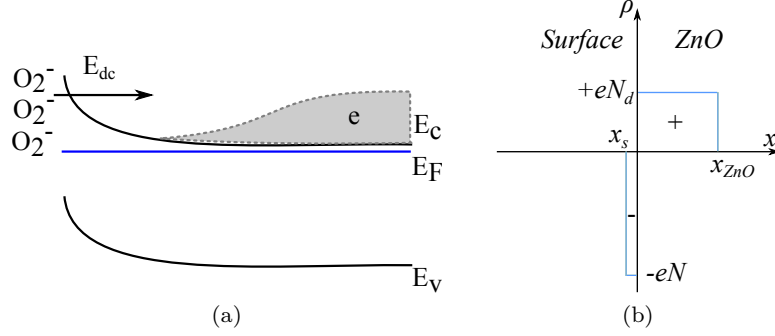


Figure 5.3: (a) Illustrates the upward band bending due to adsorbed O_2 molecules at surface defect sites. This oxygen induced E-field near the surface will deplete the electrons (grey area) towards the ZnO/native silicon oxide interface and a measurable change in resistivity is possible as oxygen molecules are adsorbed. (b) Illustrates the separation of space charge densities due to the oxygen induced e-field.

During the SHG spectral measurements it was realized that a time-dependency of the SH signal was present. This time-dependency was related to oxygen molecules desorbing from surface defect sites due to a two-photon process, see App. C. The largest time dependent response was measured when using a pump energy of 1.675 eV. Oxygen molecules adsorbed on surface defect sites capture a free electron and O_2^- ions are created. As illustrated in Fig. 5.3(a), oxygen ions located at the surface will bend the energy bands upward, which in turn will deplete the free electrons toward the ZnO/native oxide interface. A separation of space charge densities occurs as illustrated in Fig. 5.3(b). The associated depletion region is created and a built-in oxygen induced electric field E_{dc} is observed. Here E_{dc} is determined from Poisson's equation⁹⁸

$$\frac{d^2\phi(x)}{dx^2} = \frac{-\rho(x)}{\epsilon} = -\frac{dE_{dc}(x)}{dx}, \quad (5.1)$$

where $\phi(x)$ is the electric potential, $\rho(x)$ is the volume charge density, and ϵ is the permittivity of ZnO. Using the relationship in Fig. 5.3(b) to define the boundary conditions, the electric field at the surface and in the film region is found as

$$E_{dc} = \int \frac{\rho(x)}{\epsilon} dx = \begin{cases} \frac{-eN}{\epsilon}(x + x_s) & -x_s \leq x \leq 0 \\ \frac{-eN_d}{\epsilon}(x_{ZnO} - x) & 0 \leq x \leq x_{ZnO} \end{cases};$$

where N_d is the doping density. As indicated in Fig. 5.3(b) the total charge $Q = eN$ located at the surface must be balanced by the charge in the depletion region

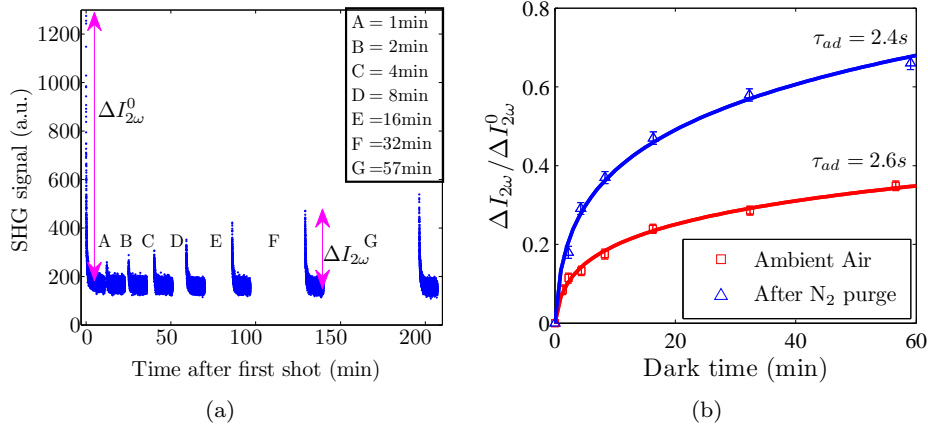


Figure 5.4: (a) Effect of blocking and unblocking the probing laser on the TD-SHG response from the sample prepared at 180°C. As the laser is unblocked the SHG signal decays and when blocked in the time intervals (dark times) A, B, ... and G (see legend), the amplitude of the SHG signal recovers and is dependent on dark time. (b) Recovered SHG signal amplitude ($\Delta I_{2\omega}$) normalized to the first measured amplitude change ($\Delta I_{2\omega}^0$) as a function of dark time. Here the solid lines are the best fit with Eq. (5.5)

according to

$$Q = N_d x_{ZnO} \approx N_d w, \quad (5.2)$$

where w is the width of the space charge region and it is assumed that $x_S \ll x_{ZnO}$. In a first approximation the total charge Q is related to the number of adsorbed oxygen molecules N . The number N adsorbed at a time t is found from³⁵

$$N(t) = A \left[\ln \left(t + \frac{1}{\tau_{ad}} \right) + \ln(\tau_{ad}) \right]. \quad (5.3)$$

Here, A is related to the number of passivated surface defect sites and τ_{ad} is a characteristic time constant for adsorption on these sites. With an increase in the number of oxygen molecules a larger oxygen induced electric field E_{dc} is created.

$$N(t) = Q(t)/e \propto E_{dc}(t). \quad (5.4)$$

As presented in Chapter 2 the SH response depends on the build-in electric field squared. Thus, by combining with Eq. (5.3) the TD-SH response of the oxygen-induced electric field as the form,

$$I(t) \propto (E_{dc}(t))^2 \propto A^2 \left[\ln \left(t + \frac{1}{\tau_{ad}} \right) + \ln(\tau_{ad}) \right]^2. \quad (5.5)$$

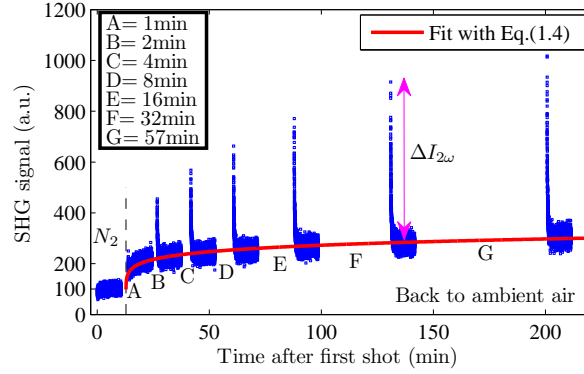


Figure 5.5: The time-dependent second-harmonic generated signals dependency on dark time when the sample is reintroduced to the ambient air after having being exposed to a nitrogen atmosphere. Notice an overall increase in SHG response, which is speculated to be related to formation of OH^- . The solid line is the best fit using Eq. (5.5) thereby indicating an adsorption process.

Figure 5.4(a) demonstrates the influence of blocking and unblocking the probing laser on the TD-SHG signal from a 20 nm thick ZnO film deposited on silicon. By blocking the laser at different times A, B, ... and G, so called dark times, a recovery in the SHG signal amplitude is seen to depend on dark time. With extended dark periods additional oxygen is adsorbed and a corresponding larger SHG signal amplitude is measured. This is due to a larger upward bending of the energy bands. Performing the same experiment in a nitrogen atmosphere the recovery of the SHG signal was absent. However, by reintroducing the sample to ambient air, see Fig. 5.5, the SHG signal recovered as discussed in App. C.

Figure 5.4(b) shows the change in SHG signal $\Delta I_{2\omega}$ normalized to the first measured amplitude change $\Delta I_{2\omega}^0$ as a function of dark time. By fitting the data with Eq. (5.5), the time constants were found to $\tau_{ad} = 2.6 \pm 0.7\text{s}$ and $\tau_{ad} = 2.1 \pm 0.7\text{s}$. As discussed in App. C the estimated τ_{ad} from the TD-SHG measurement are comparable to τ_{ad} estimated by other techniques.

An overall increase in SHG base level is also seen in Fig. 5.5 and has been fitted with Eq. (5.5), the solid red curve, thereby indicating an adsorption process different from the O_2 adsorption. As discussed in App. C it may be related to formation of OH^- due to the probing laser. According to Meyer *et al.*⁹⁹, and Dulub *et al.*¹⁰⁰ isolated water molecules are physisorbed on ZnO surfaces. When a second H_2O molecule is adsorbed on the surface at a neighbouring site, a hydrogen bond is established that triggers a dissociation of the H_2O molecules. This allows for capturing an electron-hole pair¹⁰¹ generated by the probing laser, which may contribute to an EFISH. Notice in Fig. 5.4(a) that the base level in SHG signal

is around 200 a.u., whereas in N₂ atmosphere the base level is reduced to around 100 a.u., see Fig. 5.5. This decrease in signal amplitude may be related to H₂O being removed from the surface due to the nitrogen purge, and as the sample is reintroduced to the ambient air, the H₂O EFISH returns. It is unclear, which mechanism is dominating, but the fact that it is possible to fit the SHG base level tendency with Eq. (5.5) indicates that we must be dealing with an adsorption process. This feature is discussed further below.

5.5 Ageing of ZnO

With prolonged storage time the deep-level (green) photoluminescence (PL) from ZnO has been demonstrated in the literature to decrease.^{102,103} This green deep-level PL is still up for debate whether or not it is related to oxygen vacancies.¹⁰⁴ Liu *et al.*¹⁰⁵ recently demonstrated that an increased amounts of oxygen vacancies leads to a corresponding increase in green PL. Therefore, this reduced green PL during storage time may be related to oxygen vacancies being slowly passivated by oxygen molecules.

Ageing effects were realized during the very first measurements performed on ALD ZnO thin films. The time-dependent second-harmonic response from the ZnO films changed from day to day when stored in ambient air and in the dark at room temperature. Results presented in App. C are measurements performed 24 hours after the deposition process. Here the time-dependent behaviour of the SHG response measured directly after the deposition is presented and the TD-SHG signal as a function of storage time.

The TD-SHG signal measured directly after the deposition process (~10 min) is presented in Fig. 5.6. A clear difference is observed when comparing the measurements in Figs. 5.4 and 5.5 and in App. C with Fig. 5.6. Basically the measurements are the same except with a 24 hour delay after fabrication in the results from Figs. 5.4 and 5.5 and in App. C.

When blocking the probing laser in front of this young sample the response time to oxygen is very fast, especially after the first measured curve in Fig. 5.6. Moreover, notice that during the first measurement the base value is slightly increasing and then starts to decrease. By blocking the laser this decrease, indicated by the arrow, seems to continue independent of the laser exposure and levels out.

Electron Spin Resonance (ESR) experiments have shown the presence of O₂⁻ and O⁻ on ZnO at room temperature.^{106,107} Furthermore, theoretical calculations have confirmed that it is possible for a defective ZnO surface to adsorb O₂⁻ and O⁻ ions.^{108,109} After the deposition process the sample was exposed to ambient air at 180°C. At this temperature desorption of O₂ occurs, however, higher temperatures are needed to desorb O⁻.¹⁰⁶ It is suggested that when the ZnO film is introduced to the ambient air the surface could only be O⁻-passivated. Lundsford and Jayne¹¹⁰

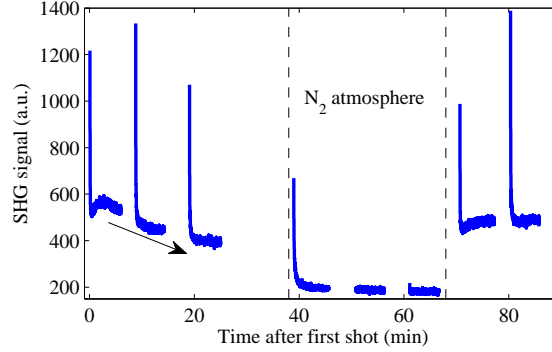


Figure 5.6: The time-dependent second-harmonic signal measured directly after the deposition process from the same sample as investigated in Figs. 5.4 and 5.5. The measured SHG signal behaves as expected in N_2 atmosphere and when reintroduced to the ambient air. However, immediately after the deposition the base SHG signal level is decreasing (indicated by the arrow) and seems to be independent of laser exposure. Finally, notice that the response to O_2 molecules are extremely fast compared to Figs. 5.4 and 5.5.

demonstrated by ESR that O^- is converted to O_2^- when the surface is exposed to oxygen molecules until a balance between O^- and O_2^- molecules is reached. It is unclear, if the decrease in SHG base level is dominated purely by O^- conversion to O_2^- , or if substitution of O^- with H_2O also occurs. Nonetheless, it is clear that the surface of the ZnO film changes directly after the deposition when in contact with the ambient air. The TD-SHG base level behaviour seen the first 30 min in Fig. 5.6 could not be reproduced with the same sample. This indicates that a newly made ZnO surface changes irreversibly. This could be related to an excess amount of O^- ions on the surface that is reduced when in contact with the ambient air.

Interestingly, when the sample was introduced to a nitrogen atmosphere, a large reduction in base level was seen and when reintroduced to the ambient air a corresponding recovery in signal base level was seen. This feature was also observed in Fig. 5.5, however, not as pronounced as observed in Fig. 5.6. This signal recovery appears to be laser independent and may be related to an intrinsic H_2O EFISH formation.

Clearly, the response to oxygen in Fig. 5.6 is fast compared to the results presented in App. C. In order to address this ageing property, two samples were prepared simultaneously on two different substrates, one with (NO HF) and one without (HF) the native silicon oxide. Both were prepared with a substrate temperature of 200°C , see App. C for similar deposition conditions. It is assumed that the HF sample is more crystalline due to the direct contact with the crystalline silicon substrate. The samples were stored in ambient air, in the dark and at room

temperature between measurements.

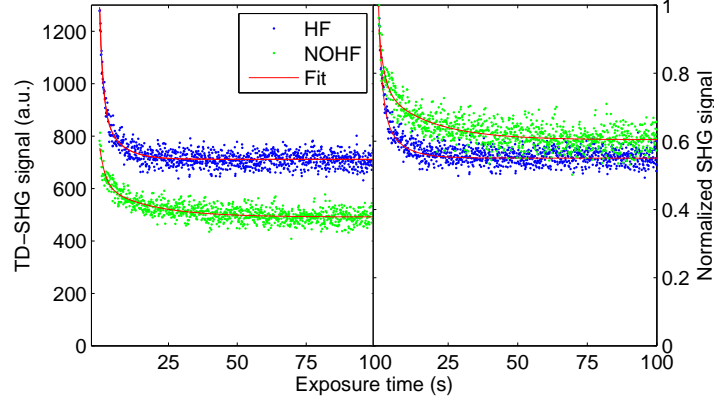


Figure 5.7: TD-SHG signal measured after 70 hours of storage in the dark and in the ambient air. The right hand side is the normalized data from the left hand side, the red curve is the best fit with Eq. (5.7) yielding τ_{de} plotted in Fig. 5.8a. The laser pump power was 36 mW.

Figure 5.7 shows the TD-SHG signal measured 70 hours after ambient air exposure. The HF sample has an overall larger SHG response, which must be related to a higher order of crystallinity compared to the NO HF sample. By normalizing the data, right hand side of Fig. 5.7, it is seen that oxygen molecules are desorbed faster from the HF sample, where for the NO HF sample, longer laser exposure is needed, before the SHG signal levels out. This may be due to an easier diffusion into the ZnO film for the NO HF sample, where the oxygen will migrate to defect sites at grain boundaries.^{102,103} Hence, longer laser exposure is needed to photodesorb oxygen from the grain boundaries compared to the surface. Additionally, the amplitude change $\Delta I_{2\omega}$ is smaller of the NO HF sample indicating a smaller oxygen induced E_{dc} or a smaller value of $\chi^{(3)}$. As discussed in App. C the signal amplitude of the oxygen induced EFISH is dependent on $\chi^{(3)}$

$$P_i^{(2)}(2\omega) = \epsilon_0 \sum_{jkl} \chi_{ijkl}^{(3)} E_j(\omega) E_k(\omega) E_l^{dc}. \quad (5.6)$$

On the other hand $\chi^{(3)}$ is related to the structural properties of the ZnO films.¹¹¹ Moreover, since $\Delta I_{2\omega}$ must be related to the amount of free surface defect sites, it is expected that the NO HF sample would have a larger oxygen induced EFISH due to a larger amount of defect sites compared to the HF sample. However, oxygen diffusion into the NO HF sample may be easier, thus resulting in more oxygen present at grain boundaries throughout the film compared to HF. This may yield a

more uniform upward bending of the energy bands and thereby the oxygen induced EFISH becomes smaller, this will be discussed further below. It is unclear if the difference of $\Delta I_{2\omega}$ is due to a different $\chi^{(3)}$ or to a difference in diffusivity of oxygen or even a combination of both. Nonetheless, it is quite apparent that the TD-SHG is dependent on the structural properties of the ZnO thin films, as indicated in App. C.

As demonstrated in App. C, the decay in SHG signal follows an exponential tendency, and a characteristic time constant τ_{de} could be estimated for the desorption rate of oxygen. It was realized that after the samples were stored for longer than ~ 3 days, the measured TD-SHG decay curves could only be properly fitted when introducing an extra decay term,

$$I_{2\omega} \propto \left[a_s \exp(-t/\tau_{de}^s) + a_f \exp(-t/\tau_{de}^f) \right]^2. \quad (5.7)$$

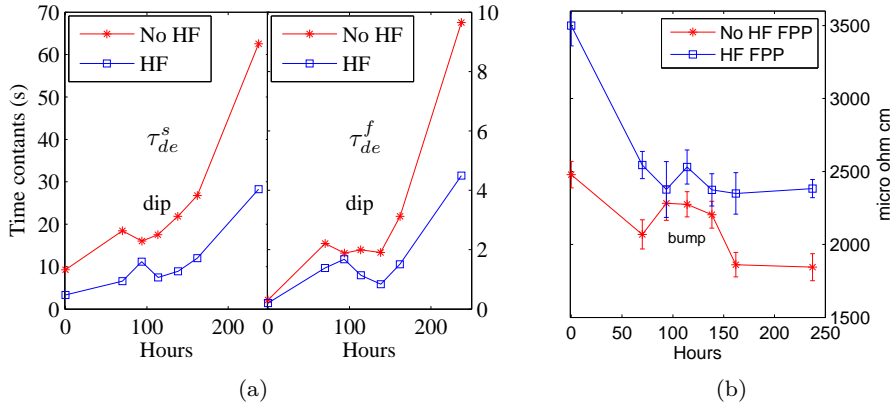


Figure 5.8: The optical and electric properties as a function of storage time for a sample with and without the native oxide. (a) Since τ_{de} increases with storage time longer laser exposure is needed to photodesorb O_2 . This may be related to O_2 diffusion into the ZnO thin film. (b) A corresponding decrease in sheet resistivity is seen and seems to level out with storage time unlike τ_{de} .

Figure 5.8(a) shows the estimated τ_{de}^s (slow τ_{de}) and τ_{de}^f (fast τ_{de}) as a function of storage time in the ambient air. Notice, that the τ_{de}^f appears after three days of storage, nonetheless, the slow and fast τ_{de} have a similar tendency, which seems to be independent of sample type. The two time constants τ_{de}^s and τ_{de}^f may be related to O_2^- desorbing from two different defect sites or even different desorption species O_2^{2-} .^{36,110} Moreover, with prolonged ambient exposure oxygen starts to diffuse into the films passivating defect sites at grain boundaries. This leads to the need for

longer laser exposure before the SHG signal levels off at the bulk SHG response as observed in Figure 5.8(a).

Figure 5.8(b) demonstrates the behaviour of the sheet resistivity measured by a four point probe (FPP) setup. Notice that the sheet resistivity is inverse proportional to the τ_{de} in Fig. 5.8 until 150 hours, where it seems to level out. According to Fig. 5.8, larger τ_{de} leads to a lower sheet resistivity, which is quite surprising, since it is expected to increase when in contact with ambient air.^{104,36,112} However, these predictions do not address the influence of oxygen diffusion into the ZnO films on a prolonged time scale. For a sol-gel prepared ZnO film, the same behaviour seen in Fig. 5.8(b) was demonstrated by Bandyopadhyay *et al.*¹¹³. The resistivity was found to decrease exponentially on a prolonged storage time.

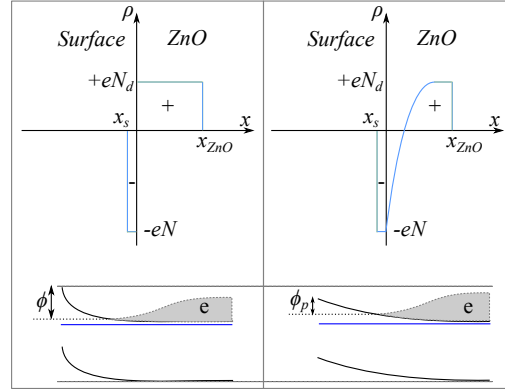


Figure 5.9: The distribution of space charge densities with O₂⁻ located only on the surface (left hand side) and when O₂⁻ is also located at grain boundaries (right hand side). The corresponding upward bending of the energy band is illustrated below. With O₂ located at grain boundaries the upward bending is smeared and the free electrons can easier overcome the pontial barrier. This model may explain the behaviour seen in Fig. 5.8.

Fig. 5.9 illustrates the effect on the space charge densities and the corresponding energy band bending after the deposition (left hand side) after the prolonged storage time (right hand side) due to the interaction between ZnO and O₂ molecules. The grey areas indicated with "e" illustrate the distribution of the free electrons in both cases, ϕ is the work function after the deposition, and ϕ_p after prolonged storage time. With a bare ZnO surface, oxygen molecules can quickly adsorb and form O₂⁻ ions. However, with time an accumulation of O₂⁻ ions located on the surface occurs, and the number of adsorbed oxygen molecules slows down according to Eq. (5.3). A corresponding logarithmic increase in sheet resistivity is expected since the oxygen induced E-field at the surface will deplete the free electron towards the ZnO/substrate interface. The free electrons will have a large work function ϕ

to overcome as illustrated in Fig. 5.9. With prolonged storage time the oxygen molecules will diffuse into the ZnO film creating O_2^- ions at grain boundaries. This will reduce the upward bending as illustrated in right hand side of Fig. 5.9 with the corresponding space charge density. The effect will reduce the sheet resistivity as the work function ϕ_p is smaller, hence, the free electrons in the conducting band now have a lower potential barrier to overcome. This model may explain the behaviour seen in Fig. 5.8b and Bandyopadhyay *et al.*¹¹³.

Interestingly, a bump and dip are seen in Figs. 5.8(a) and Fig. 5.8(b), respectively. This effect is more pronounced for the NO HF sample. The dip in τ_{de} is an artefact of less oxygen present to photodesorb and as discussed above this should lead to an increase in resistivity, if less O_2^- ions are located at grain boundaries. The three days with the dip/bump may be related to the local weather, which was clear skies and sunshine in the three days interval contra the other days. In order to perform the FPP measurement the samples were removed from the climate controlled laser laboratory to the FPP laboratory with fluorescent lamps and large windows allowing sunshine (and heat) in. Any UV light will remove the oxygen molecules, thus, the sample may have been affected by the unsuitable FPP laboratory conditions. Nonetheless, it is apparent that τ is strongly related to the sheet resistivity.

5.6 Summary and Outlook

It was found that the spectral response from thin ZnO films depends on film thickness and thereby the structural properties. It has been demonstrated that the interaction between ZnO and ambient air gases can be probed by time-dependent second-harmonic generation, where the SHG signal decays due to the photodesorption process. It was found that the adsorption dynamics of oxygen strongly depends on the surface condition of ZnO. The adsorption rates estimated from dark time TD-SHG measurements were found to be comparable to other techniques. Additionally, it was demonstrated that ageing effects of ZnO can be probed by TD-SHG. It was discussed that the change in TD-SHG response as a function of sample storage may be related to oxygen diffusing into the ZnO film, where they adsorb at grain boundaries. It is a rather complex adsorption system, where H_2O influences the O_2 interaction with ZnO. Therefore, in-situ TD-SHG characterisation of a ZnO thin film prepared in ALD deposition chamber is a possibility. Additional disclosing the TD-SHG dependency on surface morphology and structural properties may lead to further insight into the interaction. As demonstrated in chapter 4 oblique angle deposition of ZnO can lead to exotic nanostructures, which may be interesting to study with TD-SHG. Especially to disclose the ageing properties of ZnO upon prolonged exposure to ambient air as a function of structural properties, which may help give insight into the tendencies seen in Fig. 5.8. Moreover, *in-situ*

measurements on ZnO may give a more clear picture of the O₂-H₂O-ZnO system.

The overall conclusion is that the TD-SHG technique is a powerful tool to study the O₂ interaction with ZnO and may easily be extended to different types of gases (H₂, CO₂, CO, . . .). Moreover, the preliminary ageing results indicate that the oxidation process of surface and grain boundaries can be probed with TD-SHG.

Summary

This Ph.D. thesis studies the interaction between light and nonlinear thin films. When a nonlinear film is probed by intense laser light with photons of energy $\hbar\omega$, it will generate second-harmonic photons with twice the energy $2\hbar\omega$. Studying these second-harmonic generated photons as a function of different parameters can reveal information about the structural properties of the probed medium on a macroscopic scale as well as on a microscopic scale. Nonlinear optical devices based on second-harmonic generation have become an active research field with the focus on development of new nonlinear materials that have a strong nonlinear response.

With regards to this, it is demonstrated that a standard electron beam deposition technique of silicon monoxide results in a nonlinear thin film that has a strong second-harmonic response. The second-harmonic response arises due to specific deposition conditions, and several studies point in the direction of ordered dipoles as the source of the nonlinear response. It is also demonstrated that using a standard lithography process well defined nonlinear 2D SiO nanostructures can easily be constructed.

An oblique angle deposition technique is used to fabricate several SiO thin films, with a tilted columnar structure that depends on the oblique deposition angle. It is demonstrated that the second-order nonlinear response strongly depends on the angle of the tilted SiO structure, and by analysing the second-harmonic response, the angle of the tilted columns can be identified. As a consequence this simple oblique angle electron beam deposition of SiO enables one to tune the nonlinear response as one desires.

Unfortunately, this tilted porous structure tends to oxidise when in contact with ambient air resulting in a reduction of the second-harmonic signal. It is discussed that the reduction in signal can actually reveal the dynamics of the oxidation process and that the time-dependent second-harmonic response is a direct measure of oxygen atoms arriving in the SiO film. Furthermore, it is demonstrated that the oxidation process can also be studied with linear optical spectroscopy as an indirect probe to the arriving oxygen atoms.

The interaction mechanism between ambient air and thin ZnO films is also studied by time-dependent second-harmonic generation. Here it is demonstrated that O₂ adsorbed at the surface induces an electric field, which results in a second-harmonic response. It was realized that probing the ZnO at the band gap results in photo-desorption of the O₂ molecules. Moreover, this response is also found to depend on sample storage time and it is suggested to be related to oxygen diffusion into the thin ZnO film.

The overall conclusion of this work is that silicon monoxide is a strong candidate for future nonlinear optical devices that is compatible with the well established silicon processing technology. Additionally, time-dependent second-harmonic generation is a vital non-contact tool that can be used to study the interaction between ambient air and thin films that are second-harmonic active.

Resumé

Denne Ph.D. afhandling omhandler vekselvirkning mellem lys og ulineære tynde film. Når en ulineær film probes med intens laserlys med en fotonenergi på $\hbar\omega$ vil det generere såkaldte anden-harmoniske fotoner med den dobbelte energi $2\hbar\omega$. Hvordan disse anden-harmoniske fotoner bliver genereret som funktion af forskellige parametre, kan afsløre oplysninger om de strukturelle egenskaber på en makroskopisk og mikroskopisk skala. Optiske komponenter baseret på anden-harmonisk generation er et aktivt forskningsfelt med fokus på udvikling af nye ulineære materialer med et stort ulineæret respons.

I denne afhandling demonstreres det at en standard elektronstråle deponerings metode af siliciummonoxid (SiO) kan føre til en SiO-film, som har et stærkt anden-harmonisk respons. Det er et resultat af deponeringsbetingelserne, som er unikke for elektronstråle deponering, og flere eksperimenter peger i retning af ordnede dipoler i filmen som er kilden til det ulineære respons. Endvidere blev det vist, at igennem en standard litografi proces kan veldefinerede ulineære 2D strukturer nemt konstrueres.

Det blev demonstreret at deponering af SiO under en skrå vinkel, resulterer det i et ulineære repons, der er stærkt afhængig af deponeringsvinklen. Via. denne deponeringsteknik består den fabrikerede tynde film af en porøs tiltet søjle struktur. Ved at analysere det anden-harmoniske respons fra denne type film kan vinklen af de tiltede søjler bestemmes.

Desværre har denne porøse SiO struktur tendens til at oxidere når den kommer i kontakt med atmosfærisk luft. Dette resulterer i et henfald af det i anden-

harmoniske signal, som faktisk kan afsløre dynamikken i oxideringsprocessen. Det tidsafhængige anden-harmoniske respons fra en oxiderende SiO film er et direkte mål på antallet af optagne ilt atomer i SiO filmen. Endvidere blev det vist, at oxidationsprocessen også kan studeres via. lineær optisk spektroskopi gennem skiftet i filmens absorptionsbåndkant.

Vekselvirkningen mellem den omgivende luft og tynde ZnO film blev også undersøgt med tidsafhængig anden-harmonisk generation. Her blev det påvist, at O₂ adsorberet på overfladen inducerer et elektrisk felt, som resulterer i et feltinduceret anden-harmonisk respons. Ved at probe ZnO ved båndgabets energi resulterer det i foton simuleret desorption af O₂ molekylerne fra ZnO overfladen. Dette giver et målbart tab af andenharmonisk-genererede fotoner. Desuden viste det sig, at denne interaktion også er afhængig af prøveopbevaringstiden, hvilket kan være relateret til diffusion af oxygen ind i den tynde ZnO film.

Den overordnede konklusion på dette arbejde er, at siliciummonoxid er en stærk kandidat til fremtidige ulineære optiske enheder, der er kompatibel med den vel-etablerede silicium procesteknologi. Endvidere kan den tidsafhængige andenharmoniske generation bruges som et redskab til at undersøge samspillet mellem den omgivende luft og disse tynde ulineære aktive film.

List of publications

Papers in peer-reviewed journals

1. S.V. Andersen, K. Pedersen, "Second-harmonic generation from electron beam deposited SiO", Optics Express, Vol. 20, Issue 13, pp. 13857-13869 (2012)
2. S.V. Andersen, M.L. Trolle, K. Pedersen, "Growth direction of oblique angle electron beam deposited silicon monoxide thin films identified by optical second-harmonic generation", Applied Physics Letters, Vol. 103, Iss. 23, pg. 231906 (2013).
3. S. V. Andersen, V. Vandalon, R. H. E. C. Bosch, B. W. H. van de Loo, K. Pedersen, and W. M. M. Kessels, "Interaction between O₂ and ZnO probed by time-dependent second-harmonic generation", Applied Physics Letters, Vol. 104, Iss. 5, pg. 051602 (2014).

Presentation

1. Oral presentation at Northern Optics 2012, Title: "Second-harmonic generation from electron beam deposited SiO"
2. Oral presentation at the 10th International Conference on Optics of Surfaces and Interfaces, Title: "Tunable nonlinear optical properties of oblique angle electron beam deposited SiO films"

3. Oral presentation at the 10th International Conference on Optics of Surfaces and Interfaces, Title: "Interaction between O_2 and ZnO probed by time-dependent second-harmonic generation"

Bibliography

1. Maxwell, J. C. *Philos. Trans. Roy. Soc. London* **155**, 459–512 (1865).
2. Jackson, J. and Okun, L. *Rev. Mod. Phys.* **73**(3), 663–680 (2001).
3. Lorenz, L. *Philos. Mag.* **4** **34**(230), 287–301 (1867).
4. Franken, P. A., Hill, A. E., Peters, C. W., and Weinreich, G. *Phys. Rev. Lett.* **7**, 118–119 (1961).
5. Maiman, T. *Nature* **187**(4736), 493–494 (1960).
6. Boyd, R. W. *Nonlinear Optics*. Academic Press, (2003).
7. Terhune, R., Maker, P., and Savage, C. *Phys. Rev. Lett.* **8**(10), 404–406 (1962).
8. Bloembergen, N., Chang, R. K., Jha, S. S., and Lee, C. H. *Phys. Rev.* **174**, 813–822 (1968).
9. McGilp, J. F. *Prog. Surf. Sci* **49**(1), 1 – 106 (1995).
10. Lüpke, G. *Surf. Sci. Rep.* **35**(34), 75 – 161 (1999).
11. G. Lüpke, D.J. Bottomley, v. D. H. *Phys. Rev. B* **47**(16), 10389–10394 (1993).
12. Hoex, B., Gielis, J. J. H., van de Sanden, M. C. M., and Kessels, W. M. M. *J. Appl. Phys.* **104**(11), 113703 (2008).
13. Gielis, J. J. H., Hoex, B., van de Sanden, M. C. M., and Kessels, W. M. M. *J. Appl. Phys.* **104**(7), 073701 (2008).
14. Gielis, J. J. H., Gevers, P. M., Stevens, A. A. E., Beijerinck, H. C. W., van de Sanden, M. C. M., and Kessels, W. M. M. *Phys. Rev. B* **74**(16), 165311 (2006).
15. Dingemans, G., Terlinden, N. M., Pierreux, D., Profijt, H. B., Van De Sanden, M. C. M., and Kessels, W. M. M. *Electrochem. Solid-State Lett.* **14**(1), H1–H4 (2011).

16. Kazansky, P., Dong, L., and Russell, P. *Opt. Lett.* **19**(10), 701–703 (1994).
17. Cazzanelli, M., Bianco, F., Borga, E., Pucker, G., Ghulinyan, M., Degoli, E., Luppi, E., Veniard, V., Ossicini, S., Modotto, D., Wabnitz, S., Pierobon, R., and Pavesi, L. *Nat. Mater.* **11**(2), 148–154 (2012).
18. Jacobsen, R., Andersen, K., Borel, P., Fage-Pedersen, J., Frandsen, L., Hansen, O., Kristensen, M., Lavrinenko, A., Moulin, G., Ou, H., Peucheret, C., Zsigri, B., and Bjarklev, A. *Nature* **441**(7090), 199–202 (2006).
19. Myers, R., Mukherjee, N., and Brueck, S. *Opt. Lett.* **16**(22), 1732–1734 (1991).
20. Guignard, M., Nazabal, V., Troles, J., Smektala, F., Zeghlache, H., Quiquempois, Y., Kudlinski, A., and Martinelli, G. *Opt. Express* **13**(3), 789–795 (2005).
21. Dussauze, M., Fargin, E., Lahaye, M., Rodriguez, V., and Adamietz, F. *Opt. Express* **13**(11), 4064–4069 (2005).
22. Yadav, K., Callender, C. L., Smelser, C. W., Ledderhof, C., Blanchetiere, C., Jacob, S., and Albert, J. *Opt. Express* **19**(27), 26975–26983 (2011).
23. Bauer, S. *J. Appl. Phys.* **80**(10), 5531–5558 (1996).
24. Delestre, A., Lahaye, M., Fargin, E., Bellec, M., Royon, A., Canioni, L., Dussauze, M., Adamietz, F., and Rodriguez, V. *Appl. Phys. Lett.* **96**(9) (2010).
25. Xi, J.-Q., Schubert, M. F., Kim, J. K., Schubert, E. F., Chen, M., Lin, S.-Y., Liu, W., and Smart, J. A. *Nature Photon.* **1**(3), 176–179 (2007).
26. Chhajed, S., Schubert, M. F., Kim, J. K., and Schubert, E. F. *Appl. Phys. Lett.* **93**(25), 251108 (2008).
27. Hawkeye, M. M. and Brett, M. J. *J. Vac. Sci. Technol., A* **25**(5), 1317–1335 (2007).
28. Hohl, A., Wieder, T., van Aken, P., Weirich, T., Denninger, G., Vidal, M., Oswald, S., Deneke, C., Mayer, J., and Fuess, H. *J. Non-Cryst. Solids* **320**(1–3), 255–280 (2003).
29. Baba, Y., Sekiguchi, T., Shimoyama, I., and Hirao, N. *Surf. Sci.* **612**(0), 77 – 81 (2013).
30. Miller, R. C. *Appl. Phys. Lett.* **5**(1), 17–19 (1964).
31. Wang, G., Kiehne, G. T., Wong, G. K. L., Ketterson, J. B., Liu, X., and Chang, R. P. H. *Appl. Phys. Lett.* **80**(3), 401–403 (2002).

32. Neumann, U., Grunwald, R., Griebner, U., Steinmeyer, G., and Seeber, W. *Appl. Phys. Lett.* **84**(2), 170–172 (2004).
33. Cao, H., Wu, J. Y., Ong, H. C., Dai, J. Y., and Chang, R. P. H. *Appl. Phys. Lett.* **73**(5), 572–574 (1998).
34. Djurisić, A. B. and Leung, Y. H. *Small* **2**(8-9), 944–961 (2006).
35. Barry, T. I. and Stone, F. S. *Proc. R. Soc. Lond. A* **255**(1280), 124–144 (1960).
36. Lampe, U. and Müller, J. *Sens. and Actuators* **18**(3-4), 269–284 (1989).
37. Morkoç, H. and Özgür. *Zinc Oxide*. Wiley-VCH, (2008).
38. Armstrong, J., Bloembergen, N., Ducuing, J., and Pershan, P. *Phys. Rev.* **127**(6), 1918–1939 (1962).
39. Herman, W. N. and Hayden, L. M. *J. Opt. Soc. Am. B* **12**(3), 416–427 (1995).
40. Jerphagnon, J. and Kurtz, S. *J. Appl. Phys.* **41**(4), 1667–1681 (1970).
41. Hagimoto, K. and Mito, A. *Appl. Opt.* **34**(36), 8276–8282 Dec (1995).
42. Parsons, G., Elam, J., George, S., Haukka, S., Jeon, H., Kessels, W., M., L., Poodt, P., Ritala, M., and Rossnagel, S. *J. Vac. Sci. Technol., A* **31**(5), 050818 (2013).
43. <http://www.genplot.com/>.
44. <http://www.iontof.com/>.
45. Jellison, G. E. and Modine, F. A. *Appl. Phys. Lett.* **69**(3), 371–373 (1996).
46. Ziegler, J. F. and Manoyan, J. M. *Nucl. Instr. Meth.* **B35**, 215–228 (1989).
47. Argall, F. and Jonscher, A. *Thin Solid Films* **2**(3), 185 – 210 (1968).
48. Hansen, J. L. *Aarhus University*.
49. Iacona, F., Franzò, G., and Spinella, C. *J. Appl. Phys.* **87**(3), 1295–1303 (2000).
50. Inokuma, T., Wakayama, Y., Muramoto, T., Aoki, R., Kurata, Y., and Hasegawa, S. *J. Appl. Phys.* **83**(4), 2228–2234 (1998).
51. Meakin, P. *Phys. Rev. A* **38**, 994–1004 Jul (1988).
52. Nieuwenhuizen, J. M. and Haanstra, H. B. *Philips Tech. Rev.* **27**, 87 (1966).

53. Tait, R., Smy, T., and Brett, M. *Thin Solid Films* **226**(2), 196 – 201 (1993).
54. Tanto, B., Ten Eyck, G., and Lu, T.-M. *J. Appl. Phys.* **108**(2), 026107 (2010).
55. Liao, W.-S. and Lee, S.-C. *J. Appl. Phys.* **80**(2), 1171–1176 (1996).
56. van der Zwan, M. L. W., Bardwell, J. A., Sproule, G. I., and Graham, M. J. *Appl. Phys. Lett.* **64**(4), 446–447 (1994).
57. Tischler, M., Collins, R., Stathis, J., and Tsang, J. *Appl. Phys. Lett.* **60**(5), 639–641 (1992).
58. Yang, D.-Q., Meunier, M., and Sacher, E. *J. Appl. Phys.* **99**(8), 084315 (2006).
59. Cullis, A., Canham, L., and Calcott, P. *J. Appl. Phys.* **82**(3), 909–965 (1997).
60. Mawhinney, D., Glass Jr., J., and Yates Jr., J. *J. Phys. Chem. B* **101**(7), 1202–1206 (1997).
61. Silva, A., Pedersen, K., Li, Z., and Morgen, P. *Thin Solid Films* **520**(2), 697–699 (2011).
62. Drevillon, B. and Vaillant, F. *Thin Solid Films* **124**(34), 217 – 222 (1985).
63. Fritzsche, H. and Tsai, C. *Sol. Energy Mater.* **1**(56), 471 – 479 (1979).
64. Robbie, K., Beydaghyan, G., Brown, T., Dean, C., Adams, J., and Buzea, C. *Rev. Sci. Instrum.* **75**(4), 1089–1097 (2004).
65. Tauc, J., Grigorovici, R., and Vancu, A. *Phys. Status Solidi B* **15**(2), 627–637 (1966).
66. Raider, S., Flitsch, R., and Palmer, M. *J. Electrochem. Soc.* **122**(3), 413–418 (1975).
67. Mende, G., Finster, J., Flamm, D., and Schulze, D. *Surf. Sci.* **128**(1), 169 – 175 (1983).
68. Cerofolini, G. and Meda, L. *J. Non-Cryst. Solids* **216**(0), 140–147 (1997).
69. Sah, C., Sello, H., and Tremere, D. *J. Phys. Chem. Solids* **11**(3-4), 288–298 (1959). cited By (since 1996)12.
70. *Handbook of Optics*. Vol. 2. McGraw-Hill, 2nd edition edition, (1994).
71. Feng, Z. C., editor. *Handbook of Zinc Oxide and Related Materials: Volume One, Materials*. CRC Press, Boca Raton, (2013).

72. Kawamura, I., Imakita, K., Fujii, M., and Hayashi, S. *Appl. Phys. Lett.* **103**(20), 201119 (2013).
73. Biagi, G., Holmgaard, T., and Skovsen, E. *Opt. Express* **21**(4), 4355–4360 (2013).
74. Skovsen, E., Søndergaard, T., Fiutowski, J., Simesen, P., Osadnik, A., Lützen, A., Rubahn, H.-G., Bozhevolnyi, S. I., and Pedersen, K. *Opt. Express* **20**(15), 16715–16725 (2012).
75. Berini, P. *Adv. Opt. Photon.* **1**(3), 484–588 Nov (2009).
76. Randhawa, S., Krasavin, A. V., Holmgaard, T., Renger, J., Bozhevolnyi, S. I., Zayats, A. V., and Quidant, R. *Appl. Phys. Lett.* **98**(16), 161102 (2011).
77. Harris, K., Huizinga, A., and Brett, M. *Electrochem. Solid-State Lett.* **5**(11), H27–H29 (2002).
78. Wu, Y., Hermkens, P. M., van de Loo, B. W. H., Knoops, H. C. M., Potts, S. E., Verheijen, M. A., Roozeboom, F., and Kessels, W. M. M. *J. Appl. Phys.* **114**(2), 024308 (2013).
79. Vayssieres, L. *Adv. Mater.* **15**(5), 464–466 (2003).
80. Pedersen, K., Fisker, C., and Pedersen, T. G. *Phys. Status Solidi C* **5**(8), 2671–2674 (2008).
81. Li, Y., Meng, G. W., Zhang, L. D., and Phillipp, F. *Appl. Phys. Lett.* **76**(15), 2011–2013 (2000).
82. Meulenkaamp, E. *J. Phys. Chem. B* **102**(29), 5566–5572 (1998).
83. Wu, L., Wu, Y., and Lä, Y. *Mater. Res. Bull.* **41**(1), 128–133 (Wu2006).
84. Özgür, U., Alivov, Y. I., Liu, C., Teke, A., Reshchikov, M. A., Doğan, S., Avrutin, V., Cho, S.-J., and Morkoç, H. *J. Appl. Phys.* **98**(4), 041301 (2005).
85. Chen, Y., Bagnall, D., Koh, H., Park, K., Hiraga, K., Zhu, Z., and Yao, T. *J. Appl. Phys.* **84**(7), 3912–3918 (1998).
86. Minami, T., Ida, S., Miyata, T., and Minamino, Y. *Thin Solid Films* **445**(2), 268–273 DEC 15 (2003). 3rd International Symposium on Transparent Oxide Thin Films for Electronics and Optics (TOEO-3), TOKYO, JAPAN, APR 10-11, 2003.
87. Minami, T. *MRS Bull.* **25**(8), 38–44 (2000).

88. Repins, I., Contreras, M. A., Egaas, B., DeHart, C., Scharf, J., Perkins, C. L., To, B., and Noufi, R. *Prog. Photovolt. Res. Appl.* **16**(3), 235–239 MAY (2008).
89. Look, D. *Mater. Sci. Eng., B* **80**(13), 383–387 (2001).
90. Kong, Y., Yu, D., Zhang, B., Fang, W., and Feng, S. *Appl. Phys. Lett.* **78**(4), 407–409 (2001).
91. Garner, W. E. and Veal, F. J. *J. Chem. Soc.* **0**, 1487–1495 (1935).
92. Soci, C., Zhang, A., Xiang, B., Dayeh, S. A., Aplin, D. P. R., Park, J., Bao, X. Y., Lo, Y. H., and Wang, D. *Nano Lett.* **7**(4), 1003–1009 (2007).
93. Li, Q. H., Gao, T., Wang, Y. G., and Wang, T. H. *Appl. Phys. Lett.* **86**(12), 1–3 (2005).
94. Kind, H., Yan, H., Messer, B., Law, M., and Yang, P. *Adv. Mater.* **14**(2), 158–160 (2002).
95. Shultz, A. N., Jang, W., III, W. H., Baer, D., Wang, L.-Q., and Engelhard, M. *Surf. Sci.* **339**, 114–124 (1995).
96. Kobayashi, E., Matsuda, K., Mizutani, G., and Ushioda, S. *Surf. Sci.* **427–28**, 294–297 JUN 1 (1999). 9th International Conference on Vibrations at Surfaces (VAS9), HAYAMA, JAPAN, OCT 12-16, 1998.
97. *Corropondence with Roger Bosch. XRD measurements performed at TU/e .*
98. Neamen, D. A. *Semiconductor physics and devices - basic principles*. McGraw-Hill, 3rd edition, (2003).
99. Meyer, B., Marx, D., Dulub, O., Diebold, U., Kunat, M., Langenberg, D., and Wäll, C. *Angew. Chem. Int. Ed.* **43**(48), 6641–6645 (2004).
100. Dulub, O., Meyer, B., and Diebold, U. *Phys. Rev. Lett.* **95**, 136101 (2005).
101. Li, Y., Della Valle, F., Simonnet, M., Yamada, I., and Delaunay, J.-J. *Appl. Phys. Lett.* **94**(2) (2009).
102. Shan, F., Liu, G., Lee, W., Lee, G., Kim, I., and Shin, B. *Appl. Phys. Lett.* **86**(22) (2005).
103. Shan, F. K., Kim, B. I., Liu, G. X., Liu, Z. F., Sohn, J. Y., Lee, W. J., Shin, B. C., and Yu, Y. S. *J. Appl. Phys.* **95**(9), 4772–4776 (2004).
104. McCluskey, M. and Jokela, S. J. *J. Appl. Phys.* **106**(7), 071101–071101–13 (2009).

105. Liu, H., Zeng, F., Lin, Y., Wang, G., and Pan, F. *Appl. Phys. Lett.* **102**(18), 181908 (2013).
106. Tanaka, K. and Blyholder, G. *J. Phys. Chem.* **76**(22), 3184–3187 (1972).
107. Fujitsu, S., Koumoto, K., Yanagida, H., Watanabe, Y., and Kawazoe, H. *Jap. J. Appl. Phys.* **38**(Part 1, No. 3A), 1534–1538 (1999).
108. Yan, Y., Al-Jassim, M., and Wei, S.-H. *Phys. Rev. B* **72**(16) (2005).
109. Xu, H., Zhang, R. Q., and Tong, S. Y. *Phys. Rev. B* **82**, 155326 (2010).
110. Lunsford, J. H. and Jayne, J. P. *J. Chem. Phys.* **44**(4), 1487–1492 (1966).
111. Petrov, G. I., Shcheslavskiy, V., Yakovlev, V. V., Ozerov, I., Chelnokov, E., and Marine, W. *Appl. Phys. Lett.* **83**(19), 3993–3995 (2003).
112. Schmidt, O., Kiesel, P., de Walle, C. G. V., Johnson, N. M., Nause, J., and Döhler, G. H. *Jap. J. Appl. Phys.* **44**(10), 7271–7274 (2005).
113. Bandyopadhyay, S., Paul, G. K., Roy, R., Sen, S. K., and Sen, S. *Mater. Chem. Phys.* **74**(1), 83–91 (2002).

Appendices

A

**Optics Express, Vol. 20, Issue 13, pp.
13857-13869 (2012)**

Second-harmonic generation from electron beam deposited SiO

by

Søren Vejling Andersen and Kjeld Pedersen

Second-harmonic generation from electron beam deposited SiO films

Søren Vejling Andersen* and Kjeld Pedersen

Department of Physics and Nanotechnology at Aalborg University, Skjernvej 4a, DK-9220
Aalborg Øst, Denmark

[*sva@nano.aau.dk](mailto:sva@nano.aau.dk)

Abstract: It is demonstrated that as-grown e-beam deposited SiO_x thin films on fused silica substrates show a second-order nonlinear response that is dependent on film thickness. Using a Maker fringes method the effective nonlinear coefficient for a SiO thin film is estimated to be comparable to that of crystalline quartz. Variation of process parameters has been used to investigate the origin of the nonlinear response. The second-harmonic signal is very sensitive to annealing of the film and can be totally removed by annealing at a few hundred degrees. It is also demonstrated that a retarding grid that traps charged particles between the crucible and the sample reduces the nonlinear signal from a SiO thin film significantly. It is suggested that oriented dipoles arise during deposition due to a negatively charged film from oxygen ions, thus, resulting in a non-centrosymmetric film. Finally, using e-beam lithography, well-defined nonlinear 2D structures can be synthesized, thus opening the door to a new and practical way to create nonlinear structures for planar waveguide technology.

© 2013 Optical Society of America

OCIS codes: (190.0190) Nonlinear optics; (160.4330) Nonlinear optical materials; (190.4360) Nonlinear optics, devices; (310.0310) Thin films; (130.2755) Glass waveguides

References and links

1. R. A. Myers, N. Mukherjee, and S. R. J. Brueck, "Large second-order nonlinearity in poled fused silica," *Opt. Lett.* **16**, 1732-1734 (1991).
2. K. Pedersen, S. I. Bozhevolnyi, J. Arentoft, M. Kristensen, and C. Laurent-Lund, "Second-harmonic scanning optical microscopy of poled silica waveguides," *J. Appl. Phys.* **88**, 3872-3878 (2000).
3. M. Guignard, V. Nazabal, J. Troles, F. Smektala, H. Zeghlache, Y. Quiquempois, A. Kudlinski, and G. Martinelli, "Second-harmonic generation of thermally poled chalcogenide glass," *Opt. Express* **13**, 789-795 (2005).
4. M. Dussauze, E. Fargin, M. Lahaye, V. Rodriguez, and F. Adamietz, "Large second-harmonic generation of thermally poled sodium borophosphate glasses," *Opt. Express* **13**, 4064-4069 (2005).
5. K. Yadav, C.L. Callender, C.W. Smelser, C. Ledderhof, C. Blanchetiere, S. Jacob, and J. Albert, "Giant enhancement of the second harmonic generation efficiency in poled multilayer silica glass structures," *Opt. Express* **26**, 26975-26983 (2011).
6. T. Ning, H. Pietarinen, O. Hyvriinen, J. Simonen, G. Genty, and M. Kauranen, "Strong second-harmonic generation in silicon nitride films," *Appl. Phys. Lett.* **100**, 161902 (2012).
7. F. Iacona, G. Franzo and C. Spinella, "Correlation between luminescence and structural properties of Si nanocrystals," *J. Appl. Phys.* **87**, 1295-1303 (2000).
8. P. G. Kazansky, A. Kamal, and P. St. J. Russell, "High second-order nonlinearities induced in lead silicate glass by electron-beam irradiation," *Opt. Lett.* **18**, 693-695 (1993).
9. Q. Liu, X. Zhao, K. Tanaka, A. Narazaki, K. Hirao, F. Gan, "Second-harmonic generation in GeAsS glasses by electron beam irradiation and analysis of the poling mechanism," *Opt. Commun.* **198**, 187 (2001).
10. Q. Liu, B. Poumellec, R. Blum, G. Girard, J.-E. Boure, A. Kudlinski, and G. Martinelli, "Stability of electron-beam poling in N or Ge-doped H:SiO₂ films," *Appl. Phys. A (Mater. Sci. Pro)* **81**, 1213 (2005).

11. G. Myburg and F. D. Aurret, "Influence of the electron-beam evaporation rate of PT and the semiconductor carrier density on the characteristics of PT/normal-GAAS schottky contacts.," J. Appl. Phys. **71**, 6172-6176 (1992).
 12. D. Hoffman and D. Leibowitz, "Effect of Substrate Potential on Al_2O_3 Films Prepared by Electron Beam Evaporation," J. Vac. Sci. Technol. **9**, 326-329 (1972).
 13. G.E. Jellison and F. A. Modine, "Parameterization of the optical functions of amorphous materials in the inter-band region," Appl. Phys. Lett. **69**, 371-373 (1996).
 14. W. N. Herman and L. M. Hayden, "Maker fringes revisited: second-harmonic generation from birefringent or absorbing materials," J. opt. Soc. Am. B **12**, 416-427 (1995).
 15. J. Jerphagnon and S. K. Kurtz, "Maker Fringes: A Detailed Comparison of Theory and Experiment for Isotropic and Uniaxial Crystals," J. Appl. Phys. **41**, 1667-1681 (1970).
 16. P.G. Kazansky and P.St.J. Russel, "Thermally poled glass: frozen-in electric field or oriented dipoles?," Opt. Commun. **110**, 611-614 (1994).
 17. J. Tauc, "Optical properties of non-crystalline solids," F. Abeles (Ed.), Optical Properties of Solids, North-Holland, Amsterdam 277 (1972).
 18. K. Hagimoto and A. Mito, "Determination of the second-order susceptibility of ammonium dihydrogen phosphate and α -quartz at 633 and 1064 nm," Appl. Opt. **34**, 8276-8282 (1995).
 19. R. C. Miller, "Optical second harmonic generation in piezoelectric crystals.," Appl. Phys. Lett. **5**, 17-19 (1964).
 20. R.W. Boyd, *Nonlinear Optics*, Third Edition, (Elsevier, 2008).
 21. C. Bucci and R. Fieschi, "Ionic Thermoconductivity. Method for the Investigation of Polarization in Insulators," Phys. Rev. Lett. **12**, 16-19 (1964).
 22. SRIM simulation software based on: J. F. Ziegler and J. M. Manoyan, "The Stopping of Ions in Compounds," Nucl. Instr. Meth. **B35**, 215-228 (1989).
 23. A. Kameyama, A. Yokotani, and K. Kurosawa, "Identification of defects associated with second-order optical nonlinearity in thermally poled high-purity silica glasses," J. Appl. Phys. **89**, 4707-4713 (2001).
 24. F. Argalland and A.K. Jonscher, "Dielectric properties of thin films of aluminium oxide and silicon oxide," Thin Solid Films **2**, 185-210 (1968).
 25. H. L. Hampsch, J. M. Torkelson, S. J. Bethke, and S. G. Grubb, Second harmonic generation in corona poled, doped polymer films as a function of corona processing," J. Appl. Phys. **67**, 1037-1042 (1990).
 26. T. G. Alley, S.R.J. Brueck and, R. A. Myers, "Space charge dynamics in thermally poled fused silica," J. Non-Cryst. Solids **242** 165176 (1998).
-

1. Introduction

The development of new nonlinear optical materials compatible with Si process technology has been an active research field over the past two decades. Poling of glasses is considered a promising process that can lead to large second-order nonlinearities over a broad spectral range for a wide range of glass compositions. In the thermal poling process electric field induced rearrangement of ions at elevated temperatures lead to a built-in electric field after cooling to room temperature [1]. In combination with bulk allowed third-order nonlinearities this results in an effective second-order effect allowing second-harmonic generation (SHG) as well as electro optic effects. The two processes, SHG and linear electro optic effect, have the same selection rules and SHG is often used to map out the spatial distribution of induced nonlinearities [2]. Typically the built-in field exists in a few micrometers thick layer at the surface of the material. Effective nonlinear coefficients up to a few pm/V have been obtained depending on the glass composition [3, 4]. More than two orders of magnitude enhancement of SHG compared to a bulk poled silica glass has been obtained from a poled stack of alternating doped and un-doped layers of silica [5]. Very recently, it has been demonstrated that silicon nitride films prepared on fused silica substrates by Plasma Enhanced Chemical Vapor Deposition (PECVD) has a strong SHG response even without poling of the deposited film [6].

SiO_x films are amorphous with a range of oxidation stages of Si atoms (Si^{n+} with $0 < n < 4$) depending of deposition conditions and external excitations. Such layers have a large number of applications, for instance as protective coatings or as part of dielectric stacks for mirrors and antireflective coatings. High temperature annealing of SiO_x films leads to light-emitting layers through formation of Si nanocrystals embedded in a silica matrix [7]. The relatively open structure of the oxide allows for inclusion of ionic species, where hydrogen is expected to be the most prominent impurity.

Electron-beam irradiation of doped SiO₂ glass have shown to induce a second harmonic response due to an electrostatic space-charge field formed by the electrons [8, 9, 10]. This SHG mechanism resembles that of thermally poled glass. However, also high-energy electron beam deposition techniques are known to affect structural, electrical and optical properties of thin films [11, 12]. In this paper we show that e-beam deposition of SiO leads to a film with oriented dipoles and thus an effective second order nonlinearity giving rise to efficient SHG. The focus of this work is on description of the second-order nonlinearity of e-beam grown SiO layers and the deposition conditions leading to SHG rather than a detailed microscopic analysis of the materials aspects behind the nonlinear effect. SHG signals as functions of incidence angle of the light, thickness of the SiO layers, and the wavelength of the pump light are presented. It is suggested that the nonlinearity is formed directly through inclusion of ionized species during the deposition process and a negatively charged film due to oxygen ions. It is thus not necessary to apply electrical contacts and a thermal process as in conventional poling. Furthermore, the process allows straight forward use of conventional lithography for in-plane definition of non-linear optical elements. The symmetry of the material with a preferred direction perpendicular to the surface is similar to that of poled materials. One can thus consider the same type of active optical components produced from SiO films as from poled glass films.

2. Experimental

2.1. Thin film deposition

Several SiO thin films with different thickness have been deposited at room temperature onto fused silica and Si(100) substrates using an -7.5 kV electron beam evaporation technique with a deposition rate of 0.5-1 Å/s. The electron beam heated 3 mm-6 mm SiO grains with a 99.99 % purity placed in a graphite crucible. The advantage of using fused silica substrates is its lack of SHG response and that it is transparent in the UV to ~250 nm. The substrates were cleaned in an ultrasonic bath of acetone followed by ethanol and then blow dried by N₂ before they were loaded into the deposition system through a load-lock. A Si wafer was placed next to the silica substrates and received the same deposition of SiO_x. Prior to deposition the system was pumped down to a base pressure of 1·10⁻⁶ mbar (to prevent oxidation of SiO during deposition). By crunching SiO₂ and SiO grains to a finer powder a mixture for deposition of SiO_{x~1.5} films was obtained. Additionally, an e-beam deposited SiO₂ film on fused silica was prepared. Furthermore, the same deposition chamber included a rf-magnetron source that was used for sputter deposition of a SiO thin film using a 99.9 % pure SiO target in an argon plasma.

2.2. Material composition

The stoichiometry was investigated with a Rutherford backscattering spectrometry (RBS) technique. He⁺ ions of 2 MeV and a backscattering angle between 30° and 70° were used. Measurements on three different SiO samples with the thickness of 344 nm, 550 nm, and 902 nm revealed that the films deposited from the SiO grains are SiO_{~0.95} thin films with a homogeneous distribution of the Si and O atoms throughout the films (data not shown). The SiO_x stoichiometry was calculated from the powder mixture. Additionally, secondary ion mass spectrometry (SIMS) was used to determine the hydrogen content in the SiO films.

2.3. Linear optical characterization methods

A Sentech SE 850 ellipsometer was used to estimate the refractive index and the absorption coefficient utilizing the Jellison and Modine model [13] to represent the SiO films on the silicon substrates. This includes an estimation of the film thickness and was verified with RBS. A UV-3600 Shimadzu UV-VIS-NIR spectrometer was used to investigate the change in linear optical

properties of the SiO thin films on fused silica after annealing in N₂ or air atmospheres at various temperatures.

2.4. Nonlinear optical characterization methods

The SHG spectroscopy experiments were performed using a Nd:YAG-laser pumped optical parametric oscillator (OPO) system delivering 5-ns pulses at 10 Hz repetition rate. Pulse energies of the order of 1 mJ focused to a 1 mm spot diameter on the sample were used. No signs of sample damage were observed, even after illumination for several hours. The spectral composition of the up-converted transmitted light was investigated with a monochromator. A photomultiplier tube coupled to gated electronics was used to detect the nonlinear signals.

After analyzing the up-converted light at a few selected pump wavelengths the monochromator was removed from the setup during spectroscopic measurements. Extraction of the SHG light in the transmitted beam was done with a few combinations of colored glass filters to cover the investigated spectral region. A normalizing reference signal without Maker fringes and with a magnitude comparable to that of the thicker SiO samples was obtained by placing a wedge-shaped quartz crystal at the position of the samples.

Measurements as a function of angle of incidence were performed at pump wavelengths of 760 nm and 1350 nm, and again the measurements were normalized to the reference in order to compare the signal magnitudes of the different samples.

Maker fringes appearing in the angle of incidence scans of SHG from a 1.15-mm thick quartz disc was used to estimate absolute values of the nonlinearity of a SiO film.

3. Theoretical considerations

Herman and Hayden [14] showed that the transmitted SHG signal from an isotropic and absorbing slab with the thickness L on a substrate pumped with λ_p is given by:

$$P_{2\omega}^{\gamma \rightarrow p} = \frac{128\pi^3}{cA} \frac{[t_{af}^{\gamma}]^4 [t_{fs}^{2p}]^2 [t_{sa}^{2p}]^2}{n_2^2 c_2^2} P_\omega^2 \left(\frac{2\pi L}{\lambda_p} \right)^2 d_{eff}^2 \exp[-2(\delta_1 + \delta_2)] \frac{\sin^2 \Psi + \sinh^2 \Omega}{\Psi^2 + \Omega^2}. \quad (1)$$

The effective d_{eff} coefficient for C_{∞v} space symmetry are

$$d_{eff}^{\gamma \rightarrow p} = \begin{cases} 2d_{15}c_1s_1c_2 + d_{31}c_1^2s_2 + d_{33}s_1^2s_2 & \gamma \rightarrow p \\ d_{31}s_2 & \gamma \rightarrow s. \end{cases} \quad (2)$$

Here we have assumed $d_{15}=d_{31}$ (Kleinman symmetry). The γ denotes if the fundamental wavelength is s or p polarized. The Fresnel transmission coefficients at the fundamental and SHG wavelengths are denoted as $t^{1\gamma}$ and t^{2p} , respectively, and subscripts af , fs and sa refer to air-film, film-substrate and substrate-air interfaces, respectively. Furthermore,

$$\begin{aligned} s_m &= 1/n_m \sin(\theta) \\ c_m &= \sqrt{1 - s_m^2}, \quad m = 1, 2 \\ \Psi &= (2\pi L/\lambda_p)(n_1c_1 - n_2c_2) \\ \Omega &= \delta_1 - \delta_2 = (2\pi L/\lambda_p)(n_1\kappa_1/c_1 - n_2\kappa_2/c_2). \end{aligned}$$

Here θ is the angle of incidence of the fundamental wavelength. The subscripts $m=1$ and $m=2$ denote the fundamental and SHG wavelength, respectively. The refractive index and absorption coefficient are n_m and κ_m , respectively. Thereby using the work by Herman and Hayden the ratio between the two nonlinear coefficients d_{33}/d_{31} can be estimated.

In order to estimate the effective nonlinear coefficient, d_{eff} , the measured SHG signal from a 1.15-mm thick quartz disc was used. By combining Eq. (1) with the work by Jerphagnon and Kurtz [15] to describe the quartz crystal the signal ratio between the SiO film and quartz signals can be expressed, thus, a estimation of d_{eff} can be made.

4. Experimental results and discussions

Figure 1(a) shows a monochromator scan of the transmitted SHG signal from a 500-nm thick SiO_{~1.5} film pumped at 760 nm. The relatively narrow spectral peak centered at approximately at 380 nm indicates that the measured signal has to be SHG arising from the SiO_{~1.5} film. The same was realized for several SiO films. On the other hand, neither a 500-nm thick e-beam deposited SiO₂ film nor a 160-nm thick rf-magnetron sputtered SiO film showed detectable SHG signals. Already from these observations it is clear that charging effects from the e-beam and the composition of the deposited film are important in the creation of the second order nonlinearities.

4.1. SHG signal dependence on angle of incidence and film thickness

The transmitted p-p polarized SHG as a function of angle of incidence from different SiO samples with various thicknesses is presented in Fig. 1(b). On the left and right hand sides of the figure, pump wavelengths of 1350 nm and 760 nm were used, respectively. Clearly, there is a strong angular dependence and the SHG intensity peaks around 55-60 degrees angle of incidence, which has also been observed for poled silica [1]. The solid lines are the best fits achieved using Eq. (1) together with the refractive index and absorption coefficients estimated from ellipsometric measurements on SiO films on silicon.

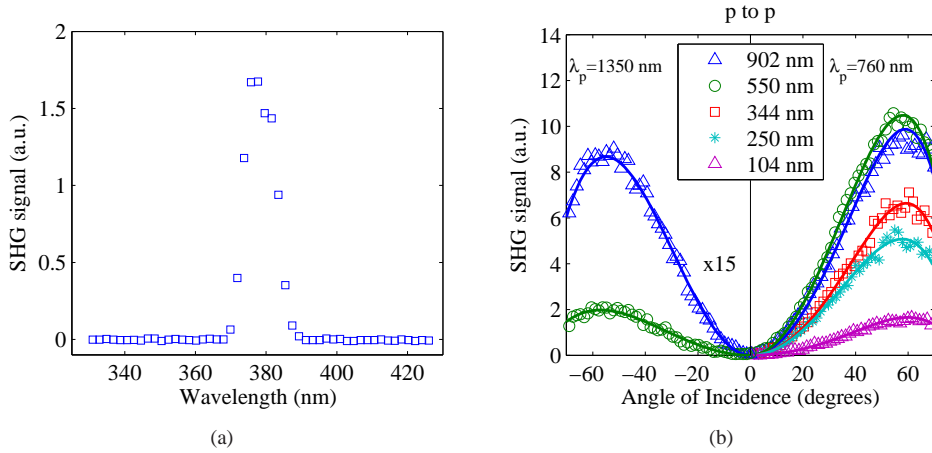


Fig. 1: Spectral and angular dependence of SHG from SiO films. a) The second harmonic signal between 300 nm and 500 nm from a 500-nm thick SiO_{~1.5} film excited by a pump beam at 760 nm. b) Angular dependences of the SHG signal from the SiO thin films with the thickness between 104 nm to 902 nm. On the left hand side and the right hand side, respectively, 1350 nm and 760 nm excitation wavelength were used. Symbols are experimental results and the solid lines are the best fits using Eq. (1). Notice that a factor of 15 has been multiplied to the signal strength on left hand side.

According to Kazansky and Russel [16] the ratio d_{33}/d_{31} should be 3 for an electric-field-induced mechanism. In the current experiments this ratio has been extracted from the measured

angle-of-incidence-dependence for p-polarized SHG. The ratio varied in the range from 2 to 4 for the different films with no particular tendency with film thickness. It is suspected that observed variations in SHG among films may be caused by differences in the traces of the e-beam in the crucibles during deposition. With the variations in the ratio seen in the current experiments it is not possible to use the ratio d_{33}/d_{31} to determine the origin of the nonlinearity.

In Fig. 1(b) it is noticed that with 760 nm pump light the growth in intensity seems to saturate for thick films as the signal levels are the same for the 550- and 902-nm thick films. To understand this we need to take a look at the linear optical properties.

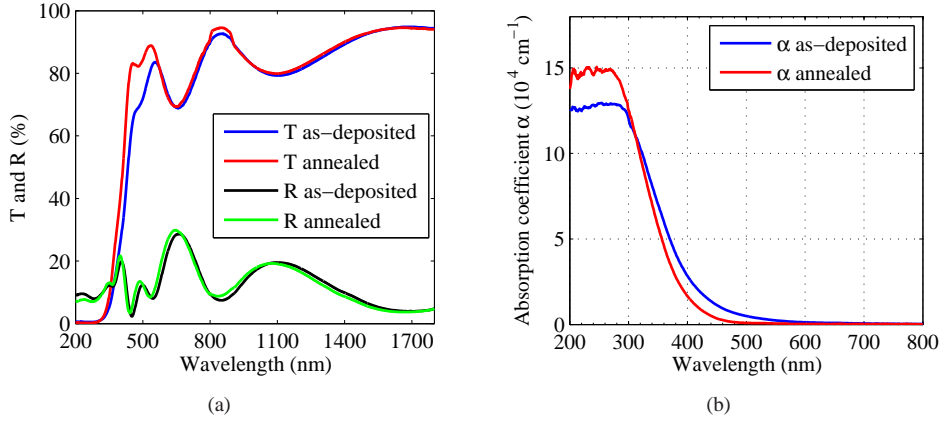


Fig. 2: The linear optical properties of a 550-nm thick SiO film. a) The measured transmittance (T) and reflection (R) curves of the as-deposited film and after annealing at 440°C for 30 min in a N_2 atmosphere. The oscillations are due to interference effects which are included in the model of the absorption coefficient (α). b) The calculated absorption spectra from the data in Fig 2(a).

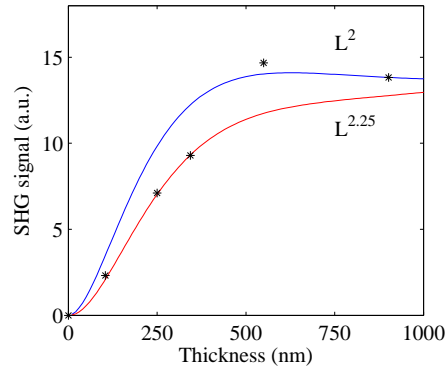


Fig. 3: The SHG signal as a function of film thickness. The stars are the SHG intensities at 57 degrees angle of incidence taken from the right side of Fig. 1(b). The curves are the calculated SHG signal using Eq. (1) with different dependencies on film thickness.

The transmittance and reflectance curves alongside with the calculated absorption coefficient, α , are presented in Fig. 2(a) and Fig. 2(b) for a 550-nm thick SiO film on fused silica. By

using a Tauc plot [17] the estimated energy band gap for the as-deposited film is approximately $E_{opt} \sim 2.5$ eV. Thus, an absorption, $\alpha \sim 4 \cdot 10^{-4} \text{cm}^{-1}$, of our SHG signal within the SiO film occurs when using 760 nm as the pump wavelength as in this present experiments.

The left hand side of Fig. 1(b) shows the behavior of the SHG signal when using a pump wavelength of 1350 nm. Now the 902-nm thick sample has an average signal strength about ~ 4.8 times that of the 550-nm thick sample between 50-60 degrees angle of incidence. According to Eq. (1) the signal strength grows with the thickness squared, meaning we should expect the 902-nm thick film to have a signal strength ~ 2.7 times larger than the 550-nm thick film without absorption. The higher experimental value may be explained by Fig. 3, which shows the variation of the SHG signal at 57 degrees angle of incidence taken from the right hand side of Fig. 1(b). The curves are the calculated SHG signal using Eq. (1) with different dependencies on film thickness and normalized to fit the data. The form of the curves can be understood from a simplified version of Eq. (1):

$$P_{2\omega} \propto L^{\beta} e^{(-2\alpha L)} \quad (3)$$

with the first factor representing the signal growth with increasing film volume ($\beta=2$ in Eq. (1)) while the exponential factor represent the absorption of the SHG light. The almost linear initial growth of SHG with thickness is best represented by $\beta=2.3$ when absorption is taken into account (the red curve). As the thickness grows β appears to be closer to 2 as expected. It is suggested that variations in β may reflect the complicated charge distribution in the film. A value of β larger than 2 is consistent with the fast growth of the signal observed at 1350 nm as mentioned above.

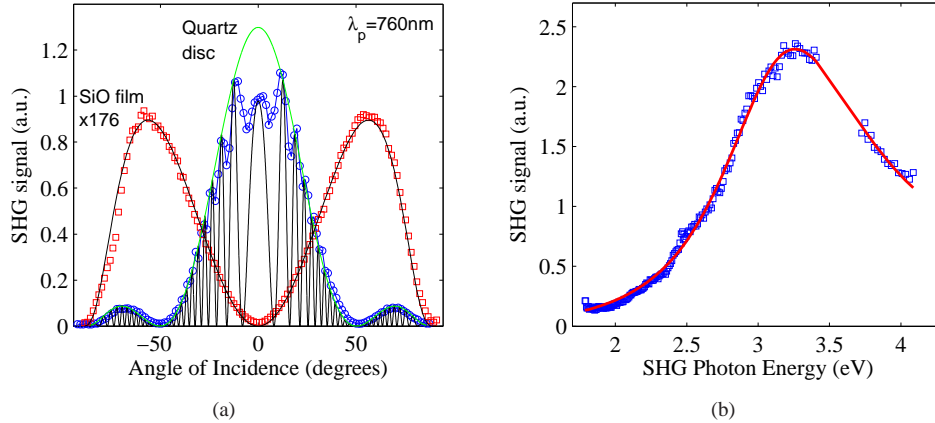


Fig. 4: The angular and pump energy dependence of the SHG signal. a) The SHG signal measured from an 1.15-mm thick quartz disc presented by blue circles and fitted with the work from [15] represented by a black curve. The green curve is the expected SHG signal from the quartz disc without any Maker fringes. The red squares are the SHG measurements from a 550-nm thick SiO film fitted with Eq. (1). The SiO SHG signal is multiplied by 176. Here $\lambda_p = 760$ nm. b) The transmitted SHG from a 550-nm thick SiO film on fused silica as a function of SHG photon energy. The OPO is not tunable in the region around degeneracy at 710 nm corresponding to SHG photon energies around 3.5 eV. This leads to the “hole” in the spectrum at this energy. The solid curve is a fit of a Lorentzian that helps to determine the resonance position to ~ 3.3 eV.

Figure 4(a) shows the SHG signal, $\lambda_p = 760$ nm, as a function of angle of incidence from a 1.15-mm thick quartz disc and from a 550-nm thick SiO film, respectively, presented with blue

circles and red squares. The green curve is the envelope curve that represents the maximum SHG signal from the quartz disc. The SHG signal in Fig. 4(a) from the SiO film is multiplied by 176 for proper presentation. This large difference in signal strength is due to the large difference between the thickness of the SiO thin film and the optical coherence length of quartz. The calculated coherence length of quartz at these wavelengths is $\sim 7.6\mu m$. Notice that the squared ratio between this coherence length and the SiO film thickness is 190. Thus, the SHG response of SiO is compatible to that of quartz.

By using Eq. (1) to describe the transmitted SHG signal from the absorbing 550-nm thick SiO film on a substrate and the work by Jerphagnon and Kurtz [15] to describe the quartz crystal the ratio between the SiO film and quartz signals can be expressed. Then, by calculating the ratio between the expected SHG signal at normal incidence from quartz, without Maker fringes, and the SiO film at signal peak, in this case ~ 57 degrees angle of incidence, see Fig. 4(a), the ratio $d_{eff}^{(SiO)} / d_{11}^{(q)}$ can be evaluated.

By using the value $d_{11} = 0.31$ pm/V reported by Hagimoto and Mito [18] for quartz at an excitation wavelength of 633 nm, and considering Miller's rule [19], the $d_{eff}^{(SiO)}$ is calculated to 0.17 pm/V. Thus, the e-beam deposited SiO thin film has an effective nonlinear coefficient that is comparable to that of crystalline quartz.

4.2. SHG signal dependence on wavelength

Figure 4(b) shows the measured SHG signal as a function of the SHG photon energy normalized to the reference SHG signal from a wedge shaped quartz crystal. The data were fitted with a Lorentzian to determine the resonance peak position to be at ~ 3.3 eV. The nonlinear response (d_{eff} in Eq. (1)) is thus dominated by a two-photon resonance near ~ 3.3 eV [20]. The peak at 3.3 eV corresponds very well to the linear calculated absorption spectra shown in Fig. 2(b).

4.3. SHG signal dependence on annealing temperature

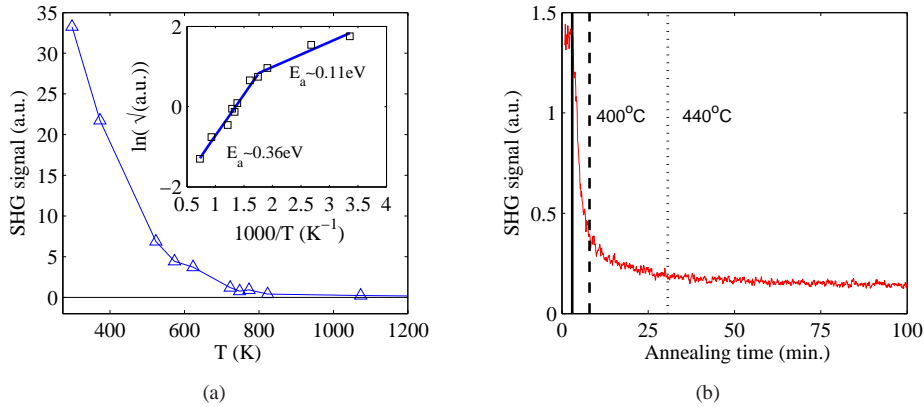


Fig. 5: Temperature dependence of SHG SiO films. a) 11 pieces of a 500-nm thick $SiO_{1.5}$ thin film annealed at different temperatures in a N_2 atmosphere. The activation energy was estimated by a linear fit as illustrated in the insert. b) The SHG signal from a 902-nm thick SiO film while annealed to $440^\circ C$ in an air atmosphere.

The nonlinearity of the e-beam deposited SiO_x films is sensitive to the sample temperature and can be removed completely through annealing. For instance, annealing a 500-nm thick $SiO_{1.5}$ film in N_2 at $100^\circ C$ for 30 minutes reduced the SHG signal by a factor of 1.5. Figure

5(a) shows the loss of SHG signal when 11 pieces of an as-deposited 500-nm thick $\text{SiO}_{1.5}$ sample are annealed for 30 min in a N_2 atmosphere at different temperatures. Every point is the average SHG signal measured by using pump wavelengths between 720 nm and 1000 nm. Notice that the SHG signal can be significantly reduced by annealing at 500°C. Following the work of Bucci and Fieschi [21] on annealing of induced polarizations in insulators an activation energy is estimated as shown in the inserted Arrhenius plot in Fig. 5(a). Here the square root of the SHG signal is used as the SHG signal is proportional to d_{eff}^2 . As indicated in the insert two processes may be at play, one with an activation energy of 0.11 eV and another at 0.36 eV.

In another experiment the SHG signal was measured from a 902-nm thick SiO film while heating in free air up to 440°C. Fig. 5(b) shows the decay of the SHG signal recorded during constant heating of the sample. The three vertical lines starting from the left to the right denotes when the temperature is turn on, when it reaches 400°C and finally stabilizes at 440°C. When the sample subsequently was cooled down to room temperature the SHG signal remained unchanged and the nonlinearity was thus permanently reduced.

The linear transmittance curve (not shown here) behaved the same way as seen in Fig. 2(a), where the 550-nm thick SiO film annealed in N_2 atmosphere became more transparent. This suggests that the reduction in SHG signal is not due to oxidation of the SiO films.

4.4. Origin of the nonlinear response

It is well known that the energetic electron beams used in e-beam deposition systems will affect the properties of the deposited film. Often a grid is used in front of the evaporator in order to prevent charged particles from reaching the substrate. Hoffman and Leibowitz [12] demonstrated that Al_2O_3 films deposited on glass slides from an e-beam source became brown in color if a buildup of negative charge on the insulating substrate was present. Furthermore, they argued that the electron beam created dissociated positive Al ions and negative O ions, thus, the negatively charged substrate repels the oxygen ions thus altering the stoichiometry, resulting in a brown Al_2O_3 film. In analogy with these experiments we placed a mesh grid ($\sim 50\%$ transmittion) consisting of stainless steel 15 cm above the crucible containing the SiO grains. Applying the same -7.5 kV on the mesh grid as for the e-gun, works as an ion trap that repels both O ions and electrons. A blueish plasma about 3-4 cm high rising from the crucible towards the grid was visible during deposition of a 230-nm thick SiO sample. The blueish color is consistent with an oxygen plasma. Figure 6 shows the SHG signal, $\lambda_{pump} = 760$ nm, divided by the squared thickness for two different samples with and without the -7.5 kV mesh grid. Compared to the film deposited without the retarding grid the SHG signal was reduced by a factor ~ 47 . Thus, electrons and/or O^- ions play a significant role in the creation of the optical nonlinearity.

It is expected that room temperature deposited SiO films have a high density of defects. Furthermore, O^- ion may be accelerated towards the sample and create defects on collisions with atoms within the film [22]. Thus, as the film grows one must expect that a high density of vacancies is generated throughout the film. One could imagine that the generation of defects by ions impinging from a direction perpendicular to the surface could lead to a second-order nonlinearity. However, these defects are expected to have a considerably higher activation energy than the 0.36 eV (Fig. 5(a)) observed here. This energy is more consistent with desorption of foreign species attached to the defects. Such adsorbed species would form dipoles that could be oriented by charges on the film surface. SIMS measurements (not showed here) performed on a 200-nm thick SiO film showed the presence of hydrogen atoms in a concentration of 2 hydrogen atoms per 13 silicon atoms. Thus, these vacancies may be passivated by hydrogen.

The necessity for defect generation in order to obtain second-order nonlinearities in glasses has been demonstrated by Kameyama and Yokotani [23]. They showed that introduction of

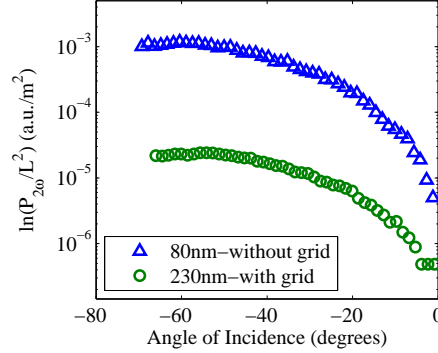


Fig. 6: The SHG signal from two different SiO films prepared with and without a retarding grid. Using a retarding grid reduces the SHG signal by a factor of ~ 47 in this case.

defects into highly pure silica glasses (using a KrF excimer laser) was necessary in order to create a nonlinear optical response in the subsequent thermal poling process. Moreover, the presence of hydrogen in the glass films was important for the magnitude of the nonlinearity.

The effect of foreign ions on defects in oxide films has been studied by Argalland and Jon-scher [24] through electrical measurements on thermally deposited silicon monoxide. They found a polarization of the films which they ascribed to hydrogen atoms bound to silicon. Moreover, they found activation energies around 0.5 eV for the induced polarization. The activation energy found in the present work (Fig. 5(a)) is thus comparable to those obtained from electrical measurements. In addition to Si-H bonds also Si-OH and Si-O bonds are expected in the films, but due to the relatively low observed activation energy (0.1-0.36 eV) it is expected that Si-H dipoles dominate the nonlinearity. However, since two activation energies are found more than one contribution may be present, e.g. desorption of hydrogen from Si-H and Si-OH species.

A second-order nonlinearity requires orientation of the bonds generated at defect sites. This orientation may be driven by a field generated in a way similar to that described for corona poling. In this process ions generated in the gas above the thin film are accelerated towards the film where they are deposited and create an internal field across the film that orients bonds to impurity atoms [25]. Following this analogy, the O^- ions in the e-beam deposition process renders the film surface negatively charged, resulting in process similar to that of a corona poling. Thus, the O^- ions both create defects and deliver the charges leading to orientation of the dipoles at defect sites.

In order to further investigate the origin of SHG a 160-nm thick SiO film was rf-magnetron sputtered onto a fused silica substrate. Here the rf-field traps the electrons and the argon ion plasma is close to the target. Thus no charging of the substrate takes place. The sample appeared almost transparent with an energy band gap of $E_{opt} \leq 4.2$ eV and no measurable nonlinear response. The same was the case for a 250-nm thick SiO₂ film e-beam deposited without the retarding grid. Moreover, it appeared as transparent as fused silica. Furthermore, while deposition of a new SiO₂ film with the retarding grid no blueish plasma was visible even with a fiber spectrometer. It is suggested that the lack of a nonlinear response from the e-beam deposited SiO₂ film is due to saturation of Si bonds with oxygen atoms in a dense structure that does not allow formation of oriented Si-H dipoles.

Ning et al. [6] found a strong second order nonlinear susceptibility of 2.5 pm/V in silicon nitride films grown at 300°C by PECVD onto fused silica. They suggested that very small

Si nanocrystals with Si-Si dimers showing an anharmonic response to the applied field are responsible for the strong SHG. If Si nanocrystals are formed in the SiO films in the present work the orientational mechanism leading to a macroscopic nonlinear coefficient could be the oxygen ions as described above. However, a signature of nanocrystal formation in glass is photoluminescence which was only observed after annealing of the room temperature grown films at temperatures where the SHG signal had disappeared. This does not support formation of nanocrystals as the origin of the SHG response in the SiO films.

The observations described above lead us to suggest that the nonlinearity of the SiO film is related to the formation of oriented dipoles. The dipoles are formed at defects created during film growth. The dipoles are oriented perpendicular to the film surface by the negative charging of the sample from the O^- ions during deposition, as sketched in Fig. (7). Thus, as the film grows the oxygen ions at the surface maintain the preferred orientation of the dipoles resulting in a non-centrosymmetric film, i.e. the orientation of the dipoles takes place continuously during the deposition due to the dc- field across the growing surface. This would be consistent with the quadratic dependence of SHG with film thickness.

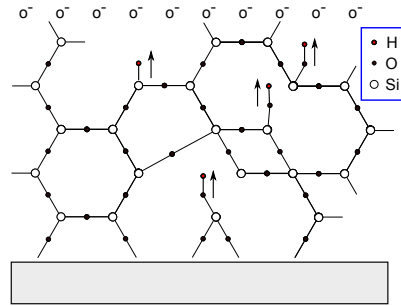


Fig. 7: A sketch illustrating oriented dipoles arising due to a charging of the film during deposition caused by oxygen ions. Drawing inspired from [24]. The sketch is based on a SiO_2 structure since it is difficult to represent an amorphous SiO structure.

The dc-field generated in the SiO film will also give rise to an effective second order non-linearity through the third order susceptibility as described for thermal poling [26] and electron beam irradiation of glass [8, 9, 10]. Assuming constant third-order susceptibility this contribution can give a quadratic dependence on film thickness only if the created dc-field is independent of thickness. The separated opposite charge distributions giving rise to this field are expected to be concentrated at the interfaces. To compensate for the growing separation between interfaces the charge densities should grow proportional to the film thickness. It is not clear how such interface charge layers can build up. It is thus suggested that the dipole orientation described above dominates the nonlinear response of the film.

5. 2D structures

One of the advantages of direct deposition of a nonlinear film could be the possibility of defining structures on substrates by lithography. In order to demonstrate this possibility a structure was defined by UV lithography in a $2\text{-}\mu\text{m}$ thick photoresist. After development a 200-nm thick SiO film was deposited and a lift-off process left $200\text{-}\mu\text{m}$ wide SiO structures on the fused silica substrate. Figure 8(a) shows a SHG scan with 130×100 points recorded with a focused beam from a mode-locked Ti:Sapphire laser delivering 100-fs p-polarized pulses at a wavelength of 786 nm. Again colored glass filters were used to separate the excitation line from the SHG signal. The SHG signal was measured with a photomultiplier coupled to a photon counter.

The SHG scan shows a structure corresponding to that defined with lithography. A number of defects appearing in the scan are most likely due to poor lift-off.

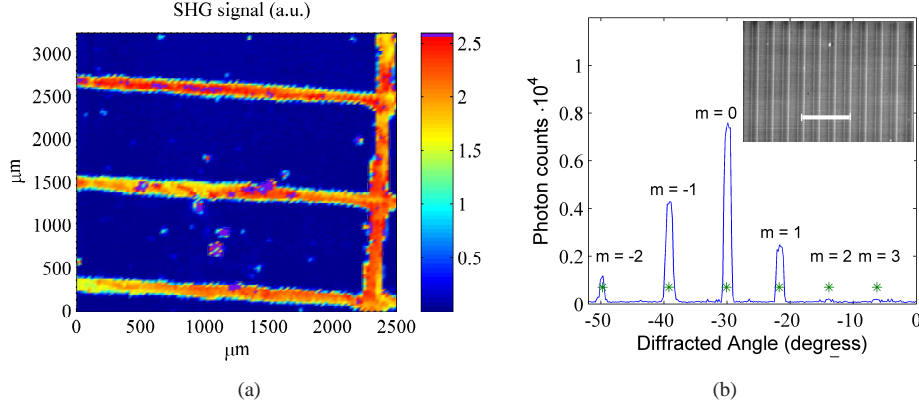


Fig. 8: SHG from SiO structures defined by lithography. a) SHG scan from a well-defined structure with 130x100 points recorded with a focused beam from a Ti:Sapphire laser operating at a wavelength of 786 nm. b) The SHG diffracted signal measured from a ~90-nm thick SiO grating consisting of ~1.4 μm wide lines that are spaced $d \sim 3\text{-}\mu\text{m}$ apart, see the inserted SEM image, scale bar is 10 μm wide.

Finally, we demonstrate by using e-beam lithography, that it is possible to define well-ordered nano-sized nonlinear structures. A 350-nm thick 3.5 % PMMA film was spin-coated onto a cleaned fused silica substrate and sputtering a thin aluminum layer on top made it possible to ground the sample and thus perform e-beam lithography. After the lithography process the aluminum was removed in a 30 % KOH solution and the structure was developed. Then a 90-nm thick SiO film was e-beam deposited on the sample and after the deposition the PMMA was removed with acetone, thus resulting in the structure shown in the SEM image in the insert in Fig.8(b). The lines are 1.4 μm wide and with a period $d \sim 3\text{ }\mu\text{m}$ resulting in a linear- and a nonlinear diffracting SiO grating.

Fig.8(b) shows the measured SHG diffracted signal from the SiO grating. Again we used the mode-locked Ti:Sapphire laser and a photomultiplier coupled to a photon counter. The SHG photons were measured during rotation of the photomultiplier behind the SiO diffracting grating. The green stars indicate the predicted maxima for the $m = -2, -1, 0, 1, 2$ and 3 order modes by using the grating equation

$$m \cdot \lambda_p/2 = d (\sin(\theta_i) + \sin(\theta_m)).$$

Here $\lambda_p/2$ is the wavelength of the SHG signal. In the experiment the incident angle is $\theta_i = 30^\circ$ and θ_m are the angles of the m 'th order of diffraction. It is clear that the nonlinear response of the SiO film is intact after formation of nanoscale structures.

6. Conclusion

It has been demonstrated that e-beam deposition of SiO is an simple way to synthesize nonlinear thin films with a built-in second order nonlinearity that is comparable in magnitude to that of crystalline quartz. The nonlinearity is stable at room temperature, but decays at elevated temperatures. Spectroscopic measurements show that the nonlinear response has a resonance

corresponding to the band gap at 3.3 eV found in linear absorption spectra. The resonance is however broad and leads to appreciable SHG for pump wavelengths from the near-infrared through the visible region. It is suggested that the nonlinearity is caused by $\text{Si}^{n+}-\text{H}^-$ dipole pairs oriented in the direction perpendicular to the surface by charging of the film during the e-beam deposition. Direct formation of nonlinear structures with in-plane dimensions of a few micrometers by a lift-off process has been demonstrated. It has thus been shown that nonlinear optical components with sizes in the region of interest for planar integrated optics technology may be fabricated by e-beam deposition of SiO_2 .

Acknowledgments

We thank John Lundsgaard Hansen, Department of Physics and Astronomy at Aarhus University (AU), for the assistance with the RBS and SIMS measurements. A thanks to Peter Kjær Kristensen at the Department of Physics and Nanotechnology in Aalborg for assistance with EBL. Finally, a special thanks to Arne Nylandsted Larsen (AU) for the fruitful discussions concerning the microscopic structure of the films.

B

**Appl. Phys. Lett. 103, 231906
(2013)**

Growth direction of oblique angle electron beam deposited silicon
monoxide thin films identified by optical second-harmonic generation

by

Søren Vejling Andersen, Mads Lund Trolle and Kjeld Pedersen



Growth direction of oblique angle electron beam deposited silicon monoxide thin films identified by optical second-harmonic generation

Søren Vejling Andersen,^{a)} Mads Lund Trolle, and Kjeld Pedersen

Department of Physics and Nanotechnology, Aalborg University, Skjernvej 4A, DK-9220 Aalborg Øst, Denmark

(Received 27 September 2013; accepted 14 November 2013; published online 3 December 2013)

Oblique angle deposited (OAD) silicon monoxide (SiO) thin films forming tilted columnar structures have been characterized by second-harmonic generation. It was found that OAD SiO leads to a rotationally anisotropic second-harmonic response, depending on the optical angle of incidence. A model for the observed dependence of the second-harmonic signal on optical angle of incidence allows extraction of the growth direction of OAD films. The optically determined growth directions show convincing agreement with cross-sectional scanning electron microscopy images. In addition to a powerful characterization tool, these results demonstrate the possibilities for designing nonlinear optical devices through SiO OAD. © 2013 AIP Publishing LLC. [<http://dx.doi.org/10.1063/1.4835075>]

Deposition of materials under oblique angles leads to porous films with excellent control of the porosity and thus also control over a number of physical properties of the film.^{1–5} Oblique angle deposition (OAD) usually leads to columnar structures tilted by an angle β relative to the surface normal depending on deposition angle α .^{4,6,7} By controlling the deposition angle, and thereby the micro-structure of the film, a continuous variation of the refractive index from almost unity to the bulk value of the dense material can be obtained.^{1,2} This technique has been applied for fabrication of graded index antireflection coatings designed for, e.g., solar cells^{1,2} or light-emitting diodes.⁸ OAD also offers flexible design of substrates for growth of semiconductors, e.g., GaN.⁹ Furthermore, porous silicon monoxide (SiO) structures obtained through OAD have been applied as humidity sensors.¹⁰

While the linear optical properties of OAD films have been studied extensively, only a few examples of nonlinear optical investigations of such films can be found in the literature, focusing on the use of optical second-harmonic generation (SHG) to characterize thin films of Al₂O₃,¹¹ AlN,¹² and ZnO.¹³ In the case of non-centrosymmetric materials with inherent second-order nonlinearities, such as ZnO, the orientation of the crystal structure relative to the surface defines the effective nonlinear optical tensor elements seen in an experiment. Typically, such materials will have a crystal symmetry direction along the columns of the OAD grown film.¹³ The present authors have recently shown that SiO films grown by electron beam (e-beam) deposition have a nonlinear response comparable to that of non-centrosymmetric crystals.¹⁴ It was suggested that the nonlinearity arises from Si–H bonds oriented by ions during the e-beam deposition process. For films grown at normal deposition direction, the field from ionized atoms orients Si–H bonds perpendicular to the surface resulting in rotationally isotropic SHG.¹⁴

In this Letter, it is shown that through oblique angle deposition the formation of a columnar structure can be used to

control the orientation of the Si–H bonds in the SiO films and that the orientation of the columns can be determined from SHG experiments. By analyzing a series of samples grown with varying deposition angle, a correlation between the angle of incidence (AOI) dependence of the SH signal and growth direction is found. This can be understood in terms of an extension of the model previously used to analyze Maker fringes,¹⁵ which then allows for extraction of the growth direction from SH angular measurements. To verify the optical model, we compare with a systematic study using cross-sectional scanning electron microscopy (SEM) imaging. An agreement to within the accuracy of the SEM measurements is generally found.

In a Cartesian coordinate system (x', y', z'), see Fig. 1(a), with the z' -axis aligned along the direction defining the broken centrosymmetry, where the angle ζ is the angle between z' -axis and the z -axis, only seven elements of the bulk SH susceptibility tensor are non-vanishing while three of these are independent;¹⁶ $\chi_{x'x'z'}^{(2)} = \chi_{y'y'z'}^{(2)} = \chi_{z'z'z'}^{(2)} = \chi_{x'z'x'}^{(2)} = \chi_{y'z'y'}^{(2)} = \chi_{z'x'x'}^{(2)} = \chi_{z'y'y'}^{(2)}$. This follows from the fact that dipolar selection rules cause only tensor elements with an odd number of z' -indices to contribute. On similar grounds, elements with three different indices also vanish. Furthermore, the x' and y' directions are fully equivalent, so x' may be substituted by y' freely. Finally, intrinsic permutation symmetry reduces the number of independent elements further, yielding the three independent elements mentioned above. Moreover, to simplify the fitting procedure in this work, Kleinman symmetry is assumed. This leaves only two non-vanishing elements of interest, namely, $\chi_{z'z'z'}^{(2)}$ and $\chi_{z'x'x'}^{(2)}$.

In the case of $\alpha = 0^\circ$, the primed and unprimed coordinate systems coincide, and an observable second-harmonic response arises exclusively from polarization in the xy plane, requiring the fundamental optical electric field to contain components parallel to the growth direction. This is readily seen by projection of the in-plane SH polarization components $\vec{P}_{xy}^{(2)}$

$$\vec{P}_{xy}^{(2)} = [(\chi_{xxz}^{(2)} + \chi_{xzx}^{(2)})E_x^{(1)}\hat{x} + (\chi_{yyz}^{(2)} + \chi_{yzy}^{(2)})E_y^{(1)}\hat{y}]E_z^{(1)}. \quad (1)$$

^{a)}Electronic mail: sva@nano.aau.dk

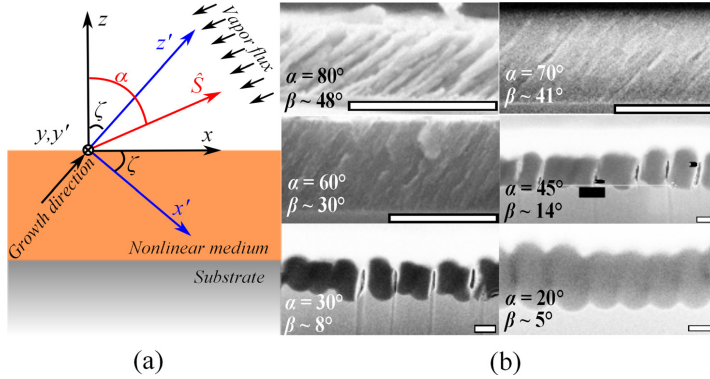


FIG. 1. (a) OAD growth of a thin film with the incident flux anti-parallel to \hat{S} at an angle α relative to the surface normal and the growth direction of columns along the z' axis making an angle β with the surface normal. The direction of broken symmetry, defined by ζ , coincidence with β in (a). Note, however, that this cannot be assumed a priori. For this reason, we distinguish between these angles. (b) Cross sectional SEM images showing structures of SiO films deposited at different α . Textured aluminum substrates were used in order to determine β for $\alpha \leq 45^\circ$. Here, Pt was deposited on top to gain a higher contrast. The remaining images show tilted SiO films deposited on silicon. The white scale bars are 300 nm.

Here, $\vec{E}^{(1)}$ is the fundamental field. Hence, a minimum in the transmitted SH signal is found for the optical AOI $\theta = 0^\circ$, while the group of four equivalent elements above contribute for $\theta \neq 0^\circ$, noting that $E_z^{(1)} \propto \sin(\theta)$. For $\alpha \neq 0^\circ$, these contributions vanish for fundamental fields inside the film perpendicular to the z' -direction, suggesting a minimum in SHG for the corresponding θ . However, an observable contribution from the $\chi_{z'x'x'}$ and $\chi_{z'y'y'}$ elements is found for $\theta \neq 0^\circ$, and the question remains how ζ can be extracted. In the following, we propose a model for this. The second-harmonic intensity $I_{2\omega}$ generated in a nonlinear optical film deposited on a substrate with purely linear optical response can in a transmission setup be related to the intensity of the fundamental beam I_ω by the expression¹⁵

$$I_{2\omega} = F_\omega(\theta) \left| \frac{\chi_{\text{eff}}^{(2)}}{2} \right|^2 I_\omega^2. \quad (2)$$

Here, F_ω contains a combination of Fresnel reflection and transmission coefficients. The SH response of the film is described by the effective nonlinear susceptibility $\chi_{\text{eff}}^{(2)}$ defined in terms of $\vec{\chi}^{(2)}$ through $\chi_{\text{eff}}^{(2)} = \hat{e}_2 \cdot \vec{\chi}^{(2)} : \hat{e}_1 \hat{e}_1$. Here, \hat{e}_m is the polarization vector of the $m\omega$ frequency component of the field inside the nonlinear medium, whereas $\{a, b, c\}$ indicate Cartesian indices. However, the use of Eq. (2) requires the Cartesian basis to be aligned with the plane of the film. Hence, we transform into lab coordinates (x, y, z) , with z normal to the interfaces by a rotation of the primed coordinate system by an angle ζ around the y and y' axes, which are taken parallel, denoting the corresponding transformation matrix by \mathbf{R} . Thus, the SH susceptibility tensor $\chi_{abc}^{(2)}$, $\{a, b, c\} \in \{x, y, z\}$ in the lab coordinate system follows from rotation of a third-rank tensor in the primed coordinate system

$$\chi_{abc}^{(2)} = \sum_{lmn} R_{al} R_{bm} R_{cn} \chi_{lmn}^{(2)}, \quad (3)$$

where the summations are taken over the Cartesian indices (and the primed indices are taken from $\{x', y', z'\}$). By measuring the transmitted SH intensity as a function of θ , the symmetry direction ζ can be extracted from the above model

by least-square fitting to experimental results. Similarly, the lab coordinate system may be rotated around the z -axis by an azimuthal angle η simulating rotational anisotropy scans.

SiO thin films were deposited with a Cryofox deposition system¹⁴ simultaneously on n-type Si(001) and fused silica (FS) substrates with deposition angles α between 0° and 80° (tolerance of 1°). Film thickness varied from 580 nm at $\alpha = 0^\circ$ to 130 nm at $\alpha = 80^\circ$. FS substrates were used for nonlinear optical measurements due to their negligible SH response, while Si substrates were used for SEM imaging. Additionally, textured aluminum substrates¹⁷ were used to estimate β for low α by SEM. Figure 1(b) shows cross sectional SEM images of the SiO films for different α . The images from $\alpha = 60^\circ$ to $\alpha = 80^\circ$ are from SiO deposited on Si substrates. It turned out to be very difficult to determine β for films deposited with $\alpha < 45^\circ$ on Si. However, deposition on textured aluminum substrates¹⁷ triggers growth of well-separated columns where the growth direction is easily detected ($\alpha = 20^\circ, 30^\circ$, and 45° in Fig. 1(b)). Tanto *et al.*⁶ found little difference between OAD growth directions of germanium on textured and flat substrates. It is thus assumed here that β determined from films on textured aluminum are the same for those on Si and glass substrates. The complex refractive index of SiO films were estimated by spectroscopic ellipsometry using the Jellison and Modine model.¹⁸ Measurements of the p-polarized SHG as a function of θ and azimuthal angle η were performed with 5 ns p-polarized pulses at a pump wavelength of 760 nm from a Nd:YAG pumped optical parametric oscillator setup, while the time-resolved measurements were performed using a mode-locked (80 MHz) Ti:sapphire laser delivering 100 fs p-polarized pulses at a wavelength of 786 nm. All second-harmonic measurements were performed in a transmission setup. For details on the optical setup, see our previous work.¹⁴

It was found by Rutherford backscattering spectrometry (RBS) that porous oblique angle deposition SiO films tended to oxidize partly to a SiO_x film in the ambient atmosphere. This is due to water vapor reacting with Si-H and -Si-Si-bonds.¹⁹ Removal of Si-H bonds causing SHG in SiO is clearly seen in the time-decay of the SH response of a film grown with $\alpha = 60^\circ$ subjected to ambient atmosphere, see

Fig. 2(a). It should be noted that dense films deposited at normal incidence have a stable SH response. A capping layer deposited with the technique described by Steele *et al.*⁵ reduced the oxidation rate considerably. The SH response from such a film, deposited with a continuous variation of α , is complicated to model optically. For this reason, the current investigation is performed with un-capped films. We note that extraction of the columnar angles relies only on the shape of the AOI dependence and not the overall intensity. As the samples with different α were deposited simultaneously, the time in ambient air before inspection by SHG differ among the samples. To minimize variations in signal levels, samples with large α that is most prone to oxidation were analyzed first. It should, however, be noted that un-capped films with large α showed clear SHG signals even after several months in ambient air.

The rotational anisotropy about the lab z -axis of the sample with $\alpha = 60^\circ$ recorded at $\theta = 0^\circ$ and $\theta = 33^\circ$ is shown in Figure 2(b). These measurements were performed after one year of storage under ambient conditions. Figure 2(b) demonstrates how, at normal incidence, a maximum in second-harmonic generation is observed when the pump field is polarized with a maximum projection onto the columnar axis, following a $\cos^2(\eta)$ -dependence, thereby indicating a C_{1v} symmetry. Changing the angle of incidence to $\theta = 33^\circ$ leads to an asymmetrical θ -dependence and a higher maximum intensity as the projection of the pump field inside the sample has a larger component along the columns. Rotating the sample by $\eta = 180^\circ$ leads to a maximum that is considerably smaller than for $\theta = 0^\circ$ (notice the $\times 5$ scaling factor for the left-hand side of the scan) since the pump field now is almost parallel to the columns. The solid lines are the best fits with Eq. (2) when considering Eq. (3) and an azimuthal rotation of η .

Figure 3(a) shows the second-harmonic generated signal as a function of θ for different α normalized to the maximum from fitted curves. The samples were oriented with the deposition flux direction in the optical plane of incidence, hence $\eta = 0$. The y -axis in Fig. 1(a) is perpendicular to the optical plane of incidence, and θ was scanned by rotation around this axis. Also, the SiO structures are tilted towards $\theta \geq 0^\circ$.

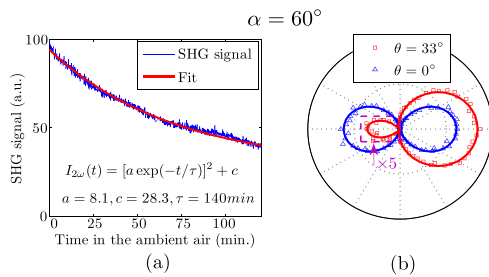


FIG. 2. SHG from sample $\alpha = 60^\circ$. (a) Oxidation effects on the nonlinear optical properties as a function of time. (b) The rotational anisotropy about the lab z -axis recorded at normal incidence ($\theta = 0^\circ$) and at $\theta = 33^\circ$. Solid lines are best fits with the model presented above. The data inside the purple box are multiplied by a factor of 5. The measurements in (b) were performed 1 yr later than the measurement in (a).

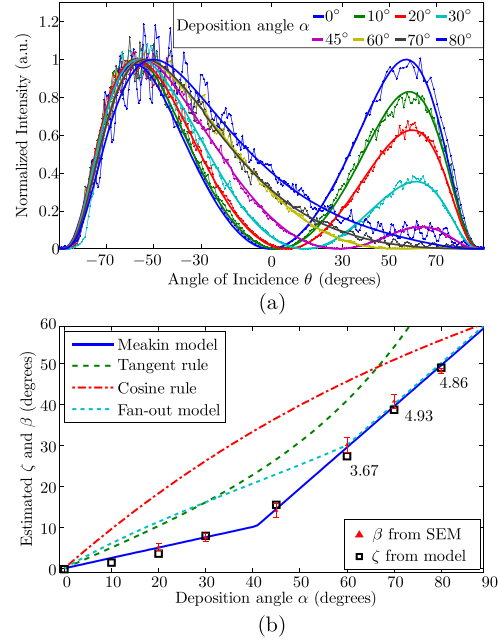


FIG. 3. (a) The SHG signal as a function of θ . The solid lines are the best fits using the presented model yielding ζ which is plotted in (b) together with Meakin's model (see Ref. 23), tangent rule (see Ref. 21), cosine rule (see Ref. 22), the fan-out model (see Ref. 6 ($\phi = 60^\circ$)), and the β values estimated by cross-sectional SEM imaging. The numbers are the estimated $\chi_{zzzz}/\chi_{zz'z'z'}$ from the fit in (a).

For $\alpha = 0^\circ$, the dependence is symmetrical with maxima near $\theta = \pm 60^\circ$ and minimum at $\theta = 0^\circ$. When α is increased, the minimum shifts to larger θ and the maximum at positive θ decreases. As a consequence, the film shows significant SHG at normal incidence for deposition angles larger than $\sim 30^\circ$. It should be noted that growth at different deposition angles leads to comparable signal levels at the maxima. Thus, $\chi_{\text{eff}}^{(2)}$ of an OAD grown film is comparable to that of a film grown at normal incidence, i.e., $\chi_{\text{eff}}^{(2)} \sim 0.16$ pm/V (Ref. 14). Films deposited under large α become transparent due to the oxidation, as already mentioned, hence, we attribute the rapid oscillations in Fig. 3(a) to multiple reflections. The solid lines in Fig. 3(a) are best fits using Eqs. (2) and (3). Since the linear optical properties change as the films oxidize, the exact linear properties of the individual films are not known. It is chosen here to use the optical properties of stable SiO films deposited at normal incidence for all films. Furthermore, it is assumed that the ratio between the χ_{zzzz} and $\chi_{zz'z'z'}$ elements is 3:1 which is in agreement with previously estimated ratios for $\alpha = 0^\circ$ films¹⁴ and as it is often found for poled glass materials.²⁰ However, for $\alpha \geq 60^\circ$, this ratio was also used as a fitting parameter, with initial value $\chi_{zzzz}/\chi_{zz'z'z'} = 3$, to achieve agreement between model and the AOI-dependence of SHG. The fitted ratios can be found in Fig. 3(b). We note that upon taking the ratio as a free parameter, the fit still converges to the correct ζ

compared to cross-sectional SEM images. The reason for variations in the ratio between the nonlinear polarizabilities parallel to and along the columns may be changes in the micro-structural properties of the film. Figure 3(b) also shows the values of ζ from the fitting procedure along with those determined from the SEM images. A convincing agreement between the two methods is seen. Hence, the symmetry direction defined by ζ is identical to the columnar growth direction defined by β . The fitting procedure for AOI SHG data was found to be very robust with respect to initial parameters, even for $\alpha > 60^\circ$ where there is no minimum in the θ -dependence.

The results for ζ and β are compared to the semi-empirical tangent²¹ and cosine²² models often used in the literature. The cosine-rule clearly has a form that does not agree with the data and while the tangent-rule has a better overall shape it overestimates the columnar angle relative to the deposition angle. A more recent model suggested by Tanto *et al.*⁶ called the fan-out model, assumes a linear relation between α and β for α larger than a certain transition angle (fan-angle). This seems to agree well with the SiO results for $\alpha > 60^\circ$ when a fan-angle of 60° is used. Fan-angles for a large number of materials have been investigated by Zhu *et al.*⁷ and found to cover a broad range from 10° to 80° . However, in the present case the model gives a poor representation of the data for $\alpha < 60^\circ$. A much better representation of the data is obtained by the model suggested by Meakin²³ on the basis of simulations of ballistic deposition. This model describes the relation between ζ and α by $\zeta = c_1\alpha$ for small angles and $\zeta = \alpha - c_2$ for larger angles. For the OAD SiO film, the data are well represented by $c_1 = 0.25$ for $\alpha < 40^\circ$ and $c_2 = 30.5^\circ$ for larger α .

The SHG experiments show that OAD leads to a nonlinear response tensor with a symmetry axis that is not perpendicular to the surface. From the SHG experiments, this direction is found to be along the only structural symmetry direction in the material, namely, along the columns. This requires formation of a local electric field during the e-beam deposition process that gives an average orientation of the Si-H bonds along the columns. The mechanism behind this is currently not understood.

In conclusion, the growth direction of the columnar structure characterizing oblique angle deposited SiO was identified by optical second-harmonic generation. A very good agreement with cross-sectional SEM images was

achieved, demonstrating SHG as a powerful and fast characterization tool of OAD SiO. As indicated by the previous experiments on AlN¹² and ZnO,¹³ this technique may be extended to other OAD deposited non-centrosymmetric materials. The dependency of the SH response on growth direction of SiO also enables tuning of the SH susceptibility tensor, essentially rotating it by the growth angle β . Hence, engineered nonlinear properties of SiO nanostructures, e.g., defined by lithography, may enable fabrication of nonlinear optical devices that are compatible with Si process technology.

The authors acknowledge the assistance of Peter Kjær Kristensen and Britta Johansen for SEM imaging and of John Lundgård Hansen for RBS. Furthermore, Yao-Chung Tsao supplied the textured aluminum substrates.

- ¹J. Q. Xi, M. F. Schubert, J. K. Kim, E. F. Schubert, M. Chen, S. Y. Lin, W. Liu, and J. A. Smart, *Nature Photon.* **1**, 176 (2007).
- ²S. Chhajed, M. F. Schubert, J. K. Kim, and E. F. Schubert, *Appl. Phys. Lett.* **93**, 251108 (2008).
- ³M. M. Hawkeye and M. J. Brett, *J. Vac. Sci. Technol. A* **25**, 1317 (2007).
- ⁴K. Robbie and M. J. Brett, *J. Vac. Sci. Technol. A* **15**, 1460 (1997).
- ⁵J. J. Steele and M. J. Brett, *J. Mater. Sci. Mater. Electron.* **18**, 367 (2007).
- ⁶B. Tanto, G. T. Eyck, and T. M. Lu, *J. Appl. Phys.* **108**, 026107 (2010).
- ⁷H. Zhu, W. Cao, G. K. Larsen, R. Toole, and Y. Zhao, *J. Vac. Sci. Technol. B* **30**, 030606 (2012).
- ⁸J. K. Kim, S. Chhajed, M. F. Schubert, E. F. Schubert, A. J. Fischer, M. H. Crawford, J. Cho, H. Kim, and C. Sone, *Adv. Mater.* **20**, 801 (2008).
- ⁹L. C. Chen, C. H. Tien, W. C. Liao, and Y. M. Luo, *J. Lumin.* **131**, 1234 (2011).
- ¹⁰K. Harris, A. Huizinga, and M. Brett, *Electrochem. Solid-State Lett.* **5**, H27 (2002).
- ¹¹V. Mizrahi, F. Suits, J. E. Sipe, U. J. Gibson, and G. I. Stegeman, *Appl. Phys. Lett.* **51**, 427 (1987).
- ¹²D. Blanc, A. Cachard, and J. C. Pommier, *Opt. Eng.* **36**, 1191 (1997).
- ¹³K. Lo, S. Lo, S. Chu, R. Chang, and C. Yu, *J. Cryst. Growth* **290**, 532 (2006).
- ¹⁴S. V. Andersen and K. Pedersen, *Opt. Express* **20**, 13857 (2012).
- ¹⁵W. N. Herman and L. M. Hayden, *J. Opt. Soc. Am. B* **12**, 416 (1995).
- ¹⁶R. W. Boyd, *Nonlinear Optics* (Academic Press, San Diego, 2003).
- ¹⁷Y.-C. Tsao, T. Søndergaard, E. Skovsen, L. Gurevich, K. Pedersen, and T. G. Pedersen, *Opt. Express* **21**, A84 (2013).
- ¹⁸J. G. E. Jellison and F. A. Modine, *Appl. Phys. Lett.* **69**, 371–373 (1996).
- ¹⁹W.-S. Liao and S.-C. Lee, *J. Appl. Phys.* **80**, 1171 (1996).
- ²⁰R. A. Myers, N. Mukherjee, and S. R. J. Brueck, *Opt. Lett.* **16**, 1732 (1991).
- ²¹J. M. Nieuwenhuizen and H. B. Haanstra, *Philips Tech. Rev.* **27**, 87 (1966).
- ²²R. Tait, T. Smy, and M. Brett, *Thin Solid Films* **226**, 196 (1993).
- ²³P. Meakin, *Phys. Rev. A* **38**, 994 (1988).

C

**Appl. Phys. Lett. 104, 051602
(2014)**

Interaction between O₂ and ZnO probed by time-dependent
second-harmonic generation

by

Søren Vejling Andersen, Vincent Vandalon, Roger Bosch, Bas van de
Loo, Kjeld Pedersen, and Erwin Kessels



Interaction between O₂ and ZnO films probed by time-dependent second-harmonic generation

S. V. Andersen,^{1,2,a)} V. Vandalon,¹ R. H. E. C. Bosch,¹ B. W. H. van de Loo,¹ K. Pedersen,² and W. M. M. Kessels^{1,b)}

¹Department of Applied Physics, Eindhoven University of Technology, P.O. Box 513, 5600 MB Eindhoven, The Netherlands

²Department of Physics and Nanotechnology, Aalborg University, Skjernvej 4A, DK-9220 Aalborg Øst, Denmark

(Received 18 December 2013; accepted 18 January 2014; published online 3 February 2014)

The interaction between O₂ and ZnO thin films prepared by atomic layer deposition has been investigated by time-dependent second-harmonic generation, by probing the electric field induced by adsorbed oxygen molecules on the surface. The second-harmonic generated signal decays upon laser exposure due to two-photon assisted desorption of O₂. Blocking and unblocking the laser beam for different time intervals reveals the adsorption rate of O₂ onto ZnO. The results demonstrate that electric field induced second-harmonic generation provides a versatile non-contact probe of the adsorption kinetics of molecules on ZnO thin films. © 2014 AIP Publishing LLC. [<http://dx.doi.org/10.1063/1.4863942>]

Oxygen interaction with ZnO thin films and nanowires has been intensively studied due to the interesting applications of ZnO such as in O₂ sensors^{1,2} and UV detectors.^{3,4} O₂ can adsorb at surface defect sites by capturing a free electron from the *n*-type ZnO thin film,⁵ resulting in O₂⁻ formation at the surface. The associated electric field leads to upward bending of the energy bands of ZnO and a depletion region is created.^{1–8} Therefore, the free electrons are repelled from the surface, and a corresponding increase of surface resistivity can be observed.^{1,3,9} Exposing the film to UV photons with an energy larger than the band gap of 3.4 eV generates electron–hole pairs. The holes will migrate along the potential slope created by the band bending and recombine with the oxygen ions located at the surface. This process causes photo desorption of O₂ and a decrease in resistivity is observed, hence making it possible to use the system as an UV detector and O₂ sensor.

Optical second-harmonic generation (SHG) is a well-established tool for investigations of adsorption of species on surfaces.¹⁰ The technique has been used for studies of adsorption and desorption of species at defect sites on rutile TiO₂ surfaces. Shultz *et al.*¹¹ have investigated UV defect generation and subsequent time dependent healing of the defects by O₂ exposure. Also, the interaction of TiO₂ with water has been probed by SHG.¹² In these investigations, the sensitivity of SHG to adsorbed molecules has been ascribed to a general sensitivity to defects through their modifications of the surface band structure. However, a number of investigations have demonstrated a strong sensitivity of SHG to charges at semiconductor surfaces and interfaces through an electric field induced third-order effect. Important information about the space-charge regions at interfaces between silicon and thin films has been revealed.^{13–15} Intensive research has been carried out on the dynamics of electric field induced

SHG (EFISH) from adsorption of O₂ ions on native oxide covered silicon surfaces.^{16,17}

In this Letter, we demonstrate that the dynamics of adsorption and desorption of O₂ on ZnO thin films can be probed by time-dependent second-harmonic generation (TD-SHG). The oxygen-induced field at the surface of the ZnO leads to an EFISH contribution. At the same time, the probing laser beam can lead to desorption of adsorbed oxygen and hence cause a decrease in the SHG response. By blocking and unblocking the laser beam, the decay and recovery of the signal due to desorption and adsorption of oxygen can be studied. It was found that the adsorption rates estimated by TD-SHG are comparable to those determined by resistivity measurements.

Thin (20 nm) polycrystalline ZnO films were deposited by atomic layer deposition (ALD) at 200 °C (labeled T200) and at 180 °C (labeled T180) in an Oxford Instruments OpAL reactor, using H₂O as the oxidant and (C₂H₅)₂Zn as the metal precursor. The thin films were deposited on *n*-type Si(100) wafers with native oxide. Additionally, a sample prepared at 200 °C was capped directly after the deposition with a 5 nm thick Al₂O₃ by ALD, from trimethylaluminum (TMA, Al₂(CH₃)₃) and H₂O. Furthermore, a 86 nm thick ZnO film was deposited on Corning 7059 glass. More details on the preparation and properties of the ZnO films can be found elsewhere.⁶ The linear optical properties and thickness of the different thin films were determined with spectroscopy ellipsometry (SE) measurements (J. A. Woollam, Inc., M2000U (0.75–5.0 eV)).

The TD-SHG experiments were performed in reflection mode using a mode-locked Ti:Sapphire laser (Tsunami, Spectra-Physics) delivering 90 fs p-polarized pulses (80 MHz repetition rate) with a photon energy of 1.675 eV focused onto the sample with a doublet lens (focal length 200 mm) resulting in an average laser intensity varying from 10 to 50 MW/cm². Colored glass filters (Schott BG40) were used to separate the excitation radiation from the second-harmonic (SH) radiation. The SHG signal was

^{a)}Electronic mail: sva@nano.aau.dk

^{b)}Electronic mail: w.m.m.kessels@tue.nl

detected with a photomultiplier tube coupled to single photon counting electronics. The angle of incidence of the laser beam was 30° except for the measurements in which the surrounding ambient of the sample was changed by using a closed chamber. In these experiments, the sample was placed at 45° angle of incidence. The chamber could be purged with dry nitrogen, and air could be reintroduced through a valve. All the measurements were performed at room temperature and a relative humidity of 40%. Moreover, T200 was exposed to 3 mW/cm^2 radiation at 237 nm from a Cole-Parmer Pen-Ray UV lamp (YO-97606-00).

It is noted that both single crystalline¹⁸ and polycrystalline¹⁹ ZnO show a bulk second-harmonic response, due to its hexagonal closed packed structure. The 6mm symmetry allows three second-order tensor elements to contribute to a bulk SHG signal.

Figure 1 shows a typical TD-SHG signal (blue dots) from T200. The rapid decrease of signal upon laser exposure can be attributed to photon-assisted O_2 desorption. After the measured SH decay, the entire sample was exposed to UV irradiation for 15 min, thereby removing O_2 located at the surface of the sample. Recording of SHG was started again 1 min after the UV illumination (green squares) at a different spot to rule out the influence of the probing laser. Only a very small decrease in the SH signal is seen compared to the first measured decay. The small decay is most likely related to O_2 adsorbed at the ZnO surface during the 1 min time interval between UV exposure and the SHG experiment. An overall increase in signal after the UV illumination is noted (Fig. 1). Under UV illumination in an atmosphere containing water, Feng *et al.*²⁰ showed that it is energetically more favorable to adsorb hydroxyl groups (OH^-) on the ZnO surface defect sites instead of oxygen. Additionally, Li *et al.*²¹ and Ahn *et al.*²² found a slow increase in resistivity upon UV illumination due to OH^- adsorption on defect sites. Thus, OH^- located at the surface cause an upward bending of the energy bands leading to a larger SHG response, as can be seen in Fig. 1.

The red curve is the TD-SHG signal from the Al_2O_3 capped ZnO film. Since the reflectivity of Al_2O_3 is different

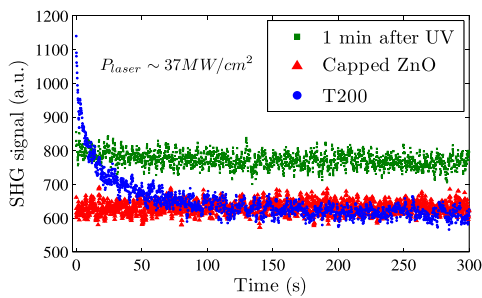


FIG. 1. TD-SHG signal from T200 (blue dots) in ambient air. The SHG signal from the Al_2O_3 capped film (red triangle) is stable in time since ZnO is not in contact with O_2 . UV illumination of ZnO removes O_2 from the surface, and the TD-SHG signal (green squares) recorded shortly after shows only a small intensity change. The overall increase in SHG after UV illumination may be related to OH^- formation at the surface.

from that of ZnO, the SH signal amplitude is multiplied by a factor of 1.37 to correct for this linear optical effect (the value is derived from SE results). Note that the TD-SHG signal is constant in time since ZnO no longer is in contact with O_2 , while the corrected signal amplitude is approximately the same as for T200. Furthermore, decay curves have also been measured for the 86 nm thick ZnO film prepared on a glass substrate. These observations demonstrate that the TD-SHG signals are related to the interaction between O_2 and the surface of the ZnO thin films, rather than to the silicon substrate.

Fig. 2(a) shows a typical TD-SHG signal from T180 along with a fit based on an exponential decay of the SHG signal of the form

$$I_{2\omega}(t) = [a_{\text{bulk}} + b_{\text{O}_2}e^{(-t/\tau_{de})}]^2. \quad (1)$$

This equation represents a coherent addition of the nonlinear optical response of a film without adsorbed oxygen a_{bulk} and an oxygen-induced response of amplitude b_{O_2} , decaying with a desorption time constant τ_{de} under laser illumination. As mentioned above, a polycrystalline ZnO film has a bulk SHG response.^{18,19} Further evidence for the bulk character of the a_{bulk} term comes from its magnitude which is several orders of magnitude larger than the response from the Si substrate. The SHG signal from the oxygen-induced E-field (E_{dc}), b_{O_2} , is related to the effective bulk third-order response tensor $\chi^{(3)}$ through $E_{2\omega} = \chi^{(3)}E_{\omega}E_{\omega}E_{dc}$,²³ where E_{dc} is related to the band bending in the depletion region generated by the adsorbed oxygen ions.

Figure 2(b) illustrates, on a double logarithmic scale, the behavior of the time constant (τ_{de}) as a function of the average laser power. The time constant decreases with average laser power and can be described by $1/\tau_{de} \propto P^{1.5 \pm 0.1}$, indicating that a multi-photon process plays a role in the desorption rather than thermal desorption. Additional evidence stems from SHG experiments carried out with an excitation

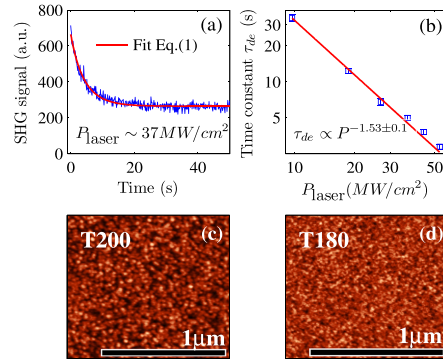


FIG. 2. (a) TD-SHG signal from T180 fitted with Eq. (1) yielding the time constant τ_{de} . In (b), τ_{de} is plotted as a function of average laser power indicating that a two-photon desorption process takes place. Note the double logarithmic scale. AFM images illustrating the surface morphology of T200 in (c) and of T180 in (d). Larger grains can be observed in (c) compared to (d).

photon energy of 1.55 eV, where no detectable decay of the SHG signal was observed. With 1.55 eV photons, the two-photon energy is too low to excite electrons across the band gap of ZnO, hence, no photo desorption can occur. This indicates that a two-photon process is responsible for O₂ desorption with 1.675 eV excitation energy. Thus, the laser beam generating the SHG probe signal is also responsible for the decay of the EFISH signal.

Investigations of the adsorption dynamics of O₂ are done by blocking the laser for different time intervals, so-called dark times t_d , followed by unblocking the beam to monitor the light-induced decay of SHG. Figure 3(a) shows a measurement on a fixed spot on T180 in ambient air, where the dark times are varied from 1 to 16 min. The level of the recovered signal ($\Delta I_{2\omega}$) increases with the dark time. When the same experiments are performed in N₂ environment, the signal amplitude never recovers, see Fig. 3(b). Additionally, when the sample was re-exposed to ambient air, the decay curve reappeared, see Fig. 3(c).

Recovery of the SHG signal from O₂ adsorption can be represented by $\Delta I_{2\omega}$, the change in SHG signal normalized to $\Delta I_{2\omega}^0$, the change in SHG signal from the first measured decay curve, see Fig. 3. The results are plotted in Fig. 4 as a function of dark time. The red squares in Fig. 4 are the data points extracted from Fig. 3(a) and the blue triangles are from Fig. 3(c).

Lampe and Müller¹ showed in their analysis of adsorption-induced changes in resistivity that the adsorption of oxygen ions on ZnO follows a logarithmic increase with O₂ exposure time. In addition, Barry and Stone² corroborated this behavior through pressure dependent measurements. In order to relate this to the TD-SHG results, it is noted that the total charge Q from adsorbed O₂⁻ is balanced by the charge

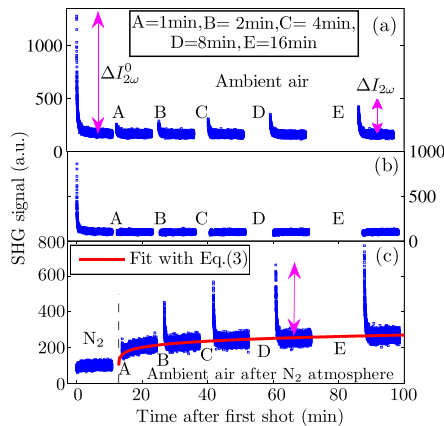


FIG. 3. TD-SHG signals from T180 measured in (a) ambient air, (b) N₂ atmosphere, where the first curve was measured 1 min after the N₂ purge was turned on. (c) After T180 was reintroduced to the ambient air. When unblocking the laser, the signal decays due to desorption of O₂ from the ZnO surface. After blocking the laser for different time intervals (dark times = A, B, ..., E), the signal strength only recovers when the sample is in the ambient air where O₂ is available. An overall increase in SHG signal in (c) is due to formation of OH⁻ during the laser illumination.

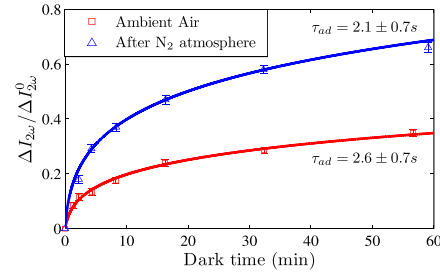


FIG. 4. The measured change in SHG signal, due to laser radiation exposure, normalized to the change of the first measured decay in SHG signal as a function of the dark time. The data reveal the adsorption rate τ_{ad} of O₂ on ZnO when fitted with Eq. (2). The data points are extracted from Fig. 3(a) (red squares) and Fig. 3(c) (blue triangles).

in the depletion region. This can be approximated by $Q = wN_d$, where N_d is the doping density and w is the width of the depletion region. In a first approximation, the oxygen-induced E-field, E_{dc} , will be proportional to w . Therefore, the recovery of the SHG signal as a function of dark time $\Delta I_{2\omega}(t_d)$, which is proportional to $(E_{dc})^2$, can be represented by the square of the logarithmic change in adsorbed O₂⁻ as presented by Barry and Stone² in the form

$$\Delta I_{2\omega}(t_d)/\Delta I_{2\omega}^0 \propto A \left[\ln \left(t_d + \frac{1}{\tau_{ad}} \right) + \ln(\tau_{ad}) \right]^2. \quad (2)$$

Here, A is related to the density of available surface defect sites and τ_{ad} is a characteristic time constant for adsorption on these sites. Using this relationship, the data in Fig. 4 can be fitted and provide the rate of adsorption τ_{ad} of O₂. For experiments in ambient air before and after the N₂ purge measurements, the adsorption rates were estimated to be $\tau_{ad} = 2.6 \pm 0.7$ s and $\tau_{ad} = 2.1 \pm 0.7$ s, respectively. The estimated TD-SHG adsorption rates compare fairly well to adsorption rates determined with resistivity measurement on a ZnO film, $\tau_{ad} = 1$ s at 280 °C (see Ref. 1) and nanowires at room temperature $\tau_{ad} = 4.6$ s (see Ref. 22) and $\tau_{ad} = 1.3$ s (see Ref. 3). Additionally, Barry and Stone² measured the adsorption rate to $\tau_{ad} = 3.5$ s from a ZnO powder sample at room temperature.

The faster O₂ response time τ_{ad} of T180 after the N₂ experiment could be related to the fact that N₂ purging also removes physisorbed H₂O from the surface, leaving behind more defect sites that can adsorb O₂. Hence, the factor A in Eq. (2) has changed. Moreover, Li *et al.*²¹ found a significant dependence of τ_{ad} on the amount of H₂O present in the atmosphere which is still not fully understood. Interestingly, an overall increase in base amplitude is noted when T180 is re-exposed to ambient air, see Fig. 3(c). This amplitude increase can be fitted with Eq. (2) indicating an adsorption process. Hence, it may be related to OH⁻ forming on defect sites due to the probing laser. Alternatively, this overall increase could be independent on the probing laser since water vapor in the ambient air has previously been shown to affect the dynamics of the ZnO-O₂ system.^{9,21,22} Isolated physisorbed water molecules remain undissociated on the

surface and do not capture electrons or holes. However, molecules adsorbed at neighboring surface sites may dissociate and enable oxygen atoms to capture electrons from the ZnO surface^{21,24} leading to an increased EFISH for high density of H₂O molecules on the ZnO surface.

Finally, we would like to address the difference in the SHG signal amplitudes between the measurement in Fig. 1 ($\Delta I_{2\omega} = 1.6$, T200) and Fig. 2 ($\Delta I_{2\omega} = 2.7$, T180). T180 was prepared at a slightly lower substrate temperature (180 °C) resulting in smaller grain sizes, as seen in the two AFM images in Figs. 2(c) and 2(d). Hence, more defect sites are expected to be present for T180 leading to a stronger oxygen induced electric field from more adsorbed O₂⁻ ions. This indicates that the amplitude change of the TD-SHG signal can be related to the surface morphology of the ZnO thin films.

In conclusion, time-dependent second-harmonic generation curves recorded from ZnO thin films deposited by ALD can be correlated to desorption/adsorption of O₂ on surface defect sites. A two-photon absorption process was found to be responsible for the laser-induced photo desorption of O₂. Adsorption rates for O₂ estimated by TD-SHG were found to be comparable to rates determined through resistivity measurements. TD-SHG can thus be used to investigate the interaction between O₂ and ZnO surface defect sites, and the technique may be extended to study adsorption kinetics of other species on ZnO thin films.

S.V.A. thanks the group PMP for the fruitful time at the Department of Applied Physics of the Eindhoven University of Technology. The authors thank Harm Knoops (TU/e) for the fruitful discussions on ZnO, Yizhi Wu (TU/e) for his deposition assistance, and Bart Macco (TU/e) for the AFM images. This work was supported by the Technology

Foundation STW through the VICI program on “Nanomanufacturing.”

- ¹U. Lampe and J. Müller, *Sens. Actuators* **18**, 269 (1989).
- ²T. I. Barry and F. S. Stone, *Proc. R. Soc. London, Ser. A* **255**, 124 (1960).
- ³Q. H. Li, T. Gao, Y. G. Wang, and T. H. Wang, *Appl. Phys. Lett.* **86**, 123117 (2005).
- ⁴C. Soci, A. Zhang, B. Xiang, S. A. Dayeh, D. P. R. Aplin, J. Park, X. Y. Bao, Y. H. Lo, and D. Wang, *Nano Lett.* **7**, 1003 (2007).
- ⁵S. B. Zhang, S. H. Wei, and A. Zunger, *Phys. Rev. B* **63**, 075205 (2001).
- ⁶Y. Wu, P. M. Hermkens, B. W. H. van de Loo, H. C. M. Knoops, S. E. Potts, M. A. Verheijen, F. Roozeboom, and W. M. M. Kessels, *J. Appl. Phys.* **114**, 024308 (2013).
- ⁷W. Göpel, G. Rucker, and R. Feierabend, *Phys. Rev. B* **28**, 3427 (1983).
- ⁸A. Oprea, N. Bärsan, and U. Weimar, *Sens. Actuators, B* **142**, 470 (2009).
- ⁹R. J. Collins and D. G. Thomas, *Phys. Rev.* **112**, 388 (1958).
- ¹⁰R. Corn and D. Higgins, *Chem. Rev.* **94**, 107 (1994).
- ¹¹A. N. Shultz, W. Jang, W. Hetherington III, D. Baer, L.-Q. Wang, and M. Engelhard, *Surf. Sci.* **339**, 114 (1995).
- ¹²E. Kobayashi, K. Matsuda, G. Mizutani, and S. Ushioda, *Surf. Sci.* **427–428**, 294 (1999).
- ¹³J. J. H. Gielis, B. Hoex, M. C. M. van de Sanden, and W. M. M. Kessels, *J. Appl. Phys.* **104**, 073701 (2008).
- ¹⁴G. Dingemans, N. M. Terlinden, D. Pierreux, H. B. Profijt, M. C. M. Van De Sanden, and W. M. M. Kessels, *Electrochem. Solid-State Lett.* **14**, H1 (2011).
- ¹⁵G. Lüpke, *Surf. Sci. Rep.* **35**, 75 (1999).
- ¹⁶Y. Q. An, J. Price, M. Lei, and M. C. Downer, *Appl. Phys. Lett.* **102**, 051602 (2013).
- ¹⁷J. G. Mihaychuk, N. Shamir, and H. M. Van Driel, *Phys. Rev. B* **59**, 2164 (1999).
- ¹⁸D. C. Haueisen and H. Mahr, *Phys. Rev. B* **8**, 734 (1973).
- ¹⁹H. Cao, J. Y. Wu, H. C. Ong, J. Y. Dai, and R. P. H. Chang, *Appl. Phys. Lett.* **73**, 572 (1998).
- ²⁰X. Feng, L. Feng, M. Jin, J. Zhai, L. Jiang, and D. Zhu, *J. Am. Chem. Soc.* **126**, 62 (2004).
- ²¹Y. Li, F. D. Valle, M. Simonnet, I. Yamada, and J. J. Delaunay, *Appl. Phys. Lett.* **94**, 023110 (2009).
- ²²S. E. Ahn, J. L. Soo, H. Kim, S. Kim, B. H. Kang, K. H. Kim, and G. T. Kim, *Appl. Phys. Lett.* **84**, 5022 (2004).
- ²³Y. R. Shen, *The Principles of Nonlinear Optics* (Wiley, New Jersey, 2002).
- ²⁴O. Dulub, B. Meyer, and U. Diebold, *Phys. Rev. Lett.* **95**, 136101 (2005).